Cranfield UNIVERSITY

Xavier Loyseau

Numerical simulation of droplet dispersion and deposition in pipes

This thesis is submitted in partial fulfilment of
the requirements for the Degree of Doctor of Philosophy

Under the supervision of:
Dr. Patrick Verdin

School of Water, Energy & Environment
Oil and Gas Engineering Centre
Cranfield University
United Kingdom
Academic year 2015-2016

Contents

List of Figures

List of Tables

Abstract

Multiphase flows are commonly encountered in industrial processes but remain challenging to predict. The role of droplets in the setting of various flow patterns seen in pipes is capital. Being able to simulate accurately the motion, the dispersion, the deposition and the entrainment of droplets from a liquid film or pool would allow refining the various numerical models and would provide a useful insight to people involved with such flows. The PhD work summarised in this thesis aims at answering that ambitious goal, i.e. to reproduce the whole "life" of a cloud of droplets, with application to pipes and industrial systems. To the author's knowledge, such study has never been realized with any open source computational fluid dynamics code such as OpenFOAM and in such details. An original surface-tracking motion has also been developed to solve wavy-stratified flows and droplets entrainment by extending OpenFOAM's capabilities. The Lagrangian framework has been selected for this study as the relationship with various forces could be expressed directly and statistical information, including any Eulerian field if needed, could be retrieved.

Acknowledgements

I would like to give special thanks to the people who helped me during this PhD, could it be to gather pertinent information or simply for their moral support. I would start to acknowledge Professor Chris Thompson for having granted me this opportunity and his guidance. I would then thank Doctor Patrick Verdin, who, as my supervisor, took the time to read and re-read my thesis and the various reviews I had to do during my PhD. I also thank him for his profound human support. He is someone who definitively deserves my respect. I respectfully thank Doctor Lloyd Brown for providing the industrial background of this thesis and for the fruitful discussions that helped me to better understand the multiphase flows in their real context. I would also like to my colleagues, doing a PhD just like me, beside me and for all the fruitful help they provided me with. Therefore, I thank Arnaud Bourdillon, who contributed with me to the same industrial project, and who I will remember always as a hard worker and perfectionist. I would like to thank Doctor Mustapha Gourma, who has a great detailed knowledge of all CFD techniques and who never looses his practical sense. I thank also Marcin Traczyk, skilled in statistical physics, with whom I had enlightened discussions. I would like to give special thanks for Doctor Robert Sawko, really skilled and always curious of absolutely every thing, always wanting to share his optimism and cheerfulness. I thank him for the support he provided all of us with the OpenFOAM software and the time he took to teach various topics ranging from CFD to general knowledge.

To all these people who helped me directly or indirectly and whose named I can't recall, I would like to give my sincere gratitude.

Chapter 1

Introduction

In oil and gas applications, it is often of significant importance to evaluate the behaviour of multiphase flows to design suitable equipments for extraction and safe transportation of fossil fuels. Nowadays, the use of computers to simulate such complex flows is mature enough to successfully help the industry on a daily basis. However, the precision and the complexity requested have never decreased and new models are always required to achieve more accurate results or to simulate more complex flow configurations.

Most of the flows involved in industrial processes are multiphase flows. Multiphase flows generally involve the generation and/or transport of droplets/particles. These droplets/particles are often responsible of major changes in the flow characteristics (flow pattern, mean density per phase, enhanced transport...) which are important to make industrial operations reliable. From the multiphase behaviour of the flows it is possible to evaluate the droplet transport, dispersion, collisions, deposition and the mass entrainment from one phase to another. The relation between droplet dispersion and deposition is not clearly known, especially in large or complex geometries.

Consequently, this research work aims at developing a new code able to reproduce the full "life" of droplets in industrial applications: from their injection, their motion, their deposition, up to the formation of a new continuous phase. To that end, it is important to study and understand the factors influencing the droplet motion (droplet properties, flow properties, interactions). This is the objective of the literature review, in the second chapter of this thesis. Multiphase flows will be introduced first, exposing the general behaviour of various flow patterns. Basics related to particulate flows is then explained. In particular, ways of representing poly-dispersed particles are discussed.

Next, common formulations to resolve particulate flows are briefly reviewed, especially the Euler-Euler and Euler-Lagrange methods. A section about the phenomena involved in particulate flows details the various forces and interactions that can be of importance when simulating this kind of flows. This section includes a description of the mathematical models used to solve the turbulent dispersion, the Brownian diffusion, as well as the method chosen to evaluate particle-particle collisions. Other phenomena such as the droplet break-up and the deposition are also explained.

After presenting the physical behaviour of particles motion, two sections present the computational details required to simulate multi-phase flows. These sections make aware the reader of the whole complexity of the task carried out during this thesis. They also explain why the Lagrangian approach was selected for in this research work.

The choice of the Lagrangian approach is not straightforward. Indeed Eulerian or PDF methods are perfectly valid ways of investigating the matter and the comparison with all these methods can be a thesis subject of its own. However, the Lagrangian approach is the one that is more directly related to the actual forces acting in real life. There are in theory no limitations to this approach, in contrary to other approaches which require further hypothesis to be put into action. It must be noted that other methods can sometimes be more informative, easier to interpret or more convenient to use in industrial applications. However, ways to post-process Lagrangian data to retrieve such useful information, and interpretations are detailed in this document.

Once the pre-requirements are exposed, the current limitations to be overcome become obvious, as well as potential ways of solving them. For instance, little information is available about the scaling-up of known and validated data in small pipes, to data in large industrial pipes. The reliability of the usual dimensionless data provided in the literature is also questionable. To palliate those problems, numerous simulations have been performed during this PhD, each looking at specific aspects of the numerics affecting directly the particulate flow prediction. Thus, Chapter 3 goes through the major results, obtained from the simulations performed during this PhD.

The statistics of the dispersion of a cloud of droplets is discussed in this chapter, introducing a new and published model of dispersion. Transient deposition of small droplets in a small vertical pipe is studied, in addition to a moving cloud of droplets. The former leads to the study of the time averaged deposition, expressing ways to post process large quantities of Lagrangian data.

These simulations are then extended and applied to pipes of large diameter, allowing a thorough investigation of the carrier flow and particle behaviours when scaling-up a rather simple geometry.

To demonstrate the operability of the code developed in an industrial context, the droplet deposition obtained in a perforated plate and on a valve geometry are discussed.

Chapter 4 is here to fulfil the scope of this PhD using the code developed during the past few years. Once deposited, droplets can coalesce and form a separated phase. To simulate this, a topological mesh solver has been implemented to represent the carrier phase in its own region. The details of the implementation are presented in this chapter. A proof of concept on the particle entrainment from the tracked interface is also discussed.

Finally, a general conclusion constitute the last chapter of this thesis. Droplet and flow results are summarized and potential future work is highlighted.

Chapter 2

Literature review

2.1 Description of multiphase flows

2.1.1 General description

Various visual aspects of the flow have been observed in multi-phase flows in pipes and they have been classified in what is generally called a "flow regime map". There are several factors that influence the aspect of a pipe flow, and among them, the surface volumetric velocity of each phase also called superficial velocity, often noted j_i or sometimes, like in this report, using the notation U_S. The superficial velocity of a phase is the velocity that the phase should have, if it were the only phase in the flow, to obtain the same flow rate. It is calculated as:

$$U_S = \frac{Q}{A} \tag{2.1}$$

where Q is the volumetric flow rate of the considered phase and A is the pipe cross section. They are the most relevant parameters, at least, when the experimental conditions do not change the surface tension or the viscosity. A valuable description of multiphase flows is provided in Kolev (1993b) and Kolev (2007) where flow pattern transitions are described.

Figure 2.1 has been extracted from Baker (1954) and shows a flow pattern map for horizontal air-water pipe flows, depending on the gas and liquid superficial velocities. Similarly, Figure 2.3 shows the flow pattern map for vertical gas-water pipe flows. It should be kept in mind that boundary lines in this flow regime map are not that sharp in reality. They are actually transition zones to express the unstable configuration of both phases. It should also be mentioned that it exists no universal flow regime map, even for a simple geometry like a pipe, as many parameters are involved in transitions from a configuration to another one (roughness, pipe inclination, etc.). Moreover, as it can be often seen, such maps are established for a given geometry, and all attempts to make dimensionless flow maps failed since transitions are not based on the same characteristic numbers. However, it will be assumed in this work that only one configuration can exist for a given set of flow parameters. Nevertheless, a common behaviour can be highlighted: with the increase of gas speed, the flow aspect will be more diffused and will eventually lead to an annular flow.

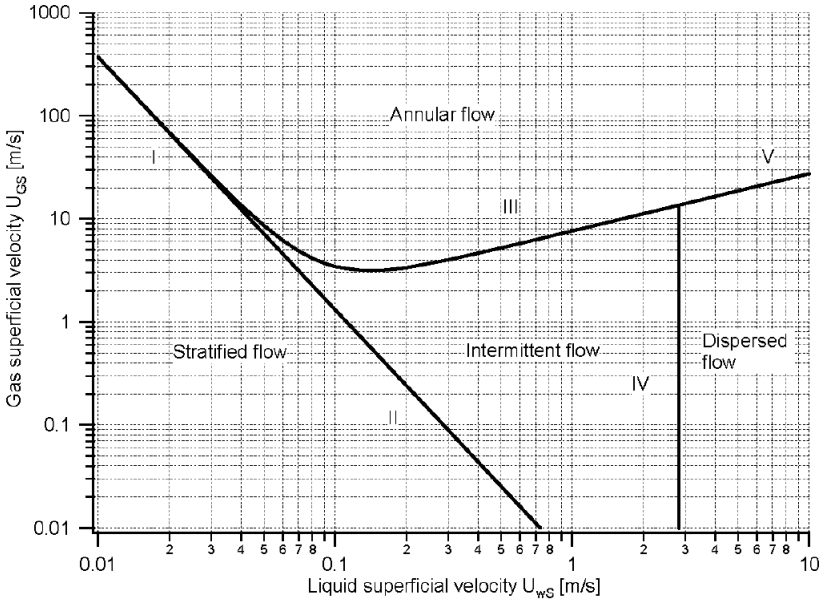

Figure 2.1: *Flow pattern boundaries proposed by Baker (1952) for air-water for 4 in. (101.6 mm) diameter pipes*

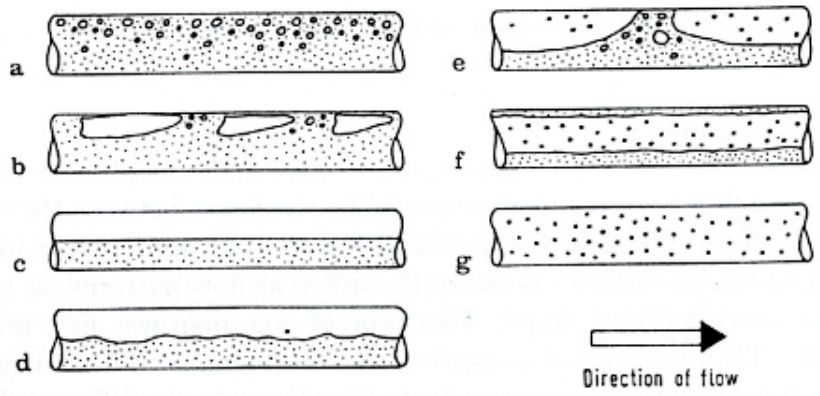

Figure 2.2: *Flow patterns in a horizontal unheated tube.*
a. Bubble flow; b. Plug flow; c. Stratified flow; d. Wavy flow; e. Slug flow; f. Annular flow; g. Disperse flow
Source: Baehr H. D. (2011)

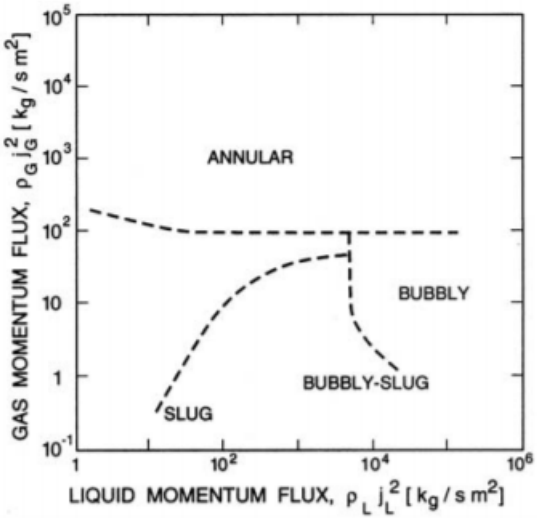

Figure 2.3: *Hewitt and Roberts (1969) vertical pipe flow pattern boundaries for a 3.2 cm air-water flow*

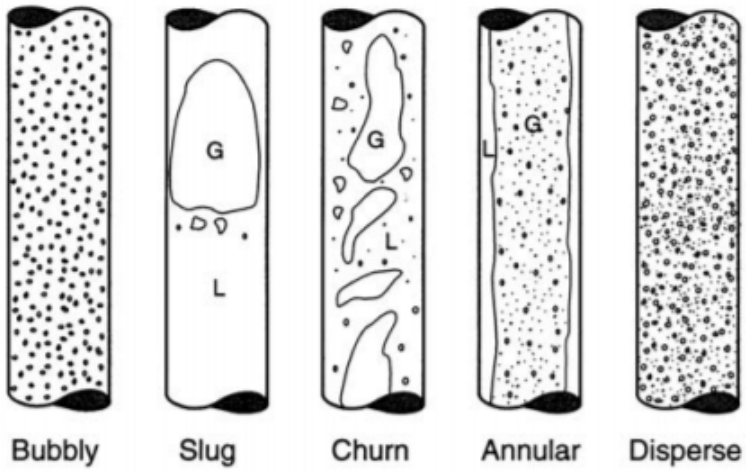

Figure 2.4: *Two-phase flow patterns in a vertical pipe - Adapted from Weisman (1983)*

Figure 2.2 shows the flow aspect for sectors that appear on Figure 2.1 for horizontal flows and Figure 2.4 shows the flow aspect for the sectors that appear on Figure 2.3 for vertical pipes. Notice that for a horizontal or near horizontal pipe, the heavier phase phase can sometimes appear in top regions of the pipe. This PhD. focuses on the disperse flow regime as it can generate all the other flow patterns. The code developed is able to start a disperse flow regime which can change into a wavy stratified flow or even an annular flow if all the conditions are met. However these sorts of flow are significantly more complex to obtain, and only a brief proof of concept will be provided in Chapters 4.1 and 4.4 of the thesis.

2.1.2 Secondary flows

In fluid mechanics, a secondary flow is a flow occurring in another plan/direction than the main one. This is illustrated by Figure 2.5. Three kind of secondary flows have been described by Prantl (1952):

- Secondary flows of first kind are generated by a significant pressure difference in an other direction than the main one, or for rotating flows (in hurricanes for instance).
- Secondary flows of second kind are generated by turbulence and by geometry effects; this is this one which is of interest for separated pipe flows.
- Secondary flows of third kind are generated by oscillations in a stationary fluid.

As the pipe section is partially obstructed by a pool, secondary flows occur in the gas region. Predicting this, is important to evaluate the wetting due to impingement of small droplets that are more likely to follow small convective structures of the gas flow. Their origin is probably linked to the kinetic turbulent energy, which is anisotropic and interact with walls and the interface. Flores *et al.* (1995) present secondary flows in various flow patterns. Brown *et al.* (2009); Verdin *et al.* (2014) describe the simulation of droplets entrainment and deposition in a large (38 in.) pipeline. A secondary flow was enhanced, due to the presence of interfacial roughness varying with position and was assumed to be related to the local thickness of the liquid film.

2.1.3 Dimensional analysis

To characterize the flows and to quantify the balance of forces involved in multiphase flows, a dimensional analysis is often performed. This can be done to evaluate the order of magnitude of various terms in equations to obtain approximations. It can also be used to produce non-dimensional equations (or variables).

One of the most usual way to establish such an analysis is by using the Buckingham Π-Theorem. It consists in expressing a set of physical quantities which are assumed to influence the problem (thereafter designated by "n"), and "k" the number of fundamental dimensions involved (such as "Time", "Length" and so on). The theorem states that $n - k$ non-dimensional numbers can be

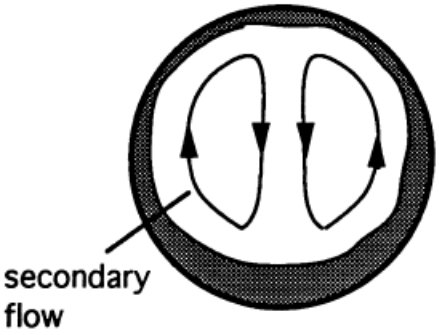

Figure 2.5: *Secondary flows in pipes contributes to wet the walls*
Source: Vij et al. (1996)

created to describe the physical phenomenon that link them. This is done by taking a sub-set k of variables over n possible ones. It is recommended to discard variables made of many dimensions. New dimensionless variables are generated by doing the product of all the remaining variables, elevated to an unknown power. A system is then solved to determine the values of the unknowns, making the overall number dimensionless.
An example is provided below, establishing a relation linking the drag force "F" exerted on a particle: it can be inferred from daily observations that parameters influencing such a force would be the (relative) flow velocity, the particle diameter, the flow density and the flow viscosity. This leads to the introduction of the following variables:

$$F, V, D, \rho, \mu \ .$$

Here, $n = 5$. The following Table 2.1 is used to determine how many independent dimensions there are:

Table 2.1: *Dimensions of some variables*

variable	dimension
force F	$M.L.T^{-2}$
velocity V	$L.T^{-1}$
diameter D	L
density ρ	$M.L^{-3}$
viscosity μ	$M.L^{-1}.T^{-1}$

A maximum of three dimensions are involved in all these variables. Therefore $k = 3$. The theorem says $n - k = 2$ dimensionless variables can be constructed. The two variables chosen to be discarded which will serve as a base for the non-dimensionalization process, are the force F and the viscosity μ. Two independent dimensionless numbers Π_1 and Π_2 can then be expressed as follow:

$$\Pi_1 = F.V^{\alpha}.D^{\beta}.\rho^{\gamma} \tag{2.2}$$

$$\Pi_2 = \mu.V^a.D^b.\rho^c \tag{2.3}$$

The sum of the exponents must be equal to zero, to obtain a dimensionless number. For the first "Π-variable", the following system (3 equations and 3 unknowns) can be written:

$$\begin{cases} M: \ 1+\gamma = 0 & \text{(2.4a)} \\ L: \ 1+\alpha+\beta-3\gamma = 0 & \text{(2.4b)} \\ T: \ -2-\alpha = 0 & \text{(2.4c)} \end{cases}$$

which leads to $\alpha = -2$, $\beta = -2$, and $\gamma = -1$.
The first dimensionless number is:

$$\Pi_1 = F.V^{-2}.D^{-2}.\rho^{-1}$$

This expression describes the drag coefficient, usually expressed by introducing the particle area ($S = \pi D^2/4$) as:

$$C_D = \frac{2F\pi}{\rho.S.V^2} \tag{2.5}$$

Note that the Π-theorem does not allow to retrieve the multiplicative constants as it deals with the dimensions only.

For the second non-dimensional number Π_2, the system is the following one:

$$\begin{cases} M: \ 1+c = 0 & \text{(2.6a)} \\ L: \ -1+a+b-3c = 0 & \text{(2.6b)} \\ T: \ -1-a = 0 & \text{(2.6c)} \end{cases}$$

which leads to $a = -1$, $b = -1$, and $c = -1$. The second dimensionless number is:

$$\Pi_2 = \mu.V^{-1}.D^{-1}.\rho^{-1}$$

This is in fact the (droplet-based) Reynolds number inverted, which can be expressed in the form of Equation 2.7, by introducing $\nu = \mu/\rho$.
Non-dimensional numbers thus created often describe a balance between various physical forces. This has lead to numerous named numbers (Stokes Number, Reynolds Number, Froude Number, Weber Number to name but a few). To characterize the overall turbulent state of a flow, the Reynolds number is used. It compares the inertia effects (momentum quantity) to the viscous effects (viscous friction that counters the momentum). It exists several versions of this number to account for the various scales on which the comparison can be done. The most common one is the following:

$$Re = \frac{UL}{\nu} \tag{2.7}$$

where U represents, in most cases, the average velocity magnitude, or the far-field velocity value. L is a characteristic distance, often taken as the pipe diameter in pipe flows (sometimes, the turbulence length of establishment can be used) and ν is the kinematic viscosity. There are other relevant non-dimensional numbers for this work, such as the Stokes number, representing the balance between the particle characteristic time against a characteristic time of the carrier flow. Again,

this definition is sufficiently imprecise to account for various estimates of one or both of these specific times. The most usual is the following:

$$St = \frac{\rho_p d_p^2 U}{\mu L} \tag{2.8}$$

where ρ_p is the particle density, d_p is the particle diameter, U the average flow velocity and L a characteristic length. This number is used to characterize the particle response.
The non-dimensionalization process is important in physics as it is both a tool and an indicator of the prevalent forces in a phenomenon.

The friction velocity is widely used to characterize all sorts of flows:

$$U^* = \sqrt{\frac{\tau_w}{\rho}} \tag{2.9}$$

where τ_w is the wall shear stress:

$$\tau_w = -\mu \left. \frac{\partial U_x}{\partial y} \right)_{wall} \tag{2.10}$$

These numbers are very important to qualify any flow, and especially dispersed flows. The following section introduce the basics of particulate flows.

2.1.4 Qualifying a particulate flow

Droplet flows are a subtype of multiphase flows which can be compared to any particle flow. The fact that the particles transported are droplets can have various consequences, such as coalescence, break-up, deformation, evaporation, freezing, wetting, splash, internal circulation, etc. However, most of those droplet-specific aspects can be neglected in simple configurations, which will mainly be the case in this thesis.

A dispersed field such as a gas or a dense particle flow, can be interpreted as a continuum. A continuum can be defined by the continuous variation of the intensive variables when an extensive associated variable varies. This means that if the intensive variable is the density, and the sampling volume an extensive variable, a continuum is present when the density does not vary when increasing or decreasing the sampling volume.

In reality, this is not always the case as it is not always possible to define a meaningful intensive variable. The rule generally used to settle down this matter is given by the Knudsen number:

$$Kn = \frac{\lambda}{D} \tag{2.11}$$

where λ is the mean free path and D the particle diameter. If $Kn < 10^{-3}$, the medium is considered as a continuum and the usual conservation equations can safely be applied.

Once the continuity is ensured, the volume fraction of a dispersed phase can be written as:

$$\alpha = \frac{\pi D^3}{6\ell^3} \tag{2.12}$$

with ℓ the cell characteristic length when assuming a quad-based mesh. Otherwise it is the ratio of the cumulated particle volume in a cell divided by the cell volume. According to Crowe *et al.* (1998), a flow is said dilute if $\alpha < 0.001$, collision-dominated if $0.001 < \alpha < 0.1$ and contact-dominated if $\alpha > 0.1$. Section 2.3.3 details how the collisions can be handled in case of a collision-dominated flow.

Descriptive statistics of particulate flows

Generally, a particulate flow is constituted by a large number of particles of various shapes, sizes, and possibly of various materials. Before going further into the study of particulate flows, it is necessary to detail first how such flows are commonly described.
The main parameter associated with a particle is its diameter. Particle-Size Distributions (PSD) are used to qualify the sizes of many particles. They can be discrete or continuous. The shape of the distribution is given by a function $f(D)$. The usual descriptive statistics applies:
the $n^{th.}$ moment of the distribution is expressed by the following formula:

$$\mu_n = \int_0^{D_{max}} (D - \mu_0)^n \, f\,(D)\, dD \tag{2.13}$$

where D represents a particle diameter. A very valuable review of the various approaches for particulate flows has been performed by Loth (2000).

How to measure a statistical property in a Lagrangian flow

It is often useful to recover volume averaged quantities from a Lagrangian representation of a particulate flow. Results thus obtained could be compared to the results one could obtain with an Eulerian approach.

The choice of the averaging volume is not straightforward: the volume must be large enough so the averaged property does not vary much with the chosen volume. But it should not be too large compared to the domain, otherwise no significant variations can be seen over the domain. The Poisson distribution can be used to establish a confidence level. The probability of having N particles in a flow with a concentration n of drops per cubic meter, in a volume V is therefore:

$$P\,(N) = (nV)^N \, exp\,(-nV)\,/N! \tag{2.14}$$

as an example, for a flow with a concentration $n = 10^8$ drops per cubic meter, if the sampling volume V is a cube of side of 3 cm (i.e.: $V = 2.7 \cdot 10^{-7}\ m^3$), then the probability that there are between 2700 and 3300 drops in the domain is about 49.5 %, 3000 being enough to evaluate a property such as the mean temperature,

or any value carried by the particles. If s is the standard deviation of the sampling (here about 3000 particles), then the confidence interval at 95% is:

$$I = \left[\overline{T} - 2\frac{s}{\sqrt{N}}; \overline{T} + 2\frac{s}{\sqrt{N}}\right] \tag{2.15}$$

where $\overline{T}$ is the mean value of the random variable T from the sampling size N.

In other words, the mean value is $\overline{T} \pm 5\%$, with a confidence level of 95% , which is statistically significant. In case of collision evaluation, only a fraction of these particles will collide, so the sampling volume should be larger to get reliable collision estimations. Assuming the particle density is homogeneous throughout the domain of averaging, the sampling volume recommended by Crowe *et al.* (1998) is:

$$V^{1/3} \sim \frac{18}{n^{1/3}} \tag{2.16}$$

where V is the sampling volume and n the particle number density. If the volume fraction α is known, then:

$$\ell = D\left(\frac{\pi}{6\alpha}\right)^{1/3} \tag{2.17}$$

then

$$V^{1/3} \sim 18\ell \tag{2.18}$$

The next section introduces the equations to solve multiphase flows, for both the Eulerian and the Lagrangian framework.

2.2 Mathematical formulations

2.2.1 Euler-Euler

Figure 2.6 shows the two non-miscible domains Ω_1 and Ω_2 separated by an interface Γ. The Navier-Stokes equations can be directly applied to each fluid domain:

$$\begin{cases} \rho_i\left(\dfrac{\partial \overline{u_i}}{\partial t} + \overline{u}\cdot\overline{\overline{grad}}\,(\overline{u_i})\right) - \overline{div}\left(\mu_i\left(\overline{\overline{grad}}\,(\overline{u_i}) + \overline{\overline{grad}}^{T}\,(\overline{u_i})\right)\right) + \overline{grad}\,(p_i) = \rho_i\overline{f} & \text{(2.19a)} \\ div\,(\overline{u_i}) = 0 & \text{(2.19b)} \end{cases}$$

with

$$\overline{f} = \overline{g} + \sigma\kappa\overline{n}\delta_\Gamma \tag{2.20}$$

where σ is the surface tension, κ the curvature, $\overline{n}$ is the external normal to the interface. The subscript $._i$ represents each fluid.

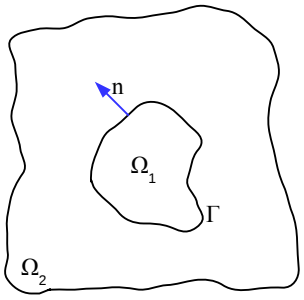

Figure 2.6: *Two non-mixing Fluid descriptive scheme*

As it is numerically expensive to solve the Navier-Stokes Equations, only one velocity field is usually solved for all phases. There is a discontinuity when passing through the interfaces, the density in particular varies between fluids.

Volume of Fluid

The Volume Of Fluid (VOF) method was developed to simulate flows between non miscible phases. Hirt and Nichols (1981), are usually referred as the founder of this approach, even if the first implementation has been done by Noh and Woodward (1976).

This method is based on a transport equation for a phase cell concentration, in the Eulerian framework, see Equation 2.21. An algorithm should be added to the basic implementation of the VOF method to reconstruct the interface, where the volume fraction is between 0 and 1. The most commonly used today is the Piecewise-Linear Interface Calculation (or PLIC) scheme.

$$\frac{\partial \alpha}{\partial t} + U.grad\,(\alpha) = 0 \tag{2.21}$$

where α denotes the cell concentration of one phase. Navier-Stokes Equations still need to be solved in addition to Equation 2.21. One of the advantages of this method is that it conserves the mass of the tracked fluid and allows discontinuous values for α. One drawback of this approach is that the interface is diffusive with most interface reconstruction methods.

Two-fluid approach

When considering the two-fluid approach (also called Euler-Euler model), each phase has its own velocity solved directly along with other physical values such as temperature, density or pressure. Differences between densities may imply a slip velocity at the interface. A similar behaviour of the temperature is also present: the time scale of energy transfer may vary for rapidly changing flow conditions and therefore the two fluids may show different temperatures.

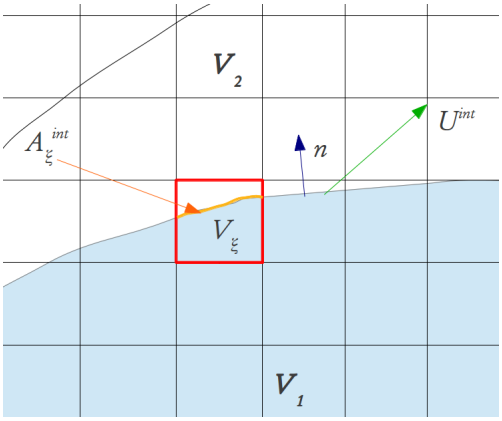

Figure 2.7: *Two Fluid descriptive scheme*

Generally, the pressure difference between phases is not taken into account. However, for applications in this thesis, the pressure difference should be investigated. The main contribution of pressure difference between phases are likely to be the pressure induced by the surface tension (in a curved interface, it is called Laplace pressure) and the pressure due to mass transfer between phases (droplets impingements and entrainment, evaporation and condensation...). The overall dynamic of the flow can also cause pressure variations. The establishment of two-fluid equations is based on volume averaged or temporal averaged[1] mass conservation and momentum equations for each phase. Figure 2.7 shows notations used in their context to set up this method.

- Mass conservation

$$\underbrace{\frac{\partial}{\partial t}\left[\alpha_i \left\langle \rho_i \right\rangle_i\right]}_{(1)} + \underbrace{\nabla \cdot \left[\alpha_i \left\langle \rho_i \overrightarrow{U}_i \right\rangle_i\right]}_{(2)} = \underbrace{a^{int} \frac{1}{A_\xi} \int_{A_\xi} \rho_i \left(\overrightarrow{U}_i^{int} - \overrightarrow{U}_i\right) \cdot \overrightarrow{n}_i^{int} dS}_{(3)} \quad (2.22)$$

  where α_i is the concentration of phase "i" over a control volume V_ξ (commonly called volumetric concentration), $\langle \cdot \rangle_i$ denotes a volume averaging over the whole volume occupied by the phase "i", $\overrightarrow{U}_i^{int}$ is the velocity field of the interface seen by the phase "i" (here integrated over a control volume), $\overrightarrow{n}_i^{int}$ is the normal field over the interface and pointing out the phase "i", a^{int} is the ratio of interface over a control volume, A_ξ is the surface associated with V_ξ

- Momentum balance

$$\begin{aligned} \underbrace{\frac{\partial}{\partial t}\left[\alpha_i \left\langle \rho_i \overrightarrow{U}_i \right\rangle_i\right]}_{(4)} + \underbrace{\nabla \cdot \left[\alpha_i \left\langle \rho_i \overrightarrow{U}_i \overline{\overline{\otimes}} \overrightarrow{U}_i + p_i \overline{\overline{I}} + \overline{\overline{\tau_i}} \right\rangle_i\right]}_{(5)} - \underbrace{\left\langle p_i^{int} \right\rangle \nabla \alpha_i}_{(6)} \\ = \underbrace{\sigma_i^M \left\langle \overrightarrow{U}_i^{exange} \right\rangle_i}_{(7)} + \underbrace{\left\langle F_i^v \right\rangle_i}_{(8)} + \underbrace{\left\langle F_i \right\rangle_i}_{(9)} \end{aligned} \quad (2.23)$$

[1] The principle of ergodicity is generally assumed.

where $\sigma_i^M =$ Term (3) in Equation 2.22.

Term (1) is the volume averaged density, Term (2) the volume averaged mass flux, Term (3) is a source term based on the interfacial mass flux. Term (4) is the transient term and term (5) expresses the fluid forces. Term (6) represents the Laplace pressure (which is resulting from the interface curvature), Term (7) represents the momentum transfer through the interface (which takes into account the mass transfer), Term (8) is the resultant of viscous forces acting on the interface (expression of interfacial shear stress) as well as the pressure from the other phase, and Term (9) describes the external forces acting on phase i.

The main advantage of the two fluid model is that it provides an accurate description of the problem, and allows non dispersive interface simulation. However it requires an extended knowledge and difficult work is required to model closure terms: this frequently leads to non mass conservative closure methods.

Drift-flux model

In that model, the velocities of each phase is related to another. For instance, in terms of fluxes:

$$j_{1-2} = (1-\alpha)\, j_1 - \alpha j_2 \tag{2.24}$$

where j_i expresses the volumetric flux of the $i^{th.}$ phase, and j_{1-2} is the drift flux.

The drift-flux Eulerian expression to compute the droplet transport is usually written as:

$$\frac{\partial C}{\partial t} + \nabla \cdot [(u + v_s)\, C] = \nabla \cdot [(D + \varepsilon_p)\, \nabla C] + S \tag{2.25}$$

where C is the particle mass concentration, u is the carrier fluid velocity, v_s is the particle settling velocity, D is the diffusion coefficient (Brownian Motion), ε_p is the particle Eddy diffusivity (turbulent dispersion) and S accounts for the mass concentration sources.

It should be noted that this expression requires to input or estimate important parameters generally not well known (such as ε_p).

The boundary conditions should also take into account the deposition and/or entrainment/re-suspension. These conditions should be based on the boundary flux (Neumann boundary condition).

2.2.2 Euler-Lagrange

Equation of motion of a single particle

The transport of particles, given by Equation 2.26, is called the BBO, i.e. the Boussinesq, Basset and Oseen equation:

$$m\frac{du_{p_i}}{dt} = mg_i + \underbrace{\mathcal{V}\left(-\frac{\partial p}{\partial x_i} + \frac{\partial \tau_{ij}}{\partial x_j}\right)}_{undisturbed\ flow} + \underbrace{3\pi\mu_p d_p\left[(u_f - u_p) + \frac{d_p^2}{24}\frac{\partial^2 u_{f_i}}{\partial x_j \partial x_j}\right]}_{steady\ state\ drag} + \underbrace{\frac{1}{2}\rho_f \mathcal{V}\frac{d}{dt}\left[(u_f - u_p) + \frac{d_p^2}{40}\frac{\partial^2 u_{f_i}}{\partial x_j \partial x_j}\right]}_{virtual\ mass\ term} + \underbrace{\frac{3}{2}\pi\mu_f d_p^2 \int_0^t \left[\frac{d/d\tau\left(u_{f_i} - u_{p_i} + d_p^2/24 \times \nabla^2 u_{f_i}\right)}{\pi\nu\left(t-\tau\right)^{1/2}}\right] d\tau}_{Basset\ term} + F_{L_i} + F_i \quad (2.26)$$

where $\mathcal{V}$ represents the particle volume, F_{L_i} the lift force and F_i any other force unaccounted for. Note that u_p stands for the instantaneous particle velocity, which includes the fluctuating velocity. The BBO equation can be simplified based on the following assumptions:

- the droplet volume is sufficiently small so that the virtual mass term can be neglected,
- the density of the particles is much higher than the density of the carrier fluid: $\rho_p \gg \rho_f$.

A simple equation can usually be retained to describe the particle motion in the core flow:

$$\frac{du_p}{dt} = \underbrace{\frac{u_f - u_p}{\tau_p}}_{Drag\ effects} + \underbrace{f}_{other\ forces} \quad (2.27)$$

where τ_p is the particle response time defined by:

$$\tau_p = \frac{4}{3}\frac{\rho_p d_{eq}^2}{\mu_G}\frac{1}{C_D \mathcal{R}e_p} \quad (2.28)$$

with d_{eq} the aerodynamically equivalent particle diameter and C_D the drag coefficient. For liquid drops, an alternative τ_p is used:

$$\tau_p = \frac{4}{3}\frac{\rho_p d_{eq}^2}{\mu_G}\frac{C_c}{C_D \mathcal{R}e_p}\left(\frac{1 + \left(\frac{\mu_f}{\mu_p}\right)}{1 + \left(\frac{2\mu_f}{3\mu_p}\right)}\right) \quad (2.29)$$

with the C_c Cunningham slip correction factor:

$$C_c = 1 + \frac{2\lambda}{d_p}\left(1.257 + 0.4e^{-1.1 d_p/2\lambda}\right) \quad (2.30)$$

where λ is the mean free path. The particle response time τ_p expresses the ability for a particle to follow the flow. The added mass is handled by an additional force, proportional to the particle acceleration. Equation 2.27 is valid when the flow seen by the particle has a low Reynolds number. In this regime, Stokes flow approximations apply ($C_D = 24/\mathcal{R}e_p$) and the drag force is proportional to the relative velocity $u_f - u_p$. Near-wall corrections from Ahmadi & McLaughlin (2008) have been applied with the Faxen correction defined as:

$$C_D\mathcal{R}e_p = 24\left[1 - \frac{9}{16}\left(\frac{d_p}{2h}\right) + \frac{1}{8}\left(\frac{d_p}{2h}\right)^3 - \frac{45}{256}\left(\frac{d_p}{2h}\right)^4 - \frac{1}{16}\left(\frac{d_p}{2h}\right)^5\right]^{-1} \tag{2.31}$$

where h is the distance from the particle centre to the nearest wall. For particles of size comparable to the carrier fluid mean free path (or smaller), the Brownian motion has to be taken into account along with the drag slip factor of Cunningham, which depends mainly of the mean free path. The following forces have been used in this PhD work to compute the motion of the particles:

- Drag force that accounts for sphere drag with the Cunningham factor auto-calculated with medium properties, near wall corrections and valid for droplet-based Reynolds numbers less than 1 (the Stokes regime),
- Gravity,
- Saffman-Mei lift force for spheres (Pang & Wei, 2011),
- Virtual mass effects,
- Pressure gradient force,
- Brownian motion, providing the mean free path λ or the medium molecule inter-spacing.

The effects of lift can be important, see Gupta & Pagalthivarthi (2006); the lift force should ideally include the effects of lift due to particles rotation. However, for the sake of simplicity, no droplet rotation was assumed in the simulations performed during this PhD. One of the most common expression for the Saffman lift force is the following:

$$F_{saffman} = 1.61\mu_c D\left|u_i - v_i\right|\sqrt{Re_G} \tag{2.32}$$

where Re_G is the shear Reynolds number:

$$Re_G = \frac{D^2}{\nu_c}\frac{du}{dy} \tag{2.33}$$

The numerical integration commonly used to solve Equation 2.27 is detailed in Graham & James (1996). The instantaneous particle velocity u_p includes the particle fluctuation u'_P, which arises from the turbulent dispersion influencing the droplets (see Section 2.3.1).

Since only particles diameters vary in the current document, their behaviour can be associated with their size. For small droplets, where the dimensionless particle relaxation time:

$$\tau_p^+ = \frac{\tau_p \left(U^*\right)^2}{\nu_f} \tag{2.34}$$

is less than 0.3, the Brownian motion, the Stokes-Cunningham drag, and the thermophoretic forces are important. For medium size droplets ($0.3 \leq \tau_p^+ \leq 20$), Stokes drag, thermophoretic, lift/pressure gradient, centrifugal forces and the conservation of angular momentum along with the turbulent dispersion should be taken into account. For large drops, where $\tau_p^+ > 20$, the Stokes drag, lift/pressure gradient, centrifugal, mass added forces, conservation of angular momentum and weight should be included (Matida *et al.*, 2000).

Two-way coupling

Particles do interact with their surroundings. They change the flow and the turbulent fields they cross. This is often called the "two-way" coupling as opposed to the "one-way" coupling (particles only are affected by the flow), and the "four-way" coupling, which includes the particle-particles collisions. For the two-way coupling, new source terms must be added to the momentum and turbulence equations of the carrier phase. Berlemont *et al.* (1990); Lain & Sommerfeld (2003); Nasr & Ahmadi (2007) proposed the following equations (source terms):

$$S_{u_i}^p = -\frac{1}{\rho_f V_{cell}} \sum_{k=1}^{N^P} m_k N_k \Delta t_L \times \sum_{n=1}^{N^T} \frac{\left[(u_i^p)_k^{n+1} - (u_i^p)_k^n\right]}{\Delta t_L} - g_i \left(1 - \frac{\rho_f}{\rho_p}\right) \tag{2.35}$$

$$S_k^p = \overline{u_i^p S_{u_i}^p} - \overline{u_i}\,\overline{S_{u_i}^p} \tag{2.36}$$

$$S_\varepsilon^p = C^{\varepsilon 3} \frac{\varepsilon}{k} S_k^p \tag{2.37}$$

with $C^{\varepsilon 3}$ not clearly determined, but Lain & Sommerfeld (2003) suggested a value of 1.87. The next section discusses in more details how particles interacts with the carrier flow and other particles.

2.3 Particle phenomenology

2.3.1 Particles and turbulence

Particle induced reduction or enhancement of the turbulence

Particles has been found to alter significantly the turbulence, either by attenuation or by increasing its intensity. It is mainly thanks to Laser Doppler Velocimetry (LDV) techniques from the 1970s and later with their democratization that accurate predictions were possible, even though some attempts in measuring these effects using hot-wire were carried out by Hetsroni & Sokolov (1971).

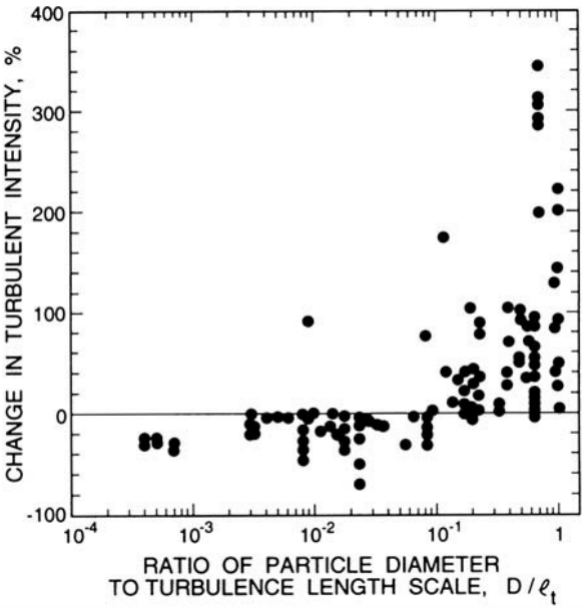

Figure 2.8: *Turbulence modulation by particles ; taken from Crowe et al. (1998)*

Figure 2.8 is a summary of various data on turbulence modulation up to 1989, that is taken out from Crowe *et al.* (1998). Some empirical models are available to account for the turbulence modulation.

It has been shown by various authors (Tsuji *et al.*, 1984; Vreman, 2015) that the particle size determine the attenuation or the enhancement of turbulence. Large particles have been found to heavily enhance the turbulence, while for the small particles, the effects opposite.
Despite various estimations, there are currently no firm methods able to correctly reproduce all the effects responsible for the turbulence modulation and therefore, all models currently available have limitations or can not easily be implemented.

Turbulent dispersion

In turbulent flows, the carrier fluid velocity influences highly the particles motion. Even if Lagrangian statistics can be obtained (Govan *et al.*, 1989), it is often easier to obtain the Eulerian description of the main fluid fluctuations rather than the Lagrangian fluctuations of the disperse phase. Intuitively, as the particles are carried by the fluid, the Lagrangian statistics should be related to the Eulerian ones. This implies that the Lagrangian auto-correlation should converge to the Eulerian auto-correlation when a particle becomes a “fluid particle". However, for large particles or when the ratio of densities becomes important, the correlation with the Eulerian field should become more distant, as particles are more likely to have uncorrelated velocities with the flow. Based on the particle velocity field (Crowe *et al.*, 1998), the auto-correlation function R_P can be defined as:

$$R_P(x,t) = \frac{\langle u_P(x,t) u_P(x+\delta x, t+\delta t)\rangle}{\langle u_P(x,t)^2\rangle} \tag{2.38}$$

where u_P denotes the particle instantaneous velocity. Considering the stationary turbulent field imposed by the flow, the particle auto-correlation function can be written:

$$R_P(x,t) = R_E(x) \times R_L(t) \tag{2.39}$$

where R_E and R_L express the Eulerian spatial and Lagrangian temporal auto-correlations, respectively. The determination of R_L can be obtained in different ways. For instance, Govan *et al.* (1989) provide a measurement of this correlation, with the following general form:

$$R_L(t) = e^{-\frac{t}{\tau}} \tag{2.40}$$

where τ can be taken as τ_P, the particle relaxation time. Other formulations exist, such as the Berlemont *et al.* (1990) one, which uses Frenkiel's family of correlation function. (Gouesbet & Berlemont, 1998) did a study of particle behaviour in turbulent flows, and summarize various expressions of the Lagrangian auto-correlation and their effects on the particle dispersion. The determination of R_E is obtained from the two-point auto-correlation function for homogeneous isotropic turbulence. In general, the same family of functions used for R_L can be used for R_E, scaled with the fluctuation intensities.

Taylor (1922) developed the idea of linking the Eulerian turbulence statistics to the Lagrangian turbulent dispersion for a homogeneous isotropic turbulent flow, see also Dosio *et al.* (2005) and Koeltzsch (1998). Taylor was thus able to determine the variance of the particle displacement in any direction and for small Stokes number particles:

$$2\sqrt{var\left(u'\right)}\int_0^t\int_0^{t'} R_L^r\left(\tau\right)d\tau dt' = \begin{cases} \bar{u'^2}t^2 & \text{if } t \ll T_L \quad (2.41a) \\ 2\bar{u'^2}T_L t & \text{if } t \gg T_L \quad (2.41b) \end{cases}$$

where *var* expresses the variance (using a spatial average) and u' denotes the fluctuating velocity. The superscript r shows that only the radial direction is considered here. This spreading result can be recovered using the Langevin equation:

$$\frac{du}{dt} = -\frac{u}{T_L} + \sqrt{\frac{2.var(u)}{T_L}}n(t) \tag{2.42}$$

where $n(t)$ is a Wiener process (Szabados, 2010) and T_L is the Lagrangian integral time scale:

$$T_L = \int_0^\infty R_L\left(\tau\right)d\tau \tag{2.43}$$

Once determined, the auto-correlation function can be used to alter the particle velocity (obtained from Equation 2.27), by adding a fluctuating part u'_P:

$$u_P^{n+1} = u_P^n \cdot R_P + u'_P \tag{2.44}$$

with u'_P defined as:

$$u'_P = u_e\sqrt{1 - R_P^2}\xi \tag{2.45}$$

ξ is a random number following the standard normal distribution and $u_e = \sqrt{2k/3}$, which is representative of an eddy velocity.

Other approaches are possible to evaluate R_L. One of the most common ones is to consider the flow as a set of eddies interacting with any particle in its vicinity. This interaction generates a constant fluctuation velocity on the particle until it leaves the eddy or until the eddy dies. When this happens, another random velocity is applied to the particle. A popular scheme for this eddy interaction model is discussed in Gosman & Ioannides (1983), where the constant eddy-lifetime is based on a linear approximation of R_L. Using the "constant Eddy lifetime model" is similar as having the following linear correlation (Graham & James, 1996):

$$R_L(\delta T) = 1 - \frac{\delta T}{2T_L} \tag{2.46}$$

The time of interaction, i.e. the laps of time during which a particle keeps the same fluctuation, can be written as:

$$T_{interaction} = min\left(\tau_c, \tau_e\right) \tag{2.47}$$

where τ_c is the crossing time and τ_e the eddy-lifetime:

$$\tau_e = 2T_L \tag{2.48}$$

with T_L the Lagrangian integral time scale:

$$T_L = C_L \frac{k}{\varepsilon} \tag{2.49}$$

Different values of time scale constant C_L can be used, depending on the type of turbulence model selected. In most cases, a value around 0.32, as proposed by Hinze (1975), is suitable. Note however that the FLUENT (2014) manual specifies a default value $C_L = 0.15$ and advises to apply $C_L = 0.30$ when using the Reynolds stress turbulence model.

OpenFOAM assumes that the Lagrangian integral time scale T_L is zero at the walls. However, it has been proven that this assumption is not valid (Bocksell & Loth, 2006). Thus, for $y^+ < 5$, a constant adjustable value T_L^+ is usually taken around 2.5. For $y^+ > 100$ the description from Equation 2.49 applies. For $100 < y^+ < 5$, a quadratic correlation such as the one suggested by Kallio & Reeks (1989) and applied in this work, can be used:

$$T_L = \begin{cases} 2.3\left(\sqrt{\frac{\nu_f}{\epsilon}}\right)_{wall} & \text{if } y^+ \leq 5 \quad (2.50a) \\ \left(7.122 + 0.5731 \times y^+ - 0.00129 \times y^{+2}\right)\left(\sqrt{\frac{\nu_f}{\epsilon}}\right)_{wall} & \text{if } 5 < y^+ < 100 \quad (2.50b) \\ C_L \frac{k}{\varepsilon} & \text{otherwise} \quad (2.50c) \end{cases}$$

Note that there is a discontinuity for $y^+ = 5$ in the model presented here. However, this discontinuity does not affect much the results. T_L could have been

made continuous, for instance, with a quadratic interpolation, as proposed by Lecrivain & Hampel (2012).

As stated previously, a particle will follow the same velocity fluctuation until the eddy dies (interaction time greater than eddy lifetime) or until the drop leaves the eddy. When the particle leaves the eddy before the end of the eddy lifetime, which is expected to be more frequent for “large" particles, it will follow a new velocity fluctuation. The “crossing time” τ_c is the time for a particle moving at the eddy relative velocity, to travel at the characteristic length of the eddy L_e:

$$\tau_c = -\tau_p \ln\left(1 - \frac{L_e}{\tau_p \left|u_f - u_p\right|}\right) \tag{2.51}$$

with

$$L_e = C_\mu \frac{k^{3/2}}{\varepsilon} \tag{2.52}$$

Using Equations 2.48 and 2.51, the local particle turbulent interaction time can be evaluated from Equation 2.47.

The models described above are all based on the turbulent kinetic energy. This approach can show limitations for cases where the turbulence is anisotropic (Kallio & Reeks, 1989). Although not applied for this work, enhanced models use the Reynolds tensor components. For a numerical approach, this requires the use of a Reynolds Stress model or the use of the Boussinesq approximation. For pipe flow studies, it is a common practice to use the radial component and to define a radial Lagrangian integral time scale such as in Tian & Ahmadi (2007):

$$T_{L_r} = C_2 \frac{\overline{v'v'}}{\varepsilon} \tag{2.53}$$

where C_2 is, according to Matida *et al.* (2000), close to 1.

Thanks to DNS and measurements of the fluctuations in the layer $10 < y^+ < 30$, a trend that explains the enhanced deposition has been found. By trying to account and characterize the seeps (pushing particles to the wall or holding them in a close-wall layer) and burst events (moving particles away from the wall) that are playing an important role in the particle deposition and concentration. An interesting review and a simple stochastic model to account for these events is proposed by Jin *et al.* (2015). This can seen as having a skewed Gaussian distribution to represent the near wall fluctuations for both radial and axial fluctuations. It means that there are more fluctuations pushing the droplets towards the wall in that layer, while above $y^+ = 50$ the fluctuations push the drops away from the walls.

Turbophoresis

The turbophoresis phenomenon is related to the average particle drift from high turbulence regions towards low turbulence regions.
The usual expression of this force is the following:

$$F_{turbo} = -\frac{1}{2}\rho_p \frac{\pi d_p^3}{6} \frac{\partial \overline{u_r'^2}}{\partial r} \tag{2.54}$$

This expression directly appears in Eulerian formulations, and is generally only seen as a consequence of the turbulence fluctuations in Lagrangian approaches.

In cases of pipe flows, this effect leads to push particles near the wall. However, Vreman (2007, 2015) has shown this near-wall build up concentration is function of the mass loading of particles: the higher the mass loading, the lesser the turbophoretic effect becomes visible. It can even become negligible. In low particle concentration, this is a major effect, leading to concentrations up to 300% higher near the wall than at the centre.

2.3.2 Diffuse dispersion - Brownian motion

The Brownian motion is the main actor in the diffuse dispersion of droplets. Any molecule having a temperature, experiences a small random motion or oscillations. For particles small enough to see the carrier fluid as a discontinuous phase of agitated particles, the Brownian force is the force resulting from the collisions of such fluctuating particles. A common formulation for this force can be written, considering the vector F_b of components F_{b_i}:

$$F_{b_i} = \zeta_i \sqrt{\frac{\pi S_0}{\Delta t}} \tag{2.55}$$

where ζ_i are zero-mean, unit-variance-independent Gaussian random numbers and S_0, the spectral density, defined as:

$$S_0 = \frac{216 \nu k_B T}{\pi \rho_F {d_p}^5 \left(\frac{\rho_P}{\rho_F}\right)^2 C_c} \tag{2.56}$$

with the Cunningham slip correction factor:

$$C_c = 1 + \frac{2\lambda}{d_p}\left(1.257 + 0.4e^{-1.1 d_p/2\lambda}\right) \tag{2.57}$$

When a particle no longer sees the carrier fluid as a continuous medium, the “no-slip" condition stops being valid and the Cunningham slip factor is used to correct this.

The diffusion process has been characterized by Einstein (1905) as well as the square root of the geometric mean of the squares of the displacements in a direction (variance of displacement), as it follows:

$$\sqrt{\overline{x^2}} = \sqrt{2Dt} \tag{2.58}$$

where D is the diffusion coefficient. To test the Brownian motion model implemented in OpenFOAM, a droplet size distribution has been chosen to include sub-micron-particles, with droplets ranging from 1×10^{-9} m to 68×10^{-6} m.

This makes the Brownian motion a slow diffusion process compared to the turbulent dispersion or the particle characteristic time. However, it plays an important role in deposition and collisions of sub-micron to micrometer particles sizes.

2.3.3 Collisions and coalescence

Collisions can occur only when the particle density is high enough. According to Crowe *et al.* (1998), the collision-dominated domain begins when the particle volume fraction is greater than 0.001. The collisions are also function of the particle relative fluctuating velocity, as the flow surrounding colliding particles is almost the same. Neglecting the Basset historical term, the particle fluctuation relative to the flow is function of the particle characteristic time and the Eulerian autocorrelation R_L, usually known. Based on this, it becomes possible to evaluate the particle-particle relative fluctuation:

$$\overline{v_1 v_2} = \left\langle u'^p\left(x\right) u'^p\left(x+r\right)\right\rangle \tag{2.59}$$

However, large particles are more uncorrelated with the flow, as represented in

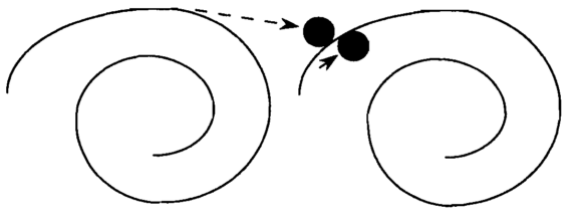

Figure 2.9: *Two particles colliding with uncorrelated fluctuating velocities; source: Kruis & Kusters (1997)*

Figure 2.9. Kruis & Kusters (1997) proposed an expression for $\overline{v_1 v_2}$ for small and large droplets (described later in this section).

When two particles are getting close to one another, the fluid pressure between these particles increases. This generates a repulsive force expressed by:

$$F_{approach} = -\frac{3\pi\mu_c R_1.R_2\frac{dh}{dt}}{2h_0} \tag{2.60}$$

where R_1 and R_2 are the particle radius of the colliding particles, $\frac{dh}{dt}$ expresses the rate at which the particles are approaching and h_0 is the half distance between the particles.

Binary collision settings

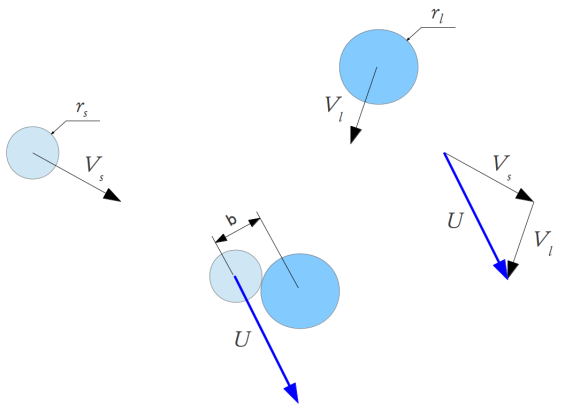

Figure 2.10: *Droplet-droplet collision settings.*

Collision outcome

The terminology used to describe the outcome of a droplet-droplet collision (bouncing, coalescence, disruption and fragmentation) will be identical to those introduced by Abbott (1977). Figure 2.10 presents the settings usually used to evaluate the collision between two droplets. The distance b refers to the distance centre-to-centre at collision point, taken perpendicularly to the vector U, which is the resultant velocity, vectorial composition of individual drops just before collision. The collisional kinetic energy (denoted CKE) for two droplets of same fluid is defined in Orme (1997) as follows:

$$CKE = \frac{\rho\pi}{12}\left(\frac{D_l^3 D_s^3}{D_l^3 + D_s^3}\right)(V_l - V_s)^2 \tag{2.61}$$

where D denotes droplet diameters and the subscripts l and s represent the large and small droplets, respectively.

For a collision to happen, the CKE must be such that the force due to the gas layer between the approaching particles generates can be overcame.

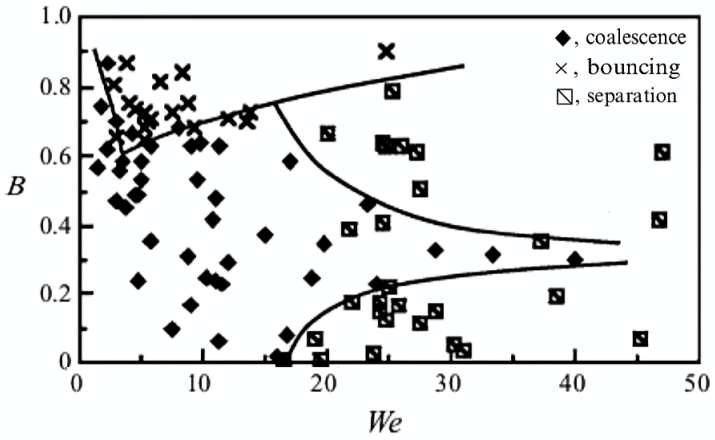

Figure 2.11: *Droplet-droplet collision regime map at 1 atm.*
Source: reproduced from Qian & Law (1997)

Figure 2.11 is a droplet-droplet collision regime map (for two particle of the same size), where the parameter $B = \frac{b}{2R}$ is a non-dimensional number characterizing the collision angle, for $B = 0$ is a head-on collision and $B = 0.5$ is a collision with an angle of $45°$. In this graph, the Weber number is mainly an indication of the velocity of the impact.

Coalescence expresses the fact that all collision energy and the energy necessary to droplet shape-change is completely dissipated. According to Orme (1997), the shape-change-energy is expressed by comparing the difference of drop surface energy (assuming that all drops have a spherical shape), and is given by Equation 2.62.

$$\Delta S_\sigma = \pi\sigma \left(\left(D_l^2 + D_s^2 \right) - \left(D_l^3 + D_s^3 \right)^{\frac{2}{3}} \right) \tag{2.62}$$

Thus, the total collisional energy E_T is defined as the sum of CKE and ΔS_σ. Several expressions depending on this parameter express the coalescence efficiency.

Modelled collisions

Droplet-droplet collision algorithm

The algorithm (shown on Figure 2.12) applied every 0.1s (for each snapshot) to determine collision events is now described briefly.
Let us consider that the distance between two droplets at position $\overrightarrow{X_1}$ and $\overrightarrow{X_2}$ is defined with the following objective function:

$$f(t) = \left(\overrightarrow{X_2} + t \times \overrightarrow{V_2} \right) - \left(\overrightarrow{X_1} + t \times \overrightarrow{V_1} \right) \tag{2.63}$$

The following algorithm can be applied for each snapshot:

- select a parcel P_1 of diameter d_1
- select another parcel (so the pair check is unique) P_2 of diameter d_2
- for t in $[0, t_{Box}[$, minimize Equation 2.63, with $t_{Box} = \frac{L_{Box}}{2\langle V \rangle_{t_i}}$

- if $f\left(t_{min}\right) \leq C \times D_{interaction}$, where $C = N^{1/3}$ is a scaling factor, with N the number of real drops in the box, and $D_{interaction} = \left(d_1 + d_2\right)/2$

  If mono-dispersed drops are evenly distributed in a box, then the distance between drops varies with the cubic root of the number of drops in this volume. The parcel behaviour is representative of the actual behaviour of the drops. Increasing the interaction distance (thus increasing the occurrence of the collisions) is similar to reduce the distance between drops.

If ($\|V_2 - V_1\| > \epsilon$) then:

- increase the number of interactions (by one)
- set the time of interaction[2] as:

$$\tau_{interaction} = \frac{\sqrt{2R_{int}^2 + f\left(t_{min}\right)^2}}{\left\|\overrightarrow{V_2} - \overrightarrow{V_1}\right\|} \tag{2.64}$$

At the end of the algorithm the number of parcel interactions for one snapshot is obtained. This process is repeated for all snapshots. This leads to an array of interaction numbers (and interaction times) over which an average value is calculated. Note that this “average” value is not a time average, but rather a “snapshot" average. To get a proper time average, the number obtained is divided by a “particle transit time" based on the length of the box L_{Box} and the average velocity in this box $\langle V \rangle_{Box}$:

$$t_{transit} = \frac{L_{Box}}{\langle V \rangle_{Box}} \tag{2.65}$$

[2] the time a drop is within the interaction distance

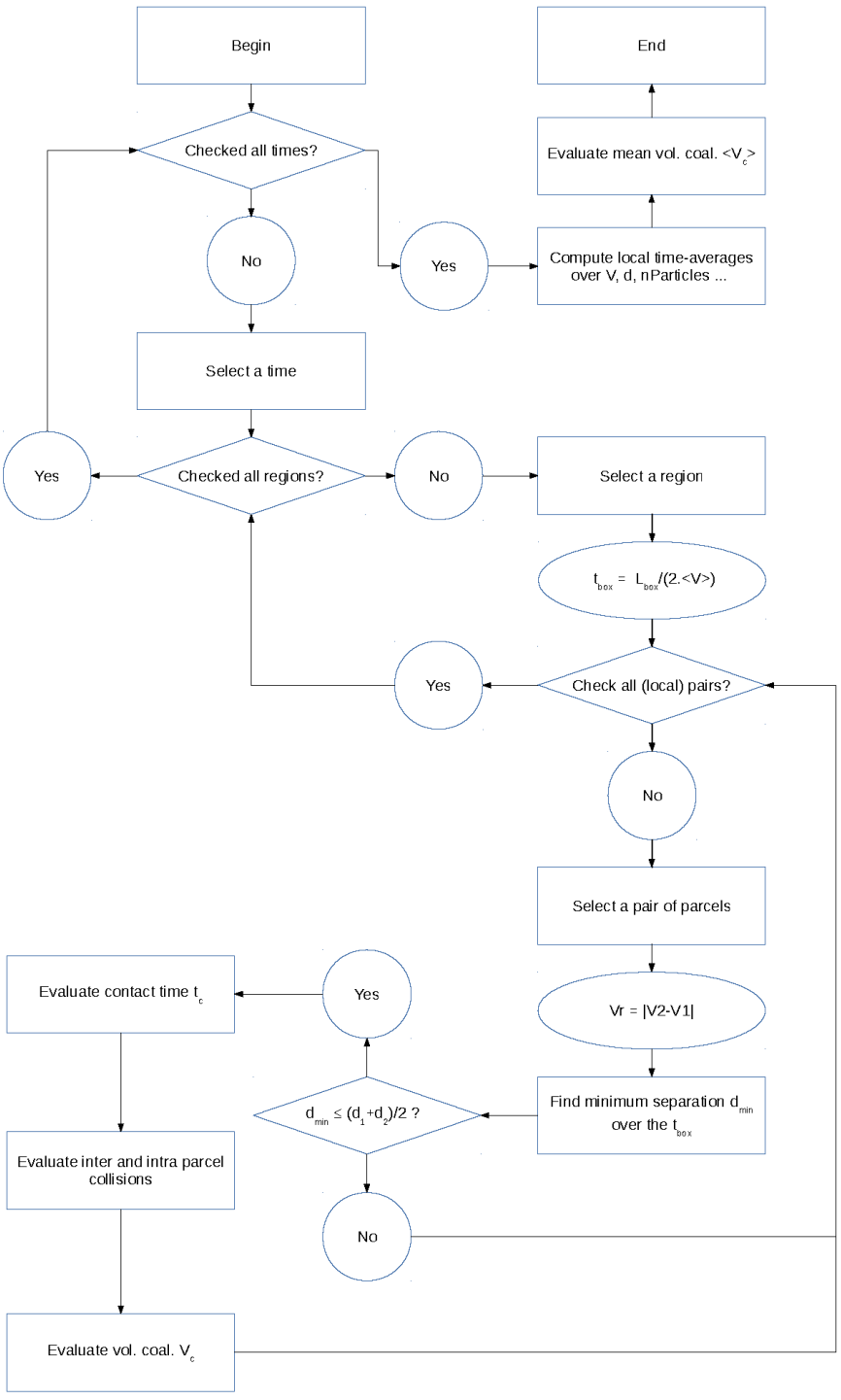

Figure 2.12: *droplet crowding algorithm*

The “transit time" is the time required for a set of drops to cross the box length (L_{Box}). This “transit time" is different from the “residence time", which is the time required for a drop to leave a box, following its curvilinear pathline. For this calculation, it is assumed that the box length is in a direction parallel to the main flow direction. The number of parcel “interaction" per second being obtained, the number of colliding drops per seconds needs to be retrieved. Several methods are possible:

- Use a constant C value so that the collision distance is corrected (enlarged) to take into account the fact that the *effective* separation of droplets is smaller than the separation distance of the parcels.
- Use the particle number per parcel carried by each parcel. When an interaction of a pair of parcels is determined, one could say that the actual number of droplet collisions is determined by the smallest number of particles per parcel of both parcels.

A consequence of using the parcel approach is that both the first and the second approaches lose accuracy if the flow becomes too dilute. Using this algorithm over a long time and using a large number of snapshots would, however, increase the chances of getting an event but would make the whole calculation impractical due to the time and resources required.

Collision correlations

Another approach to evaluate the collisions is to use correlations relating the particle concentration number, the velocity of the particles relative to each other (of which turbulent effects are often the main contributor) to the collision rate. Kruis & Kusters (1997); Sommerfeld (2001) summarized the two most common correlation-based models used: the model of Abrahamson (Abrahamson, 1975) and the Saffman model (Saffman & Turner, 1956). Most of the correlations providing the number of collisions per seconds between species i and j are computed using the following expression:

$$N_{ij} = \beta n_i n_j \tag{2.66}$$

where β is the collision frequency, dependent on the particle sizes and relative velocities, etc. There are several methods to estimate this parameter.

Here are the steps to be followed in this order, to compute the Kruis and Kuster’s collision correlation. Before starting, all the fluid and droplet physical properties should be available (ρ_f, ν, $v_f \ldots$) as well as the droplet instantaneous or averaged number concentration fields (thereafter named n_i and n_j, i and j being markers for the droplet size (they could be the same). Note that v_f represents the local carrier flow velocity.

1. Compute the wall distance field

$$y = interpolation(cell\ centers) \tag{2.67}$$

2. Compute and set as field over the whole mesh (values per cross-section if varying) the wall shear stress using Equation 2.10

3. Compute
$$b = \frac{3\rho_f}{2\rho_p + \rho_f} \tag{2.68}$$

4. Compute u^* using Equation 2.9

5. Compute using 2.67 and 2.9
$$y^+ = \frac{yu^*}{\nu} \tag{2.69}$$

6. Compute T_L using Equations 2.50

7. Compute using 2.50
$$L_f = u_f T_L \tag{2.70}$$

8. Compute using 2.70
$$\gamma = 0.183 \left({Re_{L_f}}^{\frac{1}{2}} \right) \text{ with } Re_{L_f} = \frac{u_f L_f}{\nu} \tag{2.71}$$
an alternate expression can be used:
$$\gamma \simeq \frac{L_f}{\lambda_f} \; with \; \lambda_f = u \left(\frac{30\nu}{\varepsilon} \right)^{\frac{1}{2}} \tag{2.72}$$
In practice, both should be computed an compared one another: it may happen that one cannot be used as approximation of the other.

9. Compute for each droplet size involved
$$C_{c_i} = 1 + \frac{2\lambda}{d_{p_i}} \left(1.253 + 0.5 e^{\left(-0.55 d_{p_i}/\lambda \right)} \right) \tag{2.73}$$
where λ is the mean distance between molecules. Note that this expression has been developed for particles in air. For a liquid, as long as the particles (from the dispersed phase) are larger than the molecular size, one can assume that $C_c = 1$. It is assumed that the typical molecular size for a liquid is about $10^{-9}\ m$.

10. Compute for each size involved, and using 2.73
$$\tau_i = \frac{C_{c_i} \left(2\rho_p + \rho_f \right) r_i}{9\mu} \tag{2.74}$$

11. Compute for each size involved, using 2.74 and 2.50
$$\theta_i = \frac{\tau_i}{T_L} \tag{2.75}$$

12. Compute for each size involved, using 2.75 and 2.71 or 2.72

$$\frac{v_i^2}{v_f^2} = \frac{\gamma}{\gamma - 1}\left(\frac{1}{1+\theta_i} - \frac{1}{(1+\gamma\theta_i)\,\gamma}\right) \tag{2.76}$$

13. Compute for each size involved, using 2.68, 2.75 and 2.71 or 2.72

$$\frac{w_{acc}^2}{v_f^2} = (1-b)^2\,\frac{\gamma}{\gamma-1}\left[\frac{(\theta_i+\theta_j)^2 - 4\theta_i\theta_j\sqrt{\frac{1+\theta_i+\theta_j}{(1+\theta_i)(1+\theta_j)}}}{(\theta_i+\theta_j)}\right]\times \left[\frac{1}{(1+\theta_i)\,(1+\theta_j)} - \frac{1}{(1+\gamma\theta_i)\,(1+\gamma\theta_j)}\right] \tag{2.77}$$

Note that Kruis & Kusters (1997) report this expression to be valid for a range of particle whose sizes are ranging from the Kolmogorov scale up to larger ballistic particles.

14. Compute for each size involved, using 2.76 and 2.77

$$2\frac{\overline{v_i v_j}}{v_f^2} = \frac{v_i^2}{v_f^2} + \frac{v_j^2}{v_f^2} - \frac{w_{acc}^2}{v_f^2} \tag{2.78}$$

15. Compute for each size involved, using 2.76 and 2.78

$$w_{shear}^2 = \left(\frac{v_i^2}{v_f^2}r_i^2 + \frac{v_j^2}{v_f^2}r_j^2 + 2\frac{\overline{v_i v_j}}{v_f^2}r_i r_j\right)\frac{\varepsilon}{5\nu} \tag{2.79}$$

16. Compute for each size involved, using v_f as the local carrier flow velocity and Equations 2.79 and 2.77

$$\beta_{acc+shear} = \sqrt{\frac{8\pi}{3}}\,(r_i+r_j)^2\,\sqrt{w_{acc}^2 + w_{shear}^2} \tag{2.80}$$

That final expression is then to be used in Equation 2.66 to compute the particle collision number in collisions per seconds.

This method was used to derive collisions rates using reconstructed particle concentrations, for cases where it was either impossible or inaccurate to use the previously presented algorithm for direct estimations of collisions in a sampling box.

2.3.4 Break-up

The droplet subdivision under the effects of several phenomena is called break-up. Studying the break-up mechanisms is also studying the phenomenon responsible for it. In general, destructive instabilities are often induced friction forces on the droplet, coupled with capillarity effects. A droplet under such charge will have its surface wobbling and its overall shape distorted until the surface tension is no

longer able to hold the droplet cohesion. When this happens, secondary droplets will appear, by minimizing the surface energy. The surface energy is given by:

$$S_\sigma = 4\pi\sigma r^2 \tag{2.81}$$

where σ is the surface tension in J/m^2 or N/m.

To characterize the balance between inertia forces that tends to break-up the droplet, and the surface tension that holds the droplet coherence, the Weber number is generally used, often in various versions, along with the Ohnesorge number.

The Weber number used in breakup is given by:

$$\mathcal{W}e_{breakup} = \frac{\rho_p \left|v-u\right|^2 D}{\sigma} \tag{2.82}$$

where $|v-u|$ is the relative velocity between the particle and the surrounding flow and the diameter used is the one from the initial drop.

There is a critical Weber number under which no breakup event can occur. The critical Weber number correlation was given by Brodkey in 1969 for gas-liquid flows:

$$\mathcal{W}e_c = 12\left(1+1.077\mathcal{O}n^{1.6}\right) \tag{2.83}$$

where $\mathcal{O}n$ is the Ohnesorge number:

$$\mathcal{O}n = \frac{\mu_p}{\left(\rho_p D\sigma\right)^{0.5}} \tag{2.84}$$

with μ_p the dynamic viscosity of the drop, D the initial drop diameter, ρ_p the drop density and σ the surface tension.

Pilch & Erdman (1987) described the following breakup modes, and gave correlations in the form of total breakup time versus Weber number for each one.

- Vibrational breakup $(\mathcal{W}e \lesssim 12)$
- Bag breakup $(12 \lesssim \mathcal{W}e \lesssim 50)$
- Sheet stripping $(100 \lesssim \mathcal{W}e \lesssim 350)$
- Wave crest stripping $(350 \lesssim \mathcal{W}e)$
- Catastrophic breakup $(350 \lesssim \mathcal{W}e)$

Most authors consider two breakup regimes: the primary breakup and the secondary breakup. This approach generally refers to liquid jet atomization: the primary breakup corresponds to the formation of large drops from the starting continuous liquid jet or sheet. The secondary breakup is the breaking from large-average-size drops into smaller droplets. This report will mainly focus on the secondary breakup. For acceleration or shear-induced break-up (does not applies to a jet or film breakup) the primary break-up time refers to the time the initial drop cease to exist in a coherent shape. The secondary breakup time is the time needed to generate the smallest drop size for the flow conditions.

The largest size of child droplets is estimated ultimately (at the end of the total breakup time) using the critical Weber number:

$$d = \mathcal{W}e_c \frac{\sigma}{\rho_p V^2} \tag{2.85}$$

There are several models of the breakup; here only the most commonly used ones will be briefly exposed:

- The Taylor Analogy Breakup model (TAB)
  This model was developed by Taylor[3] and is based on a force balance model similar to a forced damped spring-mass system, where surface tension acts as the spring stiffness, the forcing term similar to the drag force and the damping force expressed by the viscous forces. Droplets are distorted under the actions of oscillations and when the oscillations' amplitude goes beyond a critical value based on the droplet's radius, the droplet simply breaks-up. To determine the size and therefore the number of child droplets, as suggested by O'Rourke[4], one uses an energy conservation relation by assuming that child droplets are not oscillating.
  However this approach is only valid for low We ($We < 100$); beyond that critical value, droplets are shattered by high-speed flows. And this model should not be used when the full break-up dynamic is needed. The TAB model is implemented in OpenFOAM.

- The WAVE model (or Reitz Model)
  This model, suitable for high pressure and velocity flows ($We \geq 100$), was originally developed for spray applications by Reitz[5]. It is based on the Kelvin-Helmholtz instabilities, which produces waves at the droplet's surface. By determining the fastest growing unstable wavelength, it is possible to evaluate the radius of child droplets. This method is implemented in OpenFOAM.

- The Pilch & Erdman Correlation
  This break up model is based on the work from Pilch & Erdman (1987), described at the beginning of this Section 2.3.4. This model is implemented in OpenFOAM.

All those models have their interval of validity, which explains why several models can coexist in the same simulation. Several modifications have been provided to the original OpenFOAM implementation, adapting it to the software created during this PhD.

[3] G. I. Taylor. *The Shape and Acceleration of a Drop in a High Speed Air Stream.* Technical report, In the Scientific Papers of G. I. Taylor, ed., G. K. Batchelor, 1963

[4] P. J. O'Rourke and A. A. Amsden. *The TAB Method for Numerical Calculation of Spray Droplet Breakup.* SAE Technical Paper 872089, SAE, 1987.

[5] R. D. Reitz. *Mechanisms of Atomization Processes in High-Pressure Vaporizing Sprays.* Atomization and Spray Technology, 3:309-337, 1987.

2.3.5 Deposition

General information covering the deposition of particles is provided in this section, regardless of the nature of the particle, as this theory applies well to droplets and solid particles, even if small variations can be found. Based on the formulae given in the previous section (Equation 2.27), particles transported by the flow may collide with a boundary wall. The deposition denotes here the fact that particles remain on the boundary after they reach a wall. The deposition can be characterized by the dimensionless velocity of deposition or by the mass rate of droplets that are assimilated in the film/pool. It is shown in Ueda (1981) that the mass rate of deposition is directly proportional to the particle concentration in the core flow. Figure 2.13 shows the dimensionless velocity of deposition, given as:

$$V_{dep+} = \frac{m_{dep}}{C \cdot U^*} \tag{2.86}$$

where m_{dep} is the mass deposited per seconds and C is the concentration of particles in the flow, versus the particle response time $\tau_p^+ = \tau_p . \left(\frac{U^{*2}}{\nu}\right)$. U^* is the friction velocity defined previously in Equation 2.9.

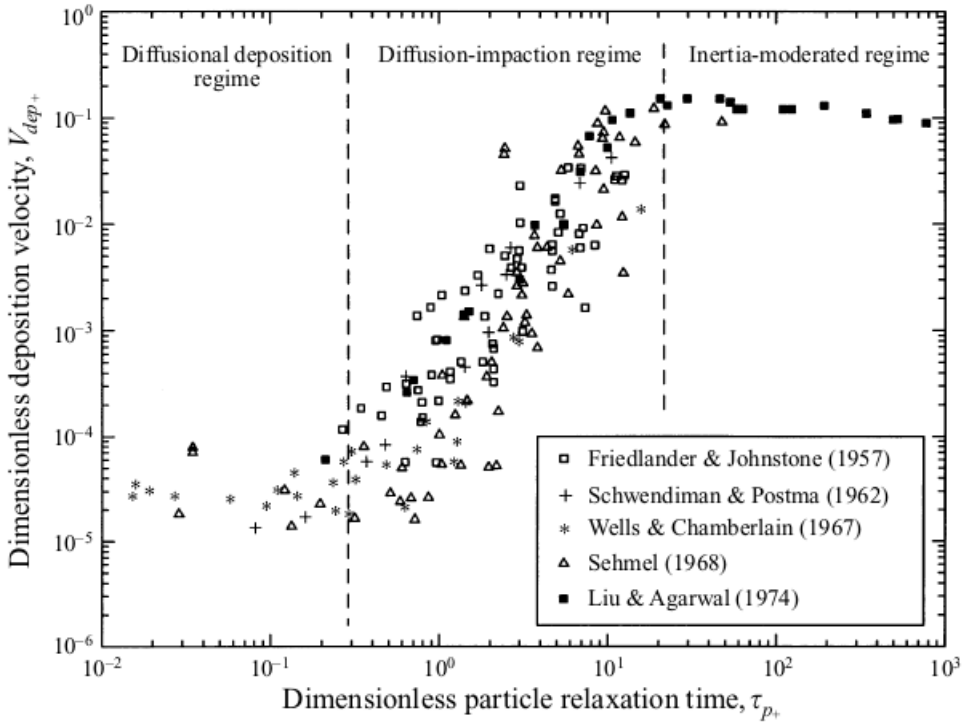

Figure 2.13: *Deposition curve in a turbulent pipe flow. Source: Young & Leeming (1997)*

Three regions can be observed in Figure 2.13:

- $\tau_p^+ < 0.3$ where particle deposition is dominated by the Brownian motion.
- $0.3 < \tau_p^+ < 20$ where turbulence plays a major role.
- $\tau_p^+ > 20$ where the particles motion is dominated by inertia.

In the first zone, particles are so small that their motion is almost fully determined by their own agitation. For that kind of particles, deposition is determined by the probability for droplets to reach a wall with such an agitation. As the agitation becomes more and more significant for particles of a molecular size, this probability increases.
For medium-size particles, drag forces are predominant and the fluid behaviour impacts particle trajectories. This regime is also said driven by the particle-turbulence interaction (or turbulence dispersion). A general description of the turbulent dispersion is provided in Section 2.3.1. For lower-middle-size particles, particles easily follow fluid variations in the core flow and in the buffer layer, where particles that were expected to touch the wall can suddenly be re-entrained. Therefore, the deposition rate is low.
The larger the particles, the greater their inertia becomes. The particle motion can no longer be evaluated without taking into account the crossing trajectories effect (see Wells & Stock (1983) for details). Gravity cannot be neglected in this case, as particles attempt to fall on a nearby wall.

2.3.6 Miscellaneous phenomena

Various phenomena related to droplets are worthwhile to mention and discuss. Most of them are generally neglected, as they are often difficult to model, not well known or simply too detailed compared to the previously exposed forces. Nevertheless, this sub-section introduces phenomena useful to model the full droplet cycle in a multi-phase environment. Many methods exist to model those various phenomena and several of them are briefly presented here, although not used in any simulation carried out during this PhD. This document does not pretend to be exhaustive by any means, and only a handful of phenomena, thought to be relevant in multi-phase flows, are introduced.

Particle shape

Throughout this thesis, all the particles tracked are supposed to have a perfectly spherical shape. This hypothesis is often reasonable, in particular when the drop diameter is less than a micrometer, or when using solid glass particles, frequently used experimentally. However, for both solid particles and droplets, such assumption does not always hold. The previous droplet break-up based section 2.3.4 has shown how the flow can deform the droplets, eventually leading to its break-up.

The particle shape affects the linear and rotational momentum equations, as well as the particle wall interactions.

Accounting for the particle shape

This paragraph briefly introduces the notations used to deal with non-spherical particles. The informations provided here are mainly extracted from the book by Crowe *et al.* (1998) and the same notations are being used here. Some of these notations were themselves introduced by earlier authors, like Waddel who

introduced the sphericity term for particle description in 1933. Since then, these notations have been used by many other authors, including Loth (2000).

Several parameters exist to account for the non-spherical state of a particle. The sphericity parameter is defined as:

$$\Psi = \frac{A_s}{A} \tag{2.87}$$

where A_s is the surface area of a sphere of the same volume and A the actual surface area. The Volume-equivalent-sphere diameter used in that case is:

$$D_n = \left(\frac{6V_d}{\pi}\right)^{1/3} \tag{2.88}$$

where V_d is the non-spherical particle volume. The surface-equivalent-sphere diameter is then expressed by:

$$D_A = \left(\frac{4A_p}{\pi}\right)^{1/2} \tag{2.89}$$

where A_p is the projected area of the particle in the direction of the relative velocity. It should be noted that the ratio:

$$d_{32} = \frac{D_n^3}{D_A^2} \tag{2.90}$$

is also known as the Sauter mean diameter (SMD). The particle circularity can be written as:

$$c = \pi D_A / P_p \tag{2.91}$$

where P_p is the projected perimeter of the particle in the direction of the relative motion. These parameters are used to correct the drag factor. The drag force is given by:

$$F_D = 3\pi\mu_c D_n f \Delta U \tag{2.92}$$

where f is the drag factor and ΔU is the relative velocity. Then, the modified drag factor for non-spherical particles is given by Tran-Cong (2004):

$$f = \frac{D_A}{D_n}\left[1 + \frac{0.15}{\sqrt{c}}\left(\frac{D_A}{D_n}Re_r\right)^{0.687}\right] + \frac{0.0175Re\left(\frac{D_A}{D_n}\right)^2}{\sqrt{c}\left[1 + 4.25\times10^4\left(\frac{D_A}{Dn}Re_r\right)^{-1.16}\right]} \tag{2.93}$$

where $Re_r = \frac{\rho_c D_n |u-v|}{\mu_c}$

Agglomeration and packings

When the local volume fraction of particles approaches the packing limit, particles begins to regroup themselves into various shapes. For mono-dispersed spherical particles, the packing density starts at 0.52, and the densest packing is can reach a packing density of 0.74.

In the conditions tested during this PhD, only dispersed flow were considered, so no packing was possible.

Turbulent bursts and sweeps effects on particles

Near-wall turbulent structures affect the behaviour of small Stokes number particles. In practice, close to walls the assumption of a Gaussian distribution of the fluctuations is wrong (Jin *et al.*, 2015). The Gaussian distribution is skewed (per components) to represent the occurrence of sudden burst of fluctuations pushing particles away from the wall and sweeps which tends to push particles towards the wall. This can modify the prediction of deposition, but it is difficult to evaluate their effects on the averaged deposition velocity.

Droplet-boundaries interaction

The impaction of droplets on dry or wet walls has been studied in details in Rein (1993). In the case of a wetted wall, a droplet may bounce, splash or merge with the film. Most of the time, a droplet hitting a wall is assumed to simply merge with the film.

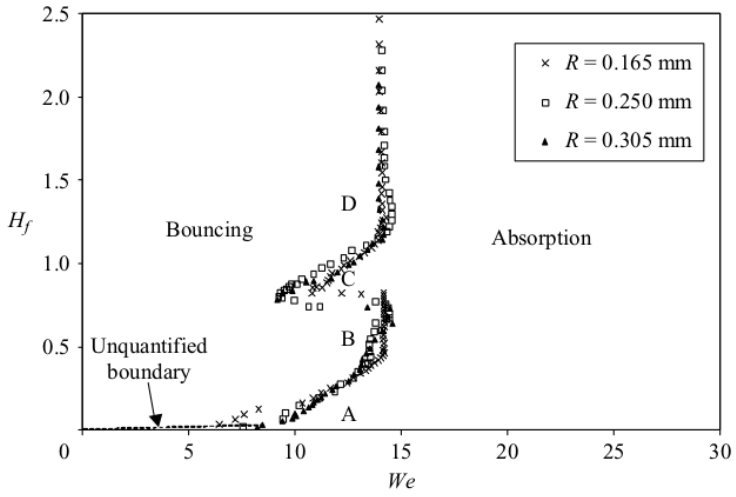

Figure 2.14: *Droplet-film interaction regime H-$\mathcal{W}e$*
Source: Pan & Law (2007)

The study of Pan & Law (2007), from which Figure2.14 is extracted, shows evidence that two main parameters control the droplet-film interaction: the Weber number and the film thickness. The Weber number is defined by:

$$\mathcal{W}e_{drop-film} = \frac{2\rho_l V^2 R}{\sigma} \tag{2.94}$$

where V is the impact velocity, ρ_l the density of liquid, σ the surface tension and R the droplet radius. Pan and Law define also the dimensionless parameter $H = \frac{\delta}{R}$. This is illustrated in Figure 2.14 for three droplets radii (165 μm, 250 μm and 305 μm). Two main regions are shown in this figure: the absorption region and the bouncing region. It appears that bouncing can only happen for Weber numbers lower than 15. Absorption may happen for Weber numbers below 15, for values of H around 0.8 and for values lower than 0.3. The impaction of droplets on dry

walls can lead to three major behaviours: bouncing, splashing and wetting. The wetting phenomenon is very briefly introduced in the following paragraph.

Wetting and drop spreading

The details of the droplet spreading are out of the scope of this thesis, although, some features of the code do include the droplet spreading to generate a pool. Here, only the basics of droplet wetting are discussed. For more information, consult the reviews from Bonn *et al.* (2009); Coninck *et al.* (2001); Haerth & Schubert (2012); Rein (1993); Yarin (2006); Zhang *et al.* (2008) for instance. The wettability is the characteristic of a substrate quantifying the easiness a liquid can spread over its surface. A frequently reported parameter qualifying this is the apparent contact angle θ_{123}, where the subscript "123" refers to the three medium involved ("1" being the substrate, "2" being the droplet and "3" the medium carrying the droplets and also in contact with the substrate. A contact angle of $\theta_{123} = 0°$ meaning the substrate is completely wet and a contact angle of $\theta_{123} = 180°$ meaning a completely non-wetting substrate. The surface roughness, the temperature, the chemical nature of both substrate and wetting liquid as well as the third medium affects the wettability of a substrate. Usually, contact angles are tabulated for a giving liquid-substrate combination (the third medium being often implicitly the air, frequently not reported).
Haerth & Schubert (2012) reports, for droplet large enough for the gravity to affect the spreading, the droplet radius evolution in time as:

$$R_{spread}(t) \propto \mathscr{V}^{3/8} \left(\frac{\rho g}{\eta} t \right)^{1/8} \tag{2.95}$$

where $\mathscr{V}$ is the droplet volume, g the gravitational acceleration. Coninck *et al.* (2001) shows that different time scales influences the dynamic of droplet spreading on a surface. Zhang *et al.* (2008) published its study for inclined spreading.

2.4 Predicting the carrier flow

2.4.1 An example of turbulence modelling

The low-Reynolds $k-\varepsilon$, $k-\omega$ SST, $v2f$ and BL-v^2/k and RSM LRR (Launder-Reece-Rodi) RANS turbulence models have been used during this thesis. The low-Reynolds $k-\varepsilon$ is one of most common models, with the Launder-Sharma (Launder & Sharma, 1974) a variant known as the standard $k-\varepsilon$ model. This model is relatively inaccurate, especially in case of large pressure gradients but is numerically stable and fast, so is widely used for industrial applications. The Wilcox $k-\omega$ is a commonly used two-equation model where one equation solves the transport of the turbulent kinetic energy and the other one solves the specific dissipation. The Shear Stress Transport (SST) variant of the $k-\omega$ model developed by Menter (1994) switches automatically from a $k-\omega$ formulation near the walls to the $k-\varepsilon$ definition in the bulk flow.

The SST formulation combines: i) a k-ω formulation in the inner parts of the boundary layer which makes this model directly usable in the viscous sub-layer

and can therefore be used as a Low-Re turbulence model , and ii) a switch to a k-ε model in the bulk flow and therefore avoids sensitivity problems encountered by a k-ω formulation due to inlet turbulence properties (ANSYS, 2013a).

In addition to solve the k and ε transport equations, the $v2f$-based model solves two transport equations for $\overline{v^2}$ and f with $\overline{v^2}$ the streamline-normal component of the fluctuations and f an elliptic relaxation function to account for near-wall anisotropy effects. In this model, $k-\epsilon$ accounts for the isotropic turbulence and $\overline{v^2}/\varepsilon$ for the anisotropic contributions.

Low Reynolds versions of the Reynolds Stress model exist. However, the high Reynolds formulation is most widely encountered.

OpenFOAM (Weller & Tabor, 1998) for instance, only uses log-wall-functions which are inappropriate for refined walls. FLUENT (ANSYS, 2013a) proposes linear wall functions alongside log-wall-functions. The wall formulation is modified in FLUENT from the original formulation of Launder-Reece-Rodi (Launder *et al.*, 1975) to make it more robust, while OpenFOAM still uses the original formulation.

Wall functions are typically used to avoid sensitivities of the impact of wall mesh refinement on the computation time.

Large variations of the velocity and turbulent characteristic fields occur next to the wall. Numerical methods rely on interpolations between computed cell values. To correctly compute the near-wall fields, various strategies have been proposed. From Figure 2.15, it can be seen that the estimate of the wall-normal velocity gradient can change significantly, depending on the first cell approach and can produce wrong results if the size of the mesh is not carefully defined.

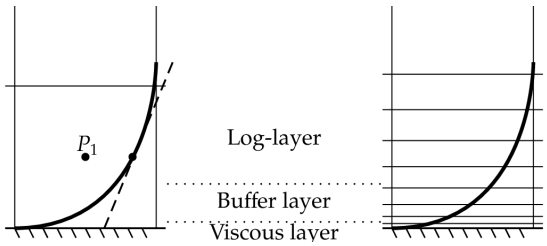

Figure 2.15: *High Reynolds number versus Low Reynolds number wall treatment*

It is important to mention that meshes which are too refined next to the walls often generate erroneous solutions, in particular when using the $k-\varepsilon$ formulation, where ε grows exponentially at the wall. It is generally recommended that the smallest cell height at the wall is such that $y^+ \simeq 1$. To generate such a mesh, the wall friction u^* has to be determined. Two methods are commonly used. The friction velocity scale-based estimation which is the simplest and fastest one, is based on the near wall gradient, pressure drop, and for the pre-processing part, on correlations (Blasius (1913) for instance). The second approach is the two friction velocity scale estimation which tries to take into account turbulence effects (Code_Saturne, 2015). The first method is more appropriate for a resolved wall mesh while the latter is best for a wall function-based mesh. Wall resolved meshes also increase the computational cost and can sometimes add instabilities.

The commercial ICEM-CFD (ANSYS, 2013b) and the open source SALOME (Salome, 2015) software were used to generate the meshes. Meshes requiring a first cell height of $y^+ = 1$ were constructed based on the friction velocity obtained from the Blasius correlation. Simulated results often showed discrepancies when compared to the Blasius estimates and the first cell height was usually found slightly below or higher than $y^+ = 1$. Other meshes using wall functions were generated with a first cell centre height around $y^+ = 20$, which is the recommended value when using such approach. Since different meshes were built, they did not always share the same quality, particularly for the non-orthogonality of the cells. However, all flow solutions were obtained with necessary correctors: extended cell least squares for Code_Saturne, standard non-orthogonal correctors for OpenFOAM and least squares for FLUENT. All the data provided in this thesis are non-dimensionalised using the friction velocity from the simulation.

2.5 Predicting the particle behaviour

2.5.1 Injection

In Lagrangian point particle simulations, the first point to carefully handle is the injection. Indeed, it has been shown (Graham & James, 1996) that the injection is important for both transient and steady state solutions, as it influences the long-term dispersion coefficient. Moreover, the flow conditions are generally not uniform throughout the simulation domain. So the fist particle position may place the droplet in a singular place, which could well determine the whole particle behaviour. Thus it is recommended to inject particles in a random position of the inlet section (instead of providing a pattern of injectors). These positions should be randomized in space and in time. Depending on the inlet section, the random positions ought to follow some rules:

- do not inject particles too close to the wall; let at least a distance that free fall particle would travel during two particle characteristic time be the minimum boundary injection distance.
- compensate for geometric effects; in case of a disk injection area, remember that the surface grows with the square of the radius: to hold a constant particle per square meters, one must inject more particles the farther from the disk centre.
- injecting a steady-sate pattern: sometimes, a concentration field of particles is expected (preferential accumulation).
- make sure particles are injected with a velocity close to the local flow velocity. It is advised to also give the injected particle a velocity fluctuation and a random turbulent iteration time.
- to better simulate the particle flow continuity, particles should be injected not on a surface, but in the small volume swept by the inlet during a time-step.

The (expected) particle concentration is also of great importance to properly calibrate the injection. Primary because particle interactions vary in case of a dilute flow compared to a dense or packed flow. Secondly, because the injection should be done in such way that the particle motion converges towards the target concentration profile.

A frequent goal one wants to achieve is, similarly to an Eulerian simulation, to have a predetermined initial volume fraction of the species represented by the particles at an intake. Doing such thing in an Lagrangian framework is not as straightforward as it is for an Eulerian simulation. It requires to compute, for each cell of the inlet, the average droplet mass flux, which depends on the flow velocity in each cell, on the surface of injection, and on the density function of position per cell. The latter is uniform in a squared geometry (channel), but quadratic in a circular shape (pipe). Note that the constant volume fraction profile might not be the best inlet profile to initialize a flow with, as often particles migrates into preferential accumulation zones. In case of an LES or a DNS, these effects of accumulation are often even more present, but often have a more localized aspect (filaments).

The Lagrangian point particle approach can be unsuitable to simulate a very large number of particles. A better method could be to use parcels instead of single particles. The main difference compared to the point particle approach, is that each parcel carry the informations relative to many particles. With the parcel approach, the parcel will be tracked by the simulation as if there where only one particle (in term of mass, effective surface area, etc) but will be carrying the information of many, allowing to retrieve the necessary informations. This imposes a set of restrictions to all particles represented by the parcel:

- the parcel carries only particles of the same size
- the droplets are travelling in the vicinity of parcel centre
- no collisions, no break-up or coalescence inside a parcel (except in some special cases)
- the volume fraction in the cell where several parcels can be, should not exceed one

The parcel method was used throughout this work and more than 2.5 millions of parcels representing each thousands of actual droplets have been simulated in a single domain.

Collisions (and break-up, and other phenomena (de-volatilisation...) can still be handled by the parcel approach, but even more cautious care should be taken. The best approach to compute the collisions in that case, would be to evaluate the Eulerian concentrations and use the expressions available in Section 2.3.3.

Numerical procedure

One shot injection

The most simple way is to inject once a given number of particles. This type of injection is faster than injecting quasi-continuously particles, but does not

allow the same sort of studies, Results obtained with this method are generally less accurate. It is almost impossible to get particle concentration fields or mass flux data with this method, except through the use of very advanced processing strategies, extrapolating the missing information from the motion of a limited amount of particles.
This injection was used to validate the deposition and the particle motion solver, as well as to reproduce the results Matida *et al.* (2000). In theses simulations, 10,000 particles were injected in concentric layers over a disk area. Results are discussed in Chapter 3.

Quasi-continuous injection

The quasi-continuous injection consists in injecting a set of particle every time-step. It is called "quasi-continuous" as the discrete time stepping can not allow for an actual continuous injection. Instead, an approximation is done to inject at a next time step the cumulated particle number (or mass) that is supposed to have flown through between the previous time step and the current one. Hence, it can appear as if a given number of particles are being released at the same time. To resolve this problem, specific times associated with each individual parcel injected are given. It is thus possible to attribute a time between two time steps to a parcel. This is not sufficient to compensate the errors introduced by the discrete aspect of the simulation. The particle position, velocity and all other associated parameters should be modified at the start of a new time step.

This sort of injection allows for more data information to be retrieved and with more precision that with the single burst injection. It becomes possible, for instance, to measure mass fluxes.

This kind of injection has been used throughout cases performed in industrial pipes, since the input information was the weight-water content.

Entry effects

If the injection is not realistic enough, or simply because it takes some time and/or some distance to generate the expected particle dispersion profile, simulations can suffer from entry effects. These effects could affect the results of concentration prediction and deposition. These effects decrease farther away from the injection point. (Picano *et al.*, 2009) propose a criterion to evaluate the final dispersion state and also to characterize the preferential accumulation, when there is one. To characterize the preferential dispersion (Picano *et al.*, 2009) propose to divide the cross-section of a pipe into M equal-area annuli. Thus the criterion is based on the definition of the entropy:

$$S(z) = -\sum_{i=1}^{M} \frac{N_i(z)}{N(z)} ln\left(\frac{N_i(z)}{N(z)}\right) \tag{2.96}$$

where N_i is the mean particle number within the domain delimited by the annuli and a distance Δz.

When $S(z)$ is constant, the steady state of dispersion is reached.

Number conservative approach

When applying a number conservative approach, the mass flow rate of water to be injected ($\dot{m}_w$) and the volume water flow rate (Q_w) are considered:

$$\dot{m}_w = Q_t \times \rho \times wct \tag{2.97}$$

$$Q_w = \frac{\dot{m}_w}{\rho_w} \tag{2.98}$$

Table 2.2 provides the drop number ratio for the number conservative approach for the small distribution of droplets of sizes 9, 25 and 41 μm for a water cut of 0.25% by weight used in the industrial simulations performed. The results of these simulations are discussed in Section 3.4.

Table 2.2: *Drop number ratio for the number conservative approach*

Drop diameter [μm]	9	25	41
Drop number ratio	93.85 %	4.76 %	1.39 %

In application to Equation 2.101, $\mathscr{N} = 4.08 \times 10^9$ which leads to the distribution of droplets number per second written in Table 2.3.

Table 2.3: *Summary of number conservative approach*

Drop diameter [μm]	9	25	41
Drop number per second	3.83×10^9	1.94×10^8	5.67×10^7
Mass flux [$kg \cdot s^{-1}$]	1.462×10^{-3}	1.589×10^{-3}	2.047×10^{-3}
Volume flux [$m^3 \cdot s^{-1}$]	1.462×10^{-6}	1.589×10^{-6}	2.047×10^{-6}
Water volume ratio [%]	29.5 %	31.2 %	39.1 %
Number ratio to smallest number	67.5	3.4	1

These numbers of droplets per second are too high to be injected as such. Instead, a parcel approach is chosen, where each parcel consists in a group of physical droplets of same size. It is assumed that a parcel moves through computational cells in the flow field as the motion of an individual droplet.

For transient simulations, if a time step of $1 \times 10^{-4} s$ is considered, and if at least one parcel of the smallest droplet number is injected per second, the parcel number per second for each size can be determined. If the parcel injection is based on the mass flux (per size) and by parcel per number, OpenFOAM will adapt the number of particle per parcel to satisfy both conditions.

The resulting droplet distribution is uniformly injected at random positions (varying in time) from the inlet of the pipe section. This leads to an increase rate of deposition close to the inlet (entry effects), due to droplets injected too close from the walls. However, these entry effects are minor and they do not affect significantly the disperse flow.

This volume flow rate can be decomposed as a sum of volume fluxes associated with each particle sizes:

$$Q_w = Q_{9\mu m} + Q_{25\mu m} + Q_{41\mu m} \tag{2.99}$$

Each volume flux can be written as the product of the number of drops injected per second by the droplet volume:

$$Q_w = N_{9\mu m} \times \mathscr{V}_{9\mu m} + N_{25\mu m} \times \mathscr{V}_{25\mu m} + N_{41\mu m} \times \mathscr{V}_{41\mu m} \tag{2.100}$$

where $\mathscr{V}_{9\mu m}$ is the volume of one droplet of the considered size.
By introducing the number ratio of each drop size:

$$Q_w = \mathscr{N} \left(p_{9\mu m} \times \mathscr{V}_{9\mu m} + p_{25\mu m} \times \mathscr{V}_{25\mu m} + p_{41\mu m} \times \mathscr{V}_{41\mu m} \right) \tag{2.101}$$

where $\mathscr{N} \times p_{9\mu m} = N_{9\mu m}$ (idem for all sizes) where $p_{9\mu m}$ is the number fraction for the considered drop size. Equation 2.101 has only one unknown and is easily solved to find $\mathscr{N}$. A numerical application of this method can be found in Section 3.4.

Chapter 3

Results of studies

A five meter long vertical pipe of diameter 0.5 in. has been selected to validate the deposition model against the experimental results of Liu & Agarwal (1974) and the simulation carried out by Matida *et al.* (2000). The Reynolds number is $Re = 12,970$ and the pipe wall is assumed smooth. Simulations have been performed with the flow conditions described in Table 3.1.

Table 3.1: *Flow conditions for air*

U_G (m/s)	ρ_f (kg/m^3)	μ_f (m^2/s)	Re $(-)$
15.66	1.2	$1.84\ 10^{-5}$	$12,970$

More details of the flow are given later in Section 3.3.1 as part of the pipe flow scaling-up study. Results of the Lagrangian droplet simulation are presented below.

3.1 Dispersed flow results

Ten thousand mono-dispersed droplets have been released from the centre of the inlet section of a vertical pipe with the flow going downwards. This injection has been repeated for each particle size considered. This number of particles injected reduces the computational cost of the Lagrangian simulation, without impacting much the averaged deposition velocity (Lai & Cheng, 2007). For the sake of clarity and to limit extensive post-processing, only results from three representative drop sizes are discussed in the following section. The particle-wall interaction is set to stick: once the distance between the particle centre and the wall is equal to the particle radius, the particle velocity is set permanently to zero. Furthermore, there is no re-injection of parcels once a particle deposits. Due to the low number of parcels and because particles do not bounce on the walls, the number of parcels decreases with the distance to the injection point. Injecting such a low number of particles (10,000) in the domain has been motivated by three major points. First, this allows a direct comparison with the work of Matida *et al.* (2000), who used

the same number of particles. Secondly, it appeared interesting to establish the minimum number of parcels to inject from the centre of the inlet section (farthest distance to the walls) to obtain reliable results (or when the deposition velocity becomes independent of the number of parcels injected). Finally, based on the number of parcels injected and their initial location, the resulting concentration field could be analysed.

3.1.1 Cross-section droplet statistics

The dispersion is a measure of the droplet cloud spreading in the pipe, but could also be seen as the evolution of the droplet cloud position moments in time and space. Being able to describe the droplet dispersion renders the prediction of the droplet concentration field possible and therefore the droplet deposition. Mechanisms primarily important in the droplet isothermal dispersion are the Brownian motion, the turbulent dispersion and the convective transport. There are several ways to describe dispersion, either spatial, temporal or based on a spectral analysis. The spatial and temporal evolutions of the dispersion are discussed here.

The positions of the droplets of size $0.5\ \mu m$ and $7.8\ \mu m$ and their associated radial distribution have been evaluated at various axial sections of the pipe. The objective was to establish a general way of describing the shape of the transient and steady state dispersion patterns for a large range of droplet sizes. It is important to find a universal radial distribution shape, which would be valid to describe the whole evolution of the dispersion. The evolution of the first three statistical moments are reported in the next section. Note that if the general expression of the radial distribution is known and is combined with the reported moment variations, the droplet concentration field (and resulting deposition) can be determined at every point in space and time.

The probability for a droplet to be in a radial interval is a random variable. It can be deduced by counting drops in bins, distributed along the pipe radius.

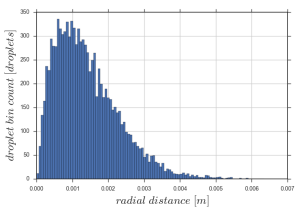

(a) $0.5\mu m$ near 0.01s dispersion $x = 0.14\ m$

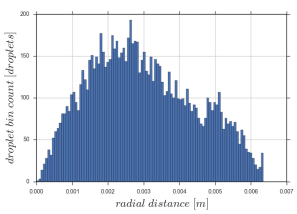

(b) $0.5\mu m$ near 0.1s dispersion $x = 1.008\ m$

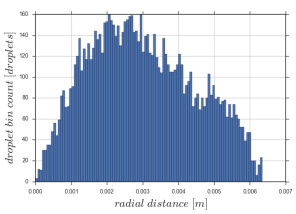

(c) $0.5\mu m$ near 0.2s dispersion $x = 2.54\ m$

Figure 3.1: *Spatial evolution of the radial dispersion - $0.5\ \mu m$ droplets*

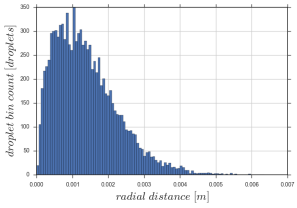

(a) $7.8\mu m$ near 0.01s dispersion $x = 0.14\ m$

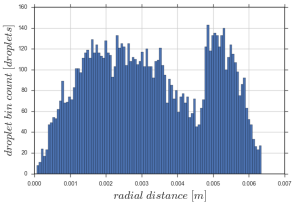

(b) $7.8\mu m$ near 0.1s dispersion $x = 1.008\ m$

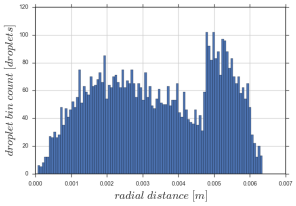

(c) $7.8\mu m$ near 0.2s dispersion $x = 2.54\ m$

Figure 3.2: *Spatial evolution of the radial dispersion -* $7.8\ \mu m$ *droplets*

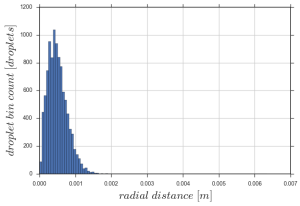

(a) $68.5\mu m$ near 0.01s dispersion $x = 0.14\ m$

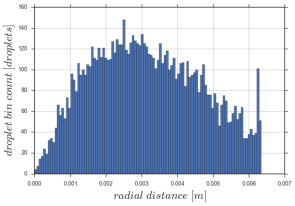

(b) $68.5\mu m$ near 0.1s dispersion $x = 1.008\ m$

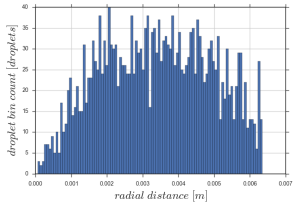

(c) $68.5\mu m$ near 0.2s dispersion $x = 2.54\ m$

Figure 3.3: *Spatial evolution of the radial dispersion -* $68.5\ \mu m$ *droplets*

Histograms displayed in Figures 3.1 to 3.3 were produced by generating a $0.0255\ m$ wide clip of the droplet pathlines and filtering them to keep one point only per droplet. All early dispersion profiles in these figures are similar, even though they do not necessarily develop at the same speed. After some time in the dispersion process, the radial distribution begins to be dependent on the droplet size.

Three zones are visible when the equilibrium state is reached: i.) a common dispersion shape, up to $0.005\ m$, ii.) a drop size dependent shape between $0.005\ m$ and $0.006\ m$ and iii.) a wall droplet build-up, common to all droplet sizes, but with various amplitudes. These regions seem consistent with the 3 layers described by Equation 2.50.

No satisfactory universal distribution has been found yet to represent at once all those states. A more detailed study should be devoted to that purpose only. A linear combination of several distributions will allow a finer and complete description of the previously described evolutions. However, such approach has not been investigated here.

The polar representation of the droplets positions illustrates how a radial distribution is represented in a disk area. Since 10,000 drops only are injected in the domain and since they stick to the wall when they reach it, too few of the $68.5\ \mu m$ drops are present near the outlet section of the pipe (most of them deposit between 1 and 2 m), rendering the analysis very difficult for droplets of this size. However, the analysis has been performed for the medium and small drop sizes considered here. Figure 3.4 shows the resulting polar representation from

a profile similar to Figure 3.1(c) for the $0.5\ \mu m$ droplets. The associated droplet surface concentration is represented by an histogram on Figure 3.5. Similar plots are obtained for the $7.8\ \mu m$ droplets, see Figures 3.6 and 3.7.

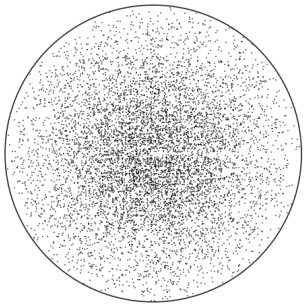

Figure 3.4: *0.5 microns droplets positions at the pipe outlet section*

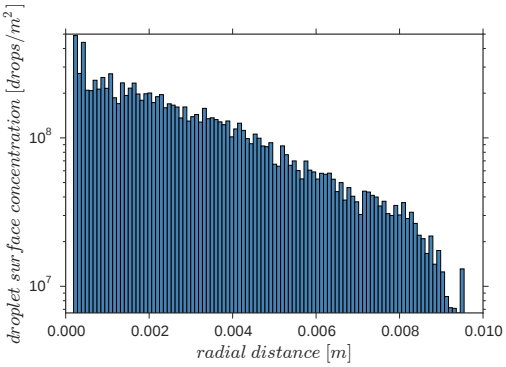

Figure 3.5: *Radial surface concentration: 0.5 microns*

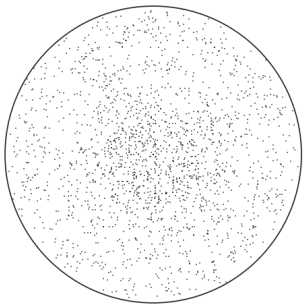

Figure 3.6: *7.8 microns droplets positions at the pipe outlet section*

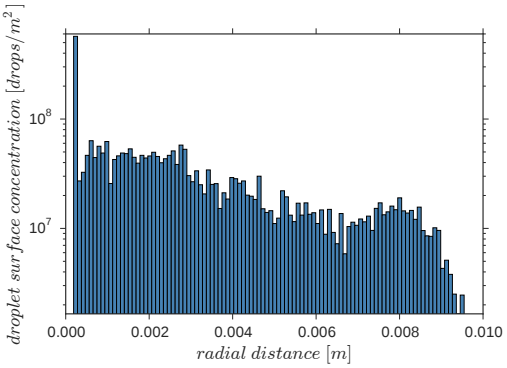

Figure 3.7: *Radial surface concentration: 7.8 microns*

The histograms on Figures 3.5 and 3.7 represent 100 pipe angular sectors of identical width (annuli areas). Sectors close to the centre of the pipe therefore have a smaller cross-sectional area than sectors next to the walls. Each vertical bar represents the number of droplets collected in each annuli sector divided by the annuli surface. The polar representation is achieved through clipping the droplets pathlines data one centimetre far from the outlet section and projecting the mean position of each droplet pathline onto a 2D surface.

In all cases, droplets are mainly concentrated around the centre axis of the pipe, the concentration decreasing as the annuli area increases from the pipe center to the wall.

3.1.2 Droplet dispersion

The previous section has described the general aspect of the cloud dispersion, particularly in its equilibrium state. Measuring the spatial and temporal evolutions of the radial dispersion moments leads to an estimate of the cloud dispersion.

The time evolution of the moments (mean radial position of the drops for a given time), the variance (axial) and the skewness are provided in Figures 3.8, 3.9 and 3.12. The continuous lines displayed on these figures represent the exponential fit curves for the data obtained numerically. A similar general behaviour can be seen in all plots: a starting transient phase followed by a relatively flat profile. The spatial evolutions shown in Figures 3.10, 3.11 and 3.13 display a straight pattern, less noisy than the time profiles. It can be seen that the droplet dispersion needs some time and some distance to reach an equilibrium state characterized here by the moments being constant. For the drop sizes investigated, a time of 0.2s and a distance of about 3m are necessary to get a fully established droplet dispersion. As expected, the dispersion of the largest droplets require more time to reach an equilibrium state. Near the end of each time profile, the data oscillate highly. Such variation is not clearly visible in the spatial distributions. This final de-coherence can be explained by the lack of particles near the end of the simulation, making any statistical analysis unreliable at the end of each simulation.

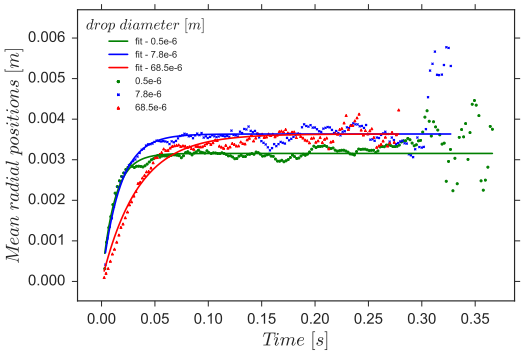

Figure 3.8: *Time evolution of the mean radial position of droplets*

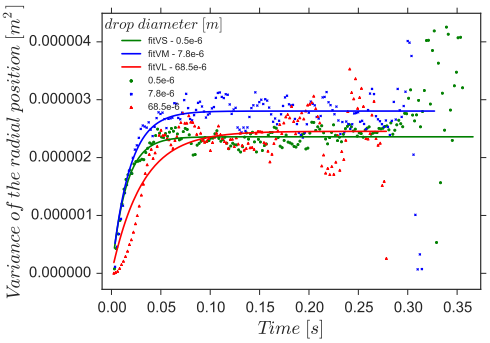

Figure 3.9: *Time evolution of the variance of the radial position of droplets*

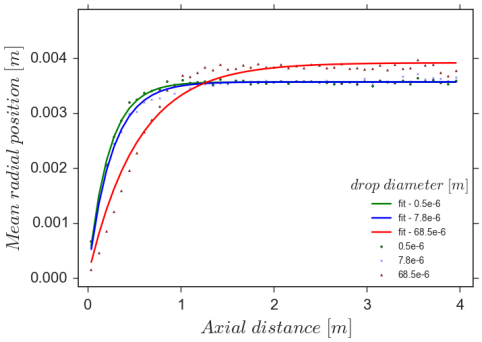

Figure 3.10: *Spacial evolution of the mean of the radial positions*

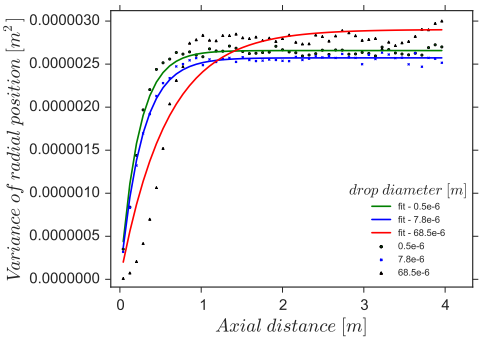

Figure 3.11: *Spacial evolution of the variance of the radial positions*

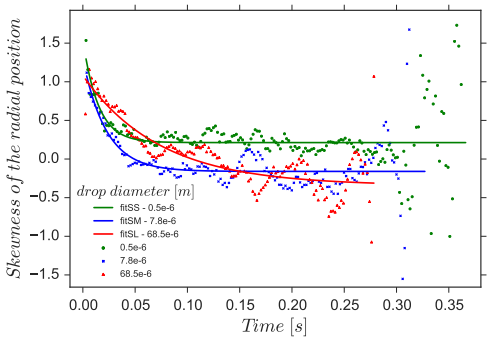

Figure 3.12: *Time evolution of the skewness of the radial positions*

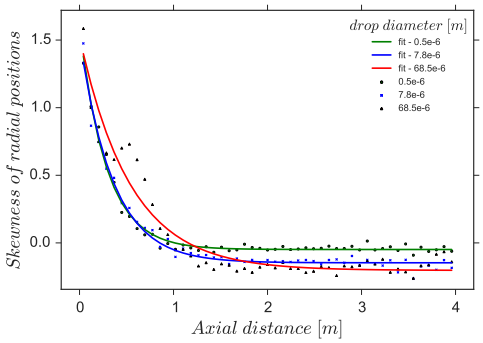

Figure 3.13: *Spacial evolution of the skewness of the radial positions*

To match the data plotted from Figure 3.8 to 3.13 and create a statistical model, exponential-based functions can be used; they are represented by plain lines on the figures. It is supposed that the variance and the mean variation follow an exponentially growing function $A\,(1 - exp(-t/\tau_A))$ while the skewness is assumed to follow a decreasing exponential $B\ exp(-t/\tau_B) + C$. Such exponential functions can be established, based on the overall shape of the evolution of the moments (variance, mean variation and skewness) which follow an exponential pattern. Furthermore, intuitively, an exponential law can generally be used in phenomena where an equilibrium value is asymptotically reached. The corresponding fitted values of A, B, τ_A, τ_B and C are written in Table 3.2.

Table 3.2: *Fitting function parameters A, B, τ_A, τ_B and C*

	Drop diameter $[\mu m]$								
Moments	0.5			7.8			68.5		
spatial mean	A	τ_A		A	τ_A		A	τ_A	
	0.0036	0.22		0.0036	0.257		0.0039	0.53	
spatial variance	A	τ_A		A	τ_A		A	τ_A	
	2.66×10^{-6}	0.23		2.57×10^{-6}	0.265		2.9×10^{-6}	0.57	
spatial skewness	B	τ_B	C	B	τ_B	C	B	τ_B	C
	1.65	0.29	−0.049	1.67	0.35	−0.15	1.73	0.54	−0.2
temporal mean	A	τ_A		A	τ_A		A	τ_A	
	0.0032	0.012		0.0036	0.017		0.0036	0.034	
temporal variance	A	τ_A		A	τ_A		A	τ_A	
	2.36×10^{-6}	0.015		2.8×10^{-6}	0.018		2.45×10^{-6}	0.03.1	
temporal skewness	B	τ_B	C	B	τ_B	C	B	τ_B	C
	1.33	0.015	0.21	1.46	0.022	−0.16	1.43	0.073	−0.34

Figure 3.14 shows the different existing states of dispersion and deposition for the injection. In Sector 0, the droplet cloud spreads quickly but does not reach the walls. Sector 1 depicts the region where the spreading has reached the walls, but is still not fully established. Droplets start depositing, but the rate of deposition has not yet reached its equilibrium state. Sector 2 represents the region where the dispersion is established and where a stable deposition velocity can be evaluated. Sector 3 may exist, depending on the flow settings. This region is present for the current simulations as all droplets are injected simultaneously and the flow conditions and droplet sizes allow such deposition. In this region, the droplet

concentration decreases since most droplets have already deposited. Finally, no deposition is present in Sector 4, which corresponds to a dry wall region. This can occur as either all droplets have already deposited in previous regions (no drops present either in the core flow), or the dispersion pattern is such that the near-wall concentration is low and/or the overall concentration is too low to be accounted for (only a few droplets deposit).

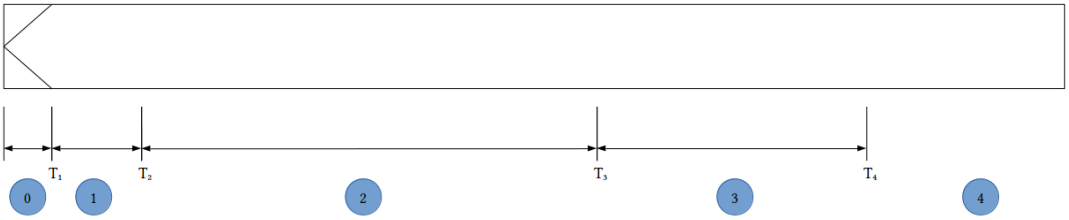

Figure 3.14: *Evolution of the dispersion/deposition scheme*

Picano *et al.* (2009) provided a relationship to evaluate the distance where the fully developed concentration profile in a pipe is reached:

$$\frac{L_\infty}{R} \simeq 75\tau_p^{+0.21} \quad . \tag{3.1}$$

When this formula is applied to the current cases, the fully developed droplet concentration is estimated to be reached at 0.2616m, 0.7723m and 1.92m for the droplets of sizes 0.5μm, 7.8μm and 68.5μm, respectively. These values do not seem to agree with curves shown previously on Figures 3.10, 3.11 and 3.13. A similar equilibrium-state concentration formula has however been determined, assuming that an equilibrium state pattern in the dispersion has been reached at the $3\tau_B$ position which corresponds to 95% of the asymptotic value reached:

$$\frac{L_\infty}{R} \simeq 157.388\tau_p^{+0.06453} \quad . \tag{3.2}$$

This correlation is different from Picano's one represented graphically on Figure 3.15. However, Equation 3.1 has been established using a continuous drop injection, which differs from the drop injection in this work, and for a Reynolds number of $3,000$, which is also different from the one used in this work ($Re \simeq 15,000$). Equation 3.2 provides fully developed concentrations obtained after 0.83m, 1.16m, and 1.54m, for droplets of sizes 0.5μm, 7.8μm and 68.5μm, respectively.

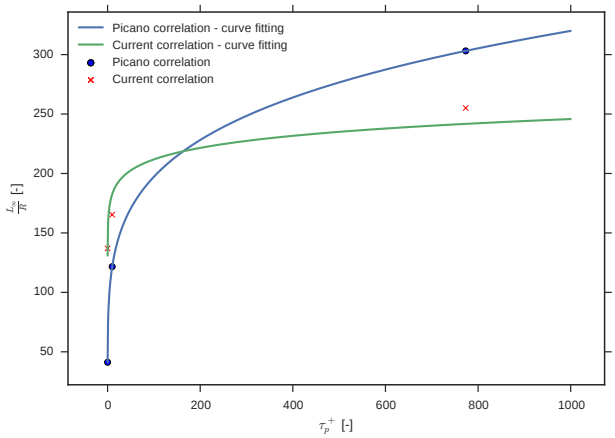

Figure 3.15: *Correlation comparison*

Deposition results and analysis

To analyse the droplets deposition, their position and the time required for them to deposit, the impact velocities have been investigated.

The cumulative density function (CDF) and probability density function (PDF) of deposition time (which can be compared to the first-passage time density function) allow to determine how rare the initial and “dry-out" deposition in the pipe can be (along with the deposition in the other sectors). Figure 3.16 shows the cumulated density function obtained for each drop size separately, in the 5m long pipe. This figure shows the four different sectors described previously through Figure 3.14. No deposition is present at the start of the simulation (Sector 0). After a laps of time, the deposition grows “exponentially" (Sector 1) to reach a region where the deposition rate is almost constant, i.e. where the slope of the curves is almost constant (Sector 2). The decrease of the number of drops decreases the deposition rate (curved region, Sector 3). Past this region, a plateau is present (more or less visible depending on the droplet size), which is due to the particles which have spent some time in the turbulent eddies or have been trapped in the boundary layer. The longer the plateau, the more sensitive a particle size to turbulence. Finally, the last region shows no deposition (Sector 4). The coloured lines present above Figure 3.16 represents the time limits of all sectors represented in Figure 3.14, where each colour corresponds to a particle size (colour displayed in the legend).

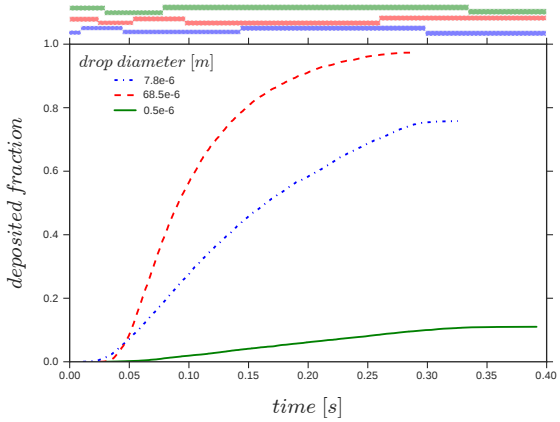

Figure 3.16: *CDF of time of deposition - deposited fraction along the time (0.5 ,7.8 and 68.5 microns)*

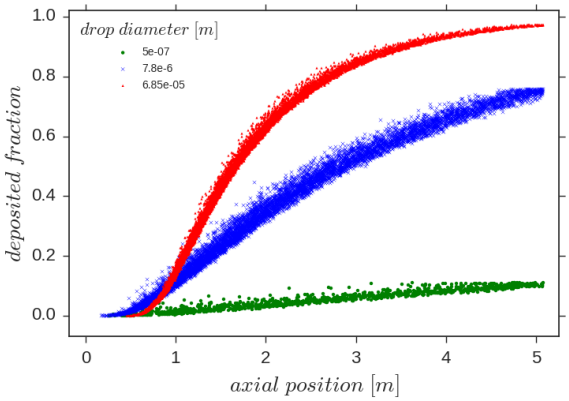

Figure 3.17: *CDF of axial position of deposition (current simulation)*

Figure 3.17 shows the ratio of deposited to the number of injected droplets against the axial position down the pipe. The curves follow a similar pattern as the time evolution of the same drop sizes in Figure 3.16. This result was expected since most drops are merely transported away by the flow. It can also be seen that for a given deposition fraction level, the deposition occurs over a certain spatial length.

The larger the drops, the faster the deposition. As shown on Figure 3.16, the time required for 90% of the drops to deposit is shorter for the large drops than for the small ones. Figure 3.17 shows that most large drops deposit between 1 and 2 meters.

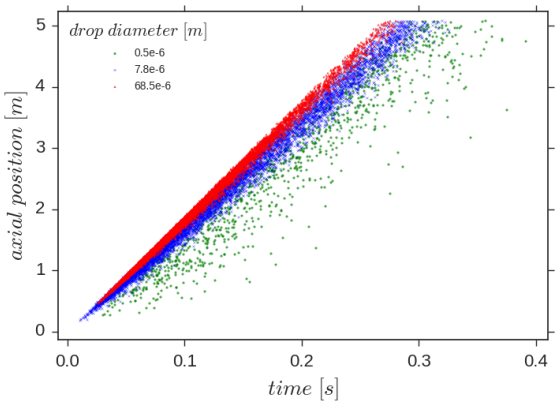

Figure 3.18: *Correlation between the impact position and the impact time*

A similar study has been performed for the spatial evolution. A strong correlation can be established between the time and the spatial evolutions of the variables, as shown in Figure 3.18. This correlation decreases with time and distance. The correlation, clearly visible for large drops which have a ballistic trajectory, is however less pronounced for small diffusive particles which are more likely to be affected by turbulence and Brownian motion effects. For each impact

position, there is a time interval represented by a lower and an upper bound during which all the deposition occurs. This interval varies with the droplet size and the time. Far away from the inlet of the pipe, the smallest droplets will take more time to deposit while the largest droplets will deposit quickly next to the inlet section of the pipe. This remark is also valid when looking at the space interval for each droplet size: the maximum distance between two deposited droplets is larger for small droplets than for large ones.

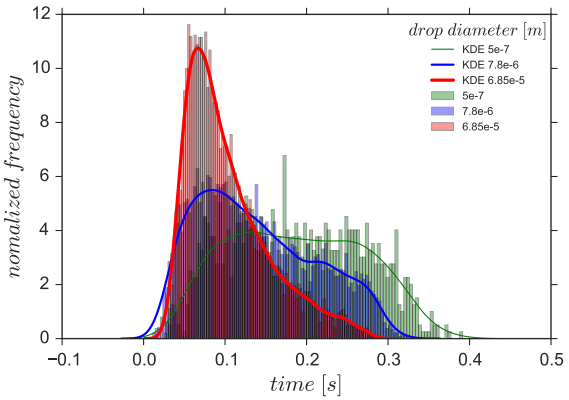

Figure 3.19: *PDF of deposition time and their respective Kernel Density Estimators*

Previous comments are further demonstrated through Figure 3.19 which shows the PDFs of deposition time and their respective Kernel Density Estimators. The larger the particle, the narrower the “time-bandwidth" (90% of the deposition occurs within a small period of time). The PDFs of the large and medium size drops seems to follow an inverse Gaussian shape. For the smallest drops, the PDF seems to be more evenly spread and over a larger time range.

Most of the large (68μm) drops deposit around 0.1s, i.e. the statistical mode is about 0.1s. The mode of the 7.8μm drops is less pronounced, but also seems to be around 0.1s. There is however no significant mode visible for the smallest drops, which seem to deposit with the same probability between 0.1s and 0.25s. It is well known (Atiya & M., 2005; Kou & Wang, 2003), that the “first passage time PDF" (i.e. the estimate of the probability density of time needed for a random process to cross a given level) for a jump-diffusion process with exponential jumps, is a generalized inverse Gaussian distribution. The Brownian motion with occasional turbulent jumps belongs to this family of processes; this is consistent with the PDF shown in Figure 3.19.

Figure 3.20 shows the axial variation of the radial component of the particles velocity during their impact on the wall surface. The large drops have a higher value as they act like inertial particles while the $7.8\ \mu m$ drops have a lower radial velocity. However, for the sub-micron particles, the radial velocity component can be as high as for the $68.5\ \mu m$ droplets and as small as for the $7.8\ \mu m$ ones. This means that the Brownian motion plays a major role here. It can also noticed that several values are outside the “main" lines: this is probably caused by drops influenced by turbulence (from higher fluid layers) which have kept their burst

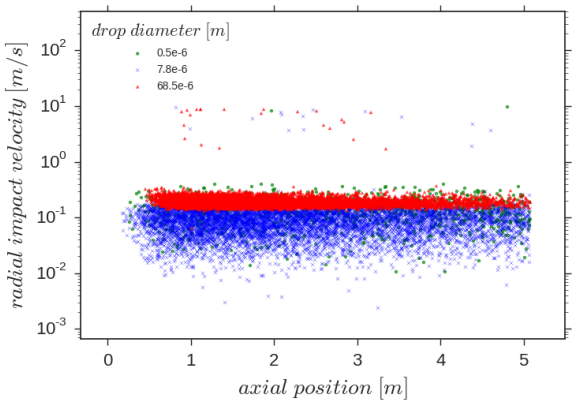

Figure 3.20: *Radial component of the impact droplet velocity versus the axial position*

velocity until they reach the walls.

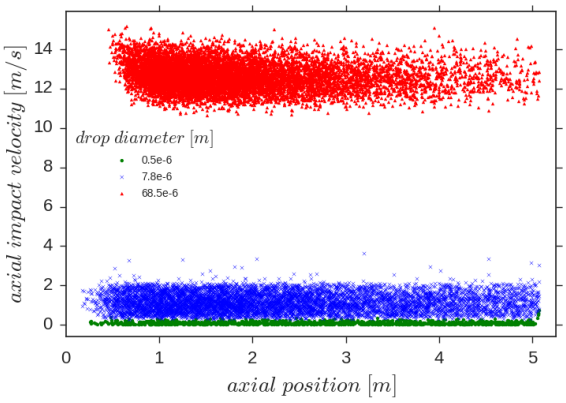

Figure 3.21: *Axial component of the impact droplet velocity versus the axial position*

Each droplet size has a distinct and restricted possible range of impact axial velocity components, see Figure 3.21. This velocity does not significantly change with the axial position. Note that the number of impacts decreases as drops reach the outlet section of the pipe. As stated previously, fewer droplets deposit in this region. The larger the droplets, the higher their axial impact velocity. This could again be explained by the fact that large drops acquire speed from the highest fluid layers and keep their velocity longer. On the contrary, smaller droplets adjust more easily their speed to the surrounding fluid velocity. The magnitude of the axial impact velocity is quite low for the sub-micron droplets and of the same order of magnitude as the radial impact velocity.

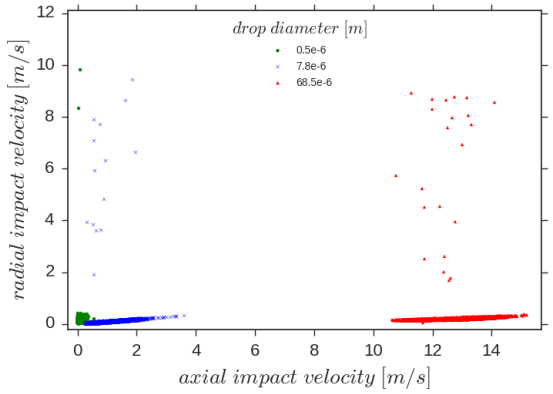

Figure 3.22: *Radial impact velocity versus axial impact velocity*

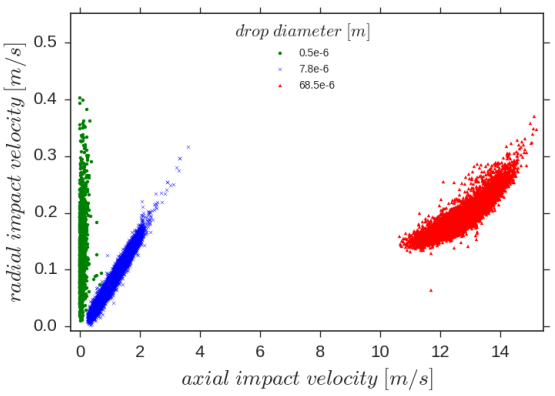

Figure 3.23: *Detail view of Figure 3.22*

Figures 3.22 and 3.23 provide additional information on the impact velocity. Both axial and radial velocity components are small and of the same order for the sub-micron droplets. However, it appears that such droplets are more likely to reach the wall with a velocity almost perpendicular to the wall (visible in Figure 3.23, where most of the points are located on the upper part of the line $radial\ velocity = axial\ velocity$). This would suggest that for sub-micron droplets, the main contribution to deposition is not only due to the cloud advance, but also to forces acting in the radial direction (Brownian motion and turbophoresis).

For the $7.8\ \mu m$ droplets, the magnitude of the impact velocity is higher than for sub micron droplets. The impact velocities are almost all aligned along a line of equation $y = 0.0878x - 0.015$, where x is the axial impact velocity (up to 4) and y represents the radial impact velocity. This equation is valid for all droplets except for those depositing because of a turbulent event. In this case, the radial component becomes higher than the axial component (off line points on Figure 3.22). Droplets affected by turbulence should impact the walls with a higher velocity. Such droplets should remain unaffected by the boundary layer, they are therefore not aligned. Slower drops which have spent some time in the near-wall boundary layer are more likely to be aligned (Picano *et al.*, 2009).

For the $68.5\ \mu m$ droplets, the impact velocities seem to follow an exponential profile. Several droplets are affected by turbulence, and consequently do not follow the exponential curve. However, in contrast to the $7.8\ \mu m$ droplets, turbulent impacts cannot make the radial component higher than the axial component.

Overall, it appears here that the near wall concentration is more highly dependent on the cloud axial advance rather than its radial dispersion, thus resulting in impact angles on the wall lower than 45°. In addition, the time scale of the radial dispersion is much slower (up to 100 times) than the axial convection. This means that once a set of particles has reached a given axial position, some time is required for particles at that axial position to reach the walls and reach their equilibrium state.

Transient study of moving cloud of particles

This section details characteristic parameters of a cloud of droplets in the 12.7 mm pipe, and to correlate it to the subsequent deposition. The following example describes a modified stochastic dispersion with OpenFOAM v.3, Matida's geometry and droplets (olive oil) diameters $d_p = 7.8\ \mu m$. The modifications consist in giving an initial random time of turbulent interaction and imposing an eddy lifetime in the domain dependent on y^+, to follow the near-wall behaviour from Lecrivain & Hampel (2012).

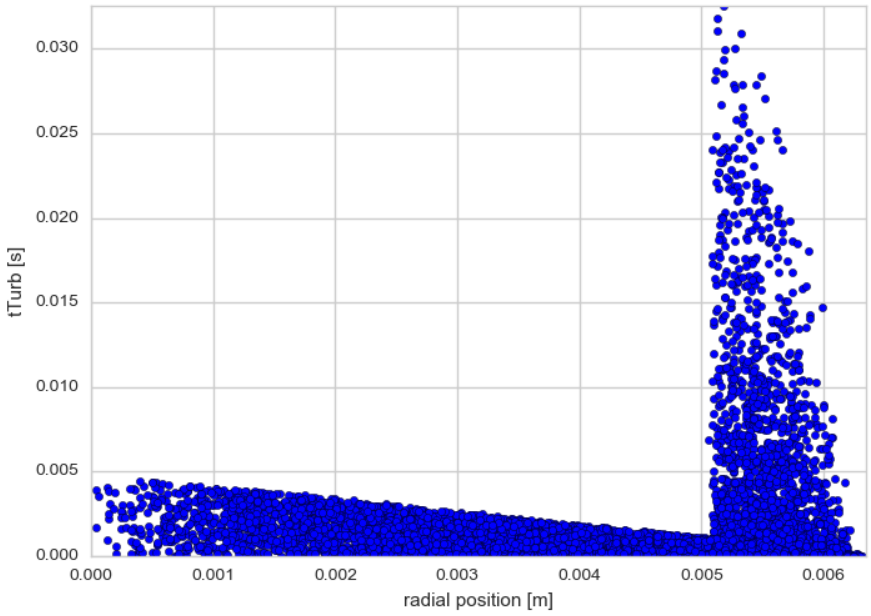

Figure 3.24: *Radial dimensional variation of the tTurb (moving part only)*

Figure 3.24 is the representation of the particle-turbulence interaction time (noted here $tTurb$) after 0.051s of simulation. For particles located at a radial position below 0.005 (in the core flow region), the $tTurb_{max}$ is a decreasing function of the radial position, with a maximum value at the centreline at about 0.005 seconds. For particles close to the wall, the $tTurb_{max}$ is much higher than for particles farther from the wall as it reaches about 0.032 seconds. The profile of $tTurb_{max}$ for that region is peak having its maximum value at a radial position of 0.005 meters and going to zero at the wall. This is likely due to an implementation error caused by the use of the turbulent dispersion instead of the laminar dispersion at the wall.

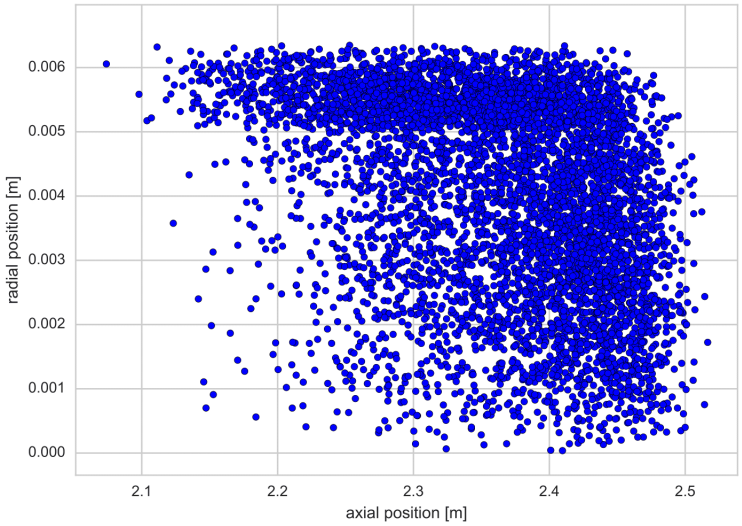

Figure 3.25: *Radial positions of the moving part along the main axis (at t=0.051 s)*

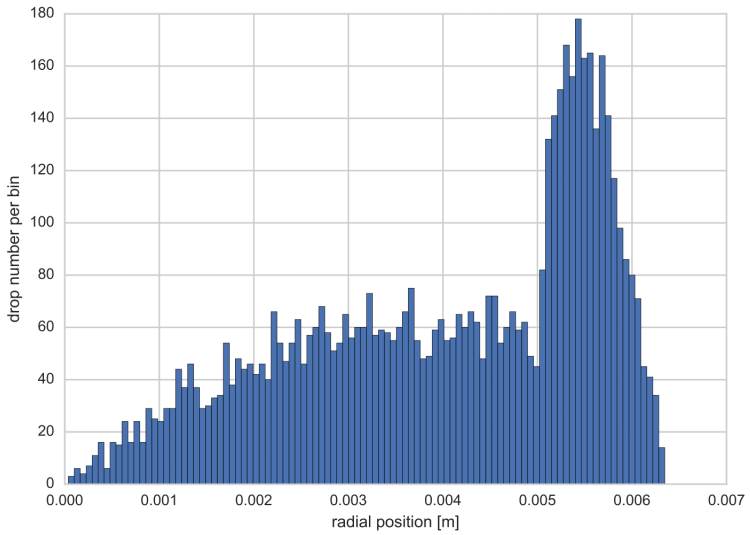

Figure 3.26: *Histogram of radial positions of the moving cloud (at t=0.051 s)*

The erroneous near-wall peak of $tTurb$ is correlated with a near wall peak of particle concentration, as it can be seen in Figures 3.25 and 3.26. Note that the carrier flow velocity is very slow near the walls and that particle velocities are less correlated for $y^+ < 40$, which is consistent with the turbulent kinetic energy profile.

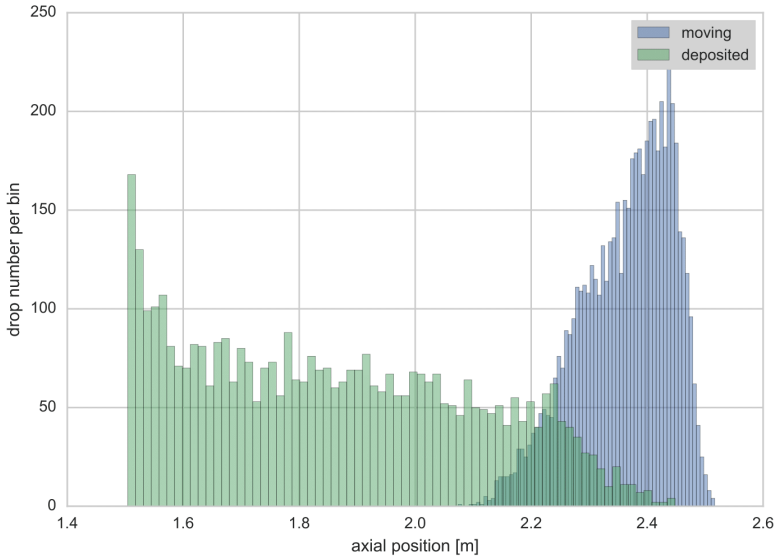

Figure 3.27: *Histogram of the axial parcel number a for both the moving and corresponding deposited part of the cloud (at t=0.051 s after the start of the simulation)*

Figure 3.27 shows the position of both deposited parcels and moving parcels. Notice the "position delay/gap" between the position of the passing cloud and the deposition, leaving deposited drops behind. The initial peak of deposition is due to entry effects.

The following describes the successive steps to evaluate the dimensionless deposition velocity k_p^+, even for a partial set of deposition data:

1. Plot the remaining fraction $F(x)$ as shown in Figure 3.28
2. Evaluate the least squares best fit function $F(x)$, called $\hat{F}(x)$ as in Figure 3.28
3. Using this function, retrieve the roots of the difference between $F(x) - \hat{F}(x)$ as in Figure 3.29. Note that it always exists two roots, as, at the beginning of the deposition, the entry effects enhance the deposition (as well as having the highest parcel concentration) and near the end, either because there are still moving parcels with depositing drops or because the drop concentration has declined.
4. The roots retrieved gives the region where the interpolation can reasonably be applied. One can refine a bit more the previous $\hat{F}(x)$ by finding the best interpolation between the roots, as in Figure 3.30.

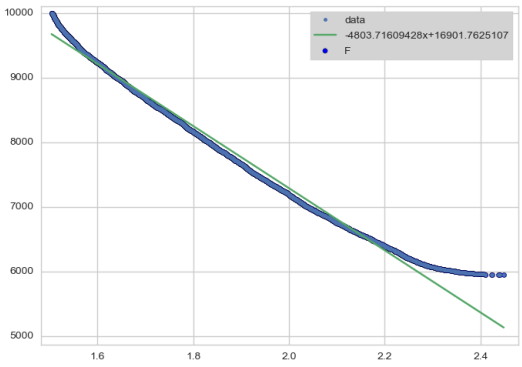

Figure 3.28: *Remaining fraction along the main axis (at t=0.051 s)*

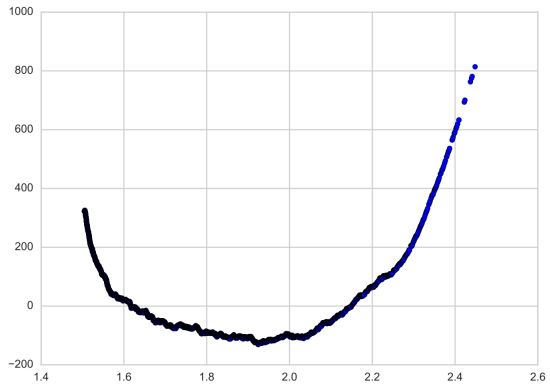

Figure 3.29: *Difference between the remaining fraction and the first interpolation (at t=0.051 s)*

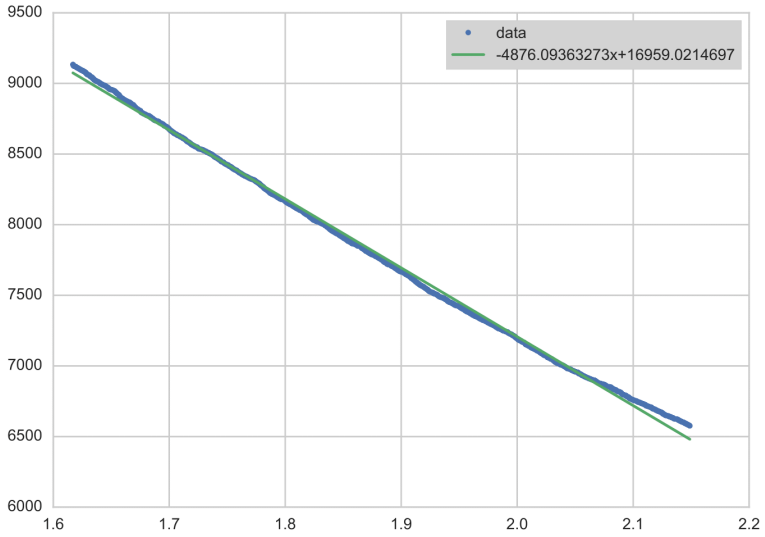

Figure 3.30: *Final remaining fraction curve fitting (at t=0.051 s)*

Equation 3.3 can be used to evaluate the deposition velocity.

3.1.3 Droplet deposition validation

Figure 3.31 summarizes the equilibrium state deposition results obtained with OpenFOAM. They are compared to numerical results from Li & Ahmadi (1993), He & Ahmadi (1999), Matida *et al.* (2000), Marchioli & Giusti (2003), to experimental data from Liu & Agarwal (1974) and to those reported by Papavergos & Hedley (1984). Additional numerical simulations have been performed with FLUENT (2014) for further comparison. The non-dimensional particle relaxation time $\tau_p^+ = \tau_p(u^{*2}/\nu)$ where u^* is the friction velocity and ν the kinematic viscosity, is plotted

in function of the non-dimensional deposition velocity k_p/u^*. The formula from Matida *et al.* (2000) has been used to calculate the deposition velocity:

$$k_p = \frac{\overline{u_f} d_t}{4\,(x_2 - x_1)} ln\left(\frac{F_1}{F_2}\right) \tag{3.3}$$

where F_1 and F_2 are the deposited fraction at two positions, d_t is the pipe diameter, $x_2 - x_1$ is the interval between the two axial positions.

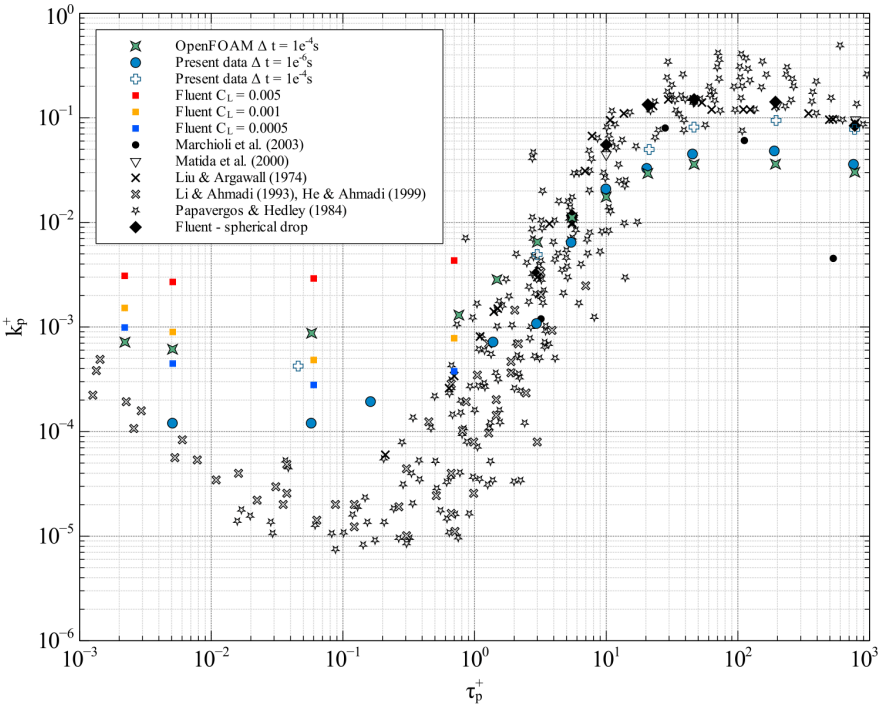

Figure 3.31: *Deposition velocity vs. relaxation time - Simulations and literature*

The time step sensitivity was tested with the present model, as shown by the Figure 3.31: the smaller the time step is, the closer the results are to the literature data. Two zones can be differentiated in Figure 3.31, when the non-dimensional particle relaxation time τ_p^+ is higher or lower than unity.

For the first region, when $\tau_p^+ \geq 1$, results are slightly under-predicted with OpenFOAM when compared to experiments although they are consistent with a DNS study from Marchioli & Giusti (2003). Those obtained with the commercial code FLUENT and those from Matida *et al.* (2000) are closer to the experimental data. However, in the contrary of OpenFOAM where the time scale constant remains constant for all droplet sizes ($C_L = 0.32$), this time scale constant has been determined specifically for each droplet size in FLUENT. According to the FLUENT manual, "C_L is to be determined and is not well known". However, guidelines are provided: $C_L = 0.15$ when applying the k-epsilon turbulence model and $C_L = 0.30$ for the Reynolds-stress turbulence model. Tian & Ahmadi (2007) specified that no universal value of C_L has been found yet, but typically, a value in the range 0.2 to 0.96 has been reported in the literature for producing satisfactory results for comparison with experimental data.

For the second region, when $\tau_p^+ < 1$, the influence of the Brownian motion is important. Results generated with OpenFOAM are closer to experiments than those obtained with FLUENT with low C_L values. FLUENT assumes that the turbulent integral time scale T_L is defined everywhere as $T_L = C_L \frac{k}{\varepsilon}$, and in particular next to the walls. Applying a small C_L value means that the near wall eddy-lifetime will be shortened, which complies with Equation 2.50.
Simulated results are higher than experimental and numerical evaluations reported in the literature, see He & Ahmadi (1999); Li & Ahmadi (1993); Papavergos & Hedley (1984); Tian & Ahmadi (2007) for instance. However, experimental measurements reported by Papavergos & Hedley (1984) and numerical solutions from the other authors were obtained in a vertical duct, while simulated results from OpenFOAM and FLUENT are obtained in a vertical pipe.

3.2 Particle concentration and deposition velocity

Although previous results of dispersion and deposition have been described separately, they are related. The particle concentration should be seen as an Eulerian field which is affected by the dispersion. Knowing the concentration field, its evolution and the turbulent field, the deposition can be predicted. This can be achieved with most Eulerian formulations by means of a diffusion-convection equation. An Eulerian drift-flux model such as the one reported by Lai & Cheng (2007) can be used to solve the evolution of concentration:

$$\frac{\partial C}{\partial t} + div\left[(u + V_s)\, C\right] = div\left[(D + \varepsilon_p)\, grad\,(C)\right] + Sources\ , \tag{3.4}$$

where C is the number of droplets per cubic meter, u the carrier fluid velocity, V_s the droplet settling velocity, D the coefficient of molecular dispersion, ε_p the particle turbulent dispersion coefficient. The deposition mass rate is a function of the particle concentration in the pipe, based on the following boundary condition:

$$J_w = \dot{m} = \rho_{p_w} V_{r_B} + p_t \rho_{p_T} V_{r_T} - \left[(D_B + D_{turb})\, \frac{\partial \rho_p}{\partial r}\right]_w\ , \tag{3.5}$$

with ρ_p the mass concentration of droplets, V the droplet velocity. Subscripts r and w denote radial and wall, respectively. Note that the new $p_t \rho_{p_T} V_{r_T}$ term accounts for the flux of drops coming from the nearest turbulent region to the wall. Drops can get high turbulent velocity from that region (around $y^+ = 20$ or 30, here) and impact the walls without loosing their speed significantly. The p_t parameter is present to account for the probability of such an event to occur since one part only of the drops present in that region, which have a positive radial velocity, are going to deposit. This term renders the expression slightly different from the wall flux derivation from Young & Leeming (1997). Finally, the $-D_{turb_w}\left(\frac{\partial \rho_p}{\partial r}\right)_w$ term accounts for the flux of drops depositing due to turbophoresis effects.
A possible novel statistical model is proposed, based on the following approach:

- Consider the initial droplet injection as a set of point particle sources.

- Evolve the dispersion of each point-source using the assumed distribution and the moments (provided in Table 3.2 in Section 3.1.2). Adapt the given evolution for points outside the inlet centre.
- Reconstruct the concentration field using the superposition of each radial distribution at a given time and position.
- Represent the wall concentration by the area of the probability density function exceeding the pipe radius $P(r > R)$.
- Evaluate the mass flux with Equation 3.5.

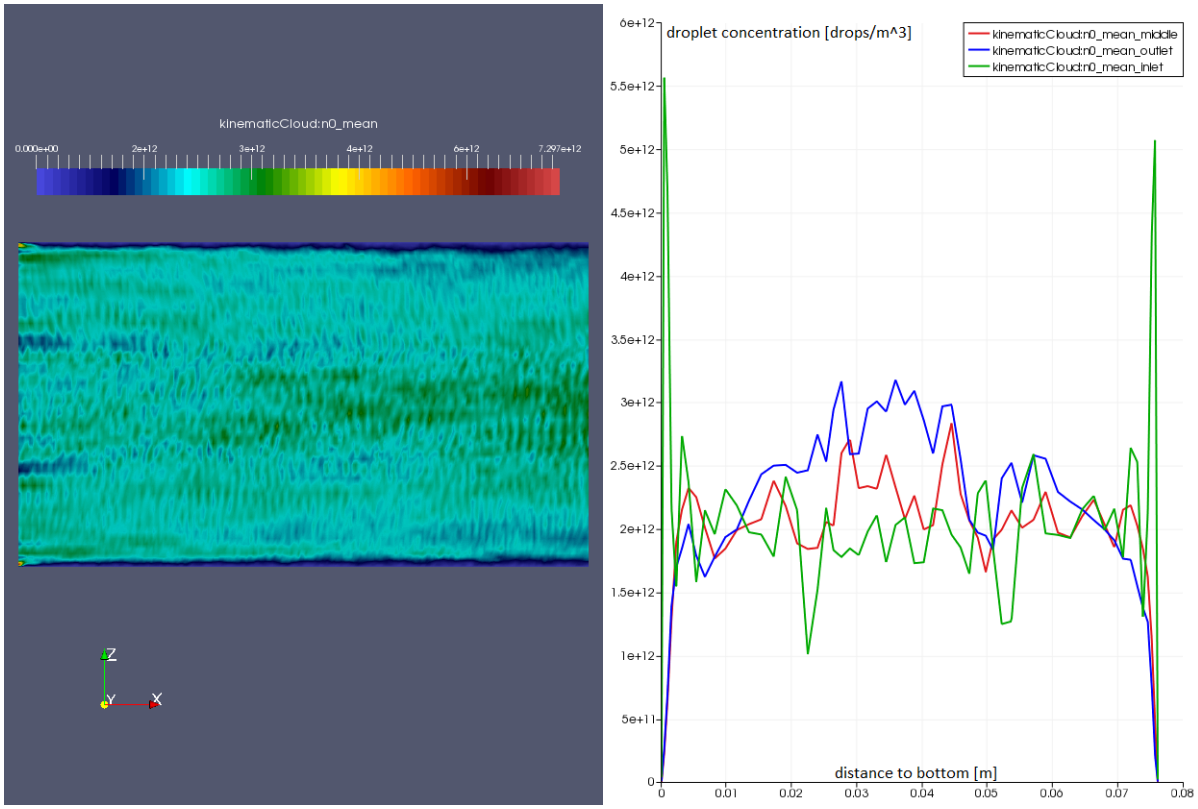

Figure 3.32: *Reconstruction of mean particle concentration over time from a Lagrangian field. Radial concentration profiles at three axial positions.*

Figure 3.32 shows an example of particle concentration generated using transient Lagrangian data in a 3 in. pipe for 9 μm droplets.

3.3 Straight pipe cases

3.3.1 Small diameter pipes

Experimental data are generally obtained in small diameter pipes. Such geometries are investigated first in this work as numerical results can easily be compared to available data from the literature.

0.5 in. ($\simeq$ 12.7mm) diameter pipe

As previously introduced at the start of Section 3, a five meter long vertical pipe of diameter 0.5 in. has been selected to validate the deposition model against the experimental results of Liu & Agarwal (1974) and the simulation carried out by Matida *et al.* (2000). The Reynolds number is $Re = 12,970$ and the pipe wall is assumed smooth. A mesh-independence study using OpenFOAM has been performed, as shown in Figure 3.33, and the flow solution obtained with the mesh comprising $760,500$ cells has been found suitable for further analysis.

Simulations have been performed with the flow conditions described in Table 3.3. Periodic boundary conditions have been applied at the inlet and outlet sections of the pipe to ensure that the flow is fully developed inside the whole domain. The SIMPLE algorithm was run until convergence, with a 10^{-6} convergence criterion.

Table 3.3: *Flow conditions for air*

U_G (m/s)	ρ_f (kg/m^3)	μ_f (m^2/s)	Re $(-)$
15.66	1.2	$1.84\ 10^{-5}$	$12,970$

The Blasius correlation can be used to evaluate the wall shear stress in smooth wall pipes:

$$\tau_w \approx f_f \cdot \rho_f \frac{U_{bulk}^2}{2} \ , \tag{3.6}$$

with

$$f_f = \frac{f_D}{4} = \begin{cases} \dfrac{16}{Re} & \text{if } Re < 3000 \quad (3.7a) \\ \dfrac{0.3164}{4} \cdot Re^{-1/4} & \text{if } Re > 3000 \quad (3.7b) \end{cases}$$

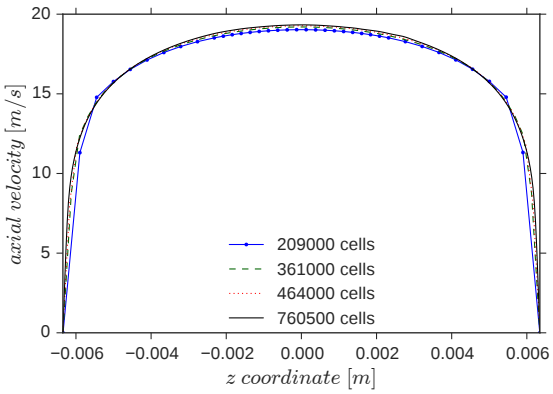

Figure 3.33: *Mesh independence study*

Although Direct Numerical Simulations (DNS) and Large Eddy Simulations (LES) are more accurate, they also require more time and computing resources compared to Reynolds Average Navier-Stokes (RANS) based simulations. Their use is therefore often limited to relatively low Reynolds numbers flows. The latter approach was therefore the preferred solution. Several turbulence models implemented in OpenFOAM and Code_Saturne were tested. The Launder-Sharma k-ε (Launder & Sharma, 1974) and the shear stress transport (SST) k-ω (Menter, 1993) models were both able to predict a pressure drop in agreement with the Blasius correlation for smooth walls (Equation 3.6), which predicts a wall shear stress around 1.08 Pa, and a pressure drop of 344 Pa/m. The expected friction velocity for this case is around 0.95 m/s.

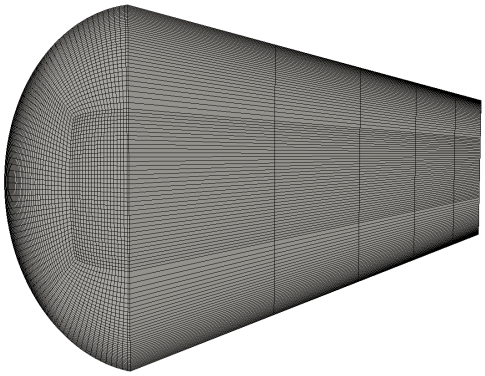

Figure 3.34: *Mesh for OpenFOAM and FLUENT*

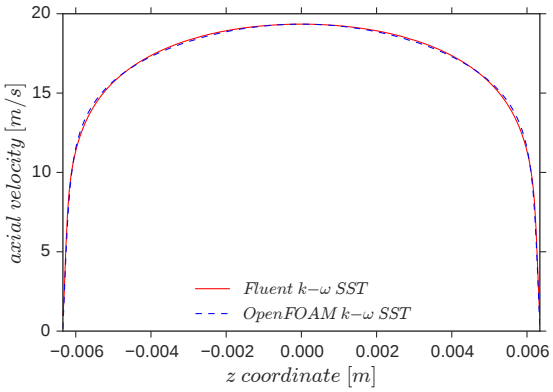

Figure 3.35: *Velocity profiles with OpenFOAM and FLUENT*

Figure 3.36: *Mesh and velocity profiles obtained with OpenFOAM and FLUENT*

To ensure that the flow solution is correct, the pipe outlet velocity profile obtained with OpenFOAM has been compared to the velocity profile generated with FLUENT, considering the same thee-dimensional mesh, see Figure 3.34. For these simulations, the k-ω SST turbulence model was used. Figure 3.35 shows the velocity profiles obtained with the open source and the commercial flow solvers. As can be seen, the velocity profiles are identical, this provides confidence in the flow settings and calculation with OpenFOAM.

As difficulties were encountered when trying to import the previous mesh in Code_Saturne, a slightly different mesh was generated with the mesh generator Salome, which is fully compatible with this open source flow solver. The corresponding mesh is shown on Figure 3.37.

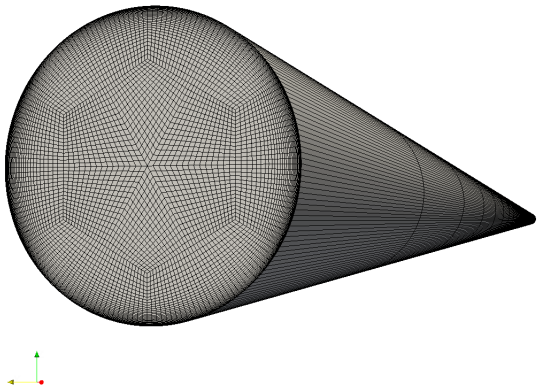

Figure 3.37: *Mesh for Code_Saturne*

Simulations performed with Code_Saturne were run either with the k-ω SST turbulence model or with the BL-$\overline{v^2}/k$ formulation which is based on the $\overline{v^2} - f$ model, a low Reynolds turbulence model. The turbulent kinetic energy dispersion rate can indeed often be seen as an asymptotic droplet diffusivity value for droplets that closely follow the flow (Paras & a.J. Karabelas, 1991).

Figure 3.38 shows the dimensional velocity profile in the radial direction, from the bottom (z = pipe radius) to the centre (z = 0) of the pipe. Although being obtained with different meshes and software, it appears clearly that the velocity profile is similar with nearly all turbulence models investigated in this work. Only the Reynolds Stress LRR model implemented in OpenFOAM produced a slightly different velocity profile, with values slightly higher in the central part of the pipe. Figure 3.39 shows the corresponding non-dimensional velocities which can be compared to the theoretical asymptotic values of the law of the wall. The wall gradient can therefore be determined and used to get the friction velocity and the dimensionless velocity u^+. From all models tested, the $k - \omega$ turbulence model in OpenFOAM seems to show the closest match to the theoretical values.

The turbulence kinetic energy predicted with all models is plotted in Figure 3.40. As expected, the choice of the turbulence model highly affects the prediction of this quantity. A significant discrepancy is noticeable between the LRR model and all other models, where the predicted turbulence kinetic energy values are twice as high. Figure 3.41 shows the corresponding non-dimensionalised values which are compared to a DNS carried out by Kim *et al.* (1987).

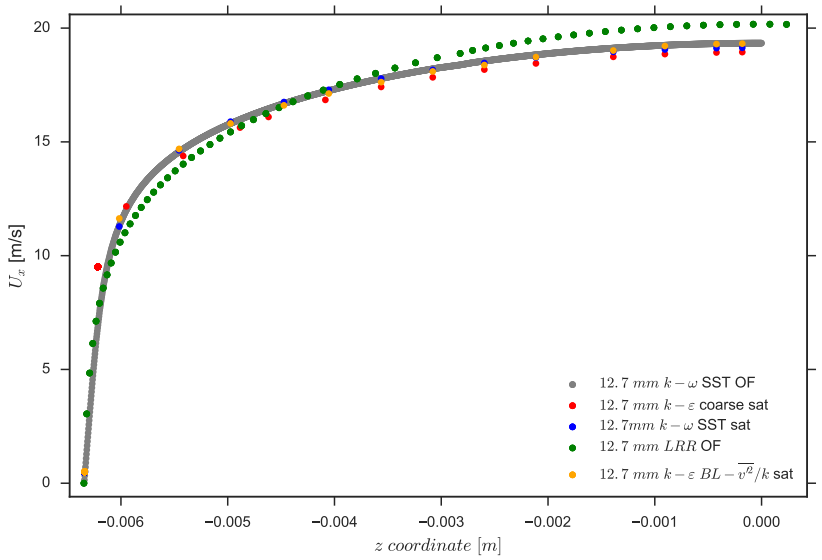

Figure 3.38: *Axial velocities for various turbulence models in the 12.7 mm id pipe*

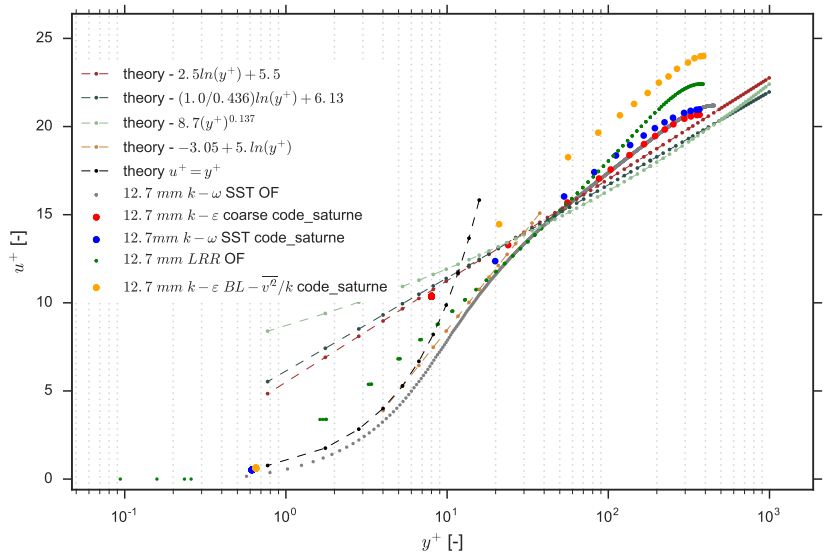

Figure 3.39: *Non-dimensional axial velocities for various turbulence models in the 12.7 mm id pipe*

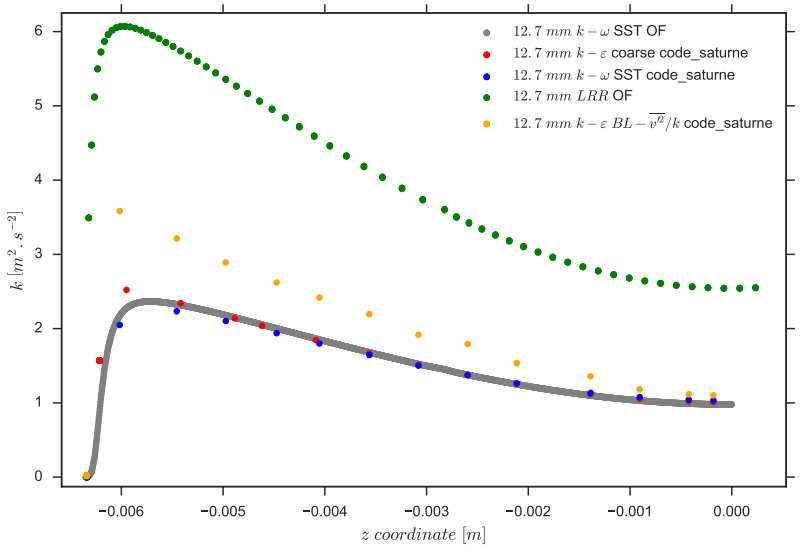

Figure 3.40: *TKE for various turbulence models in the 12.7 mm id pipe*

For this size of pipe, it can clearly be established that no single model tested here was able to correctly and simultaneously predict both the peak radial position (around $y^+ = 16$) and the overall intensity of k^+. Models are either best to predict the peak radial position or the overall amplitude (around $k^+ = 4.3$) but not both. Friction velocity and pressure drop values could be extracted from all simulations, they are reported in Table 3.4 along with the values obtained with the Blasius correlation. When looking are the friction velocity, results are comparable, apart from the value generated with the LLR model in OpenFOAM which is much higher than the values obtained with the other numerical models and also much higher than the Blasius-based one. The lowest friction velocity is obtained with the BL-v^2/k (Code_Saturne). Similarly, the LRR (OpenFOAM) model highly over-predicts the pressure drop when compared to values from the other models and to the Blasius correlation. The BL-v^2/k (Code_Saturne) model also over-predicts the pressure drop. At this stage, when comparing the results reported in this table, the $k-\omega$ SST and the $k-\varepsilon$ models from Code_Saturne and the $k-\omega$ SST from OpenFOAM seem to be best for this study.This is an important result for guidance when using Open source numerical models.

Table 3.4: *Simulation results for the 12.7 mm pipe*

Turbulence model	Predicted friction velocity (m/s)	Predicted pressure drop (Pa/m)
BL-v^2/k (Code_Saturne)	0.8046	364.11
$k-\omega$ SST (Code_Saturne)	0.9124	327.79
$k-\omega$ SST (OpenFOAM)	1.0392	343.38
$k-\varepsilon$ (Code_Saturne)	0.9165	330.23
LRR (OpenFOAM)	1.7800	895.64
Blasius correlation	0.9500	344.00

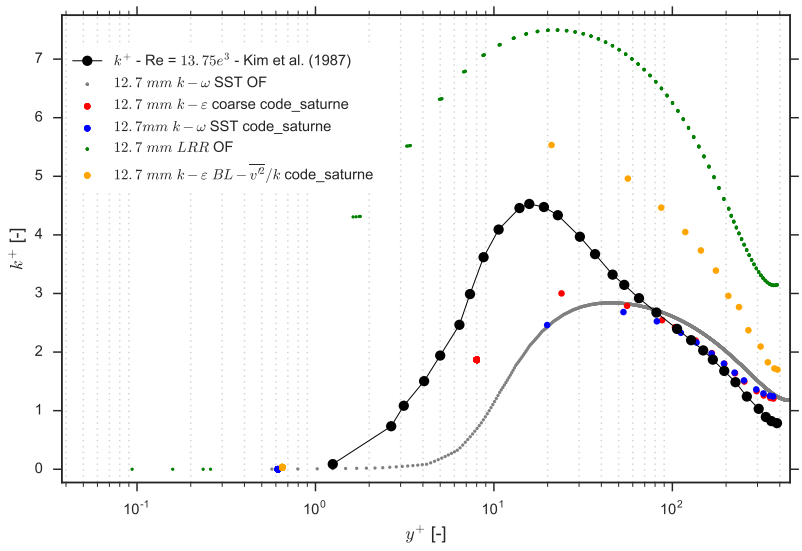

Figure 3.41: *Non-dimensional TKE for various turbulence models in the 12.7 mm id pipe*

3 in. ($\simeq 76.2mm$) diameter pipe

The 3 in. diameter pipe has been selected as experimental and numerical data for such diameters are reported in the literature. For the conditions listed in Table 3.5, a friction velocity of $0.04\ m/s$, a pressure drop of $56.54\ Pa/m$ and a wall shear stress of $1.4\ Pa$ can be deducted from the Blasius correlation.

Table 3.5: *Flow conditions for oil in pipe*

U_f (m/s)	ρ_f (kg/m^3)	μ_f $(Pa.s)$	Re $(-)$
0.51	873.47	2.0×10^{-2}	$1,696$

Note that for Reynolds numbers below 2,000, the flow is considered laminar, and thus the laminar correlation $\Lambda = 64/Re$ needs to be applied. Turbulence models are usually not adapted for such low Reynolds numbers as they often assume fully turbulent flow conditions. Among all models investigated, the v2-f model from Code_Saturne predicts a laminar flow where the other models predict a turbulent flow. It is thus expected from most turbulence models to produce erroneous results as they assume some level of turbulence where none is present. Nevertheless, it has been estimated that it would be useful to present the results from this study.

All models apart from the LRR (OpenFOAM) where the values are over-predicted, show a friction velocity and a pressure drop in agreement with the Blasius correlation, see Table 3.6. When looking at the pressure drop, the best match with Blasius is obtained with the BL-v^2/k model in Code_Saturne. The $k-\omega$ SST versions implemented in Code_Saturne and OpenFOAM produced identical friction

Table 3.6: *Simulation results for the 3 in. pipe*

Turbulence model	Predicted friction velocity (m/s)	Predicted pressure drop (Pa/m)
BL-v^2/k (Code_Saturne)	0.0351	58.64
$k-\omega$ SST (Code_Saturne)	0.0447	97.87
$k-\omega$ SST (OpenFOAM)	0.0454	92.89
LRR (OpenFOAM)	0.0624	383.38
Blasius correlation	0.0400	56.54

velocity and pressure drop results. However, although the friction velocity is in agreement with Blasius, the pressure drop is over-predicted with both models.

Based on this table, the BL-v^2/k (Code_Saturne) model agrees better with the laminar-based Blasius correlation. As mentioned previously, only this turbulence model predicts a laminar flow. The other models consider that the flow is fully turbulent, this is clearly visible when looking at the velocity profiles plotted on Figure 3.42.

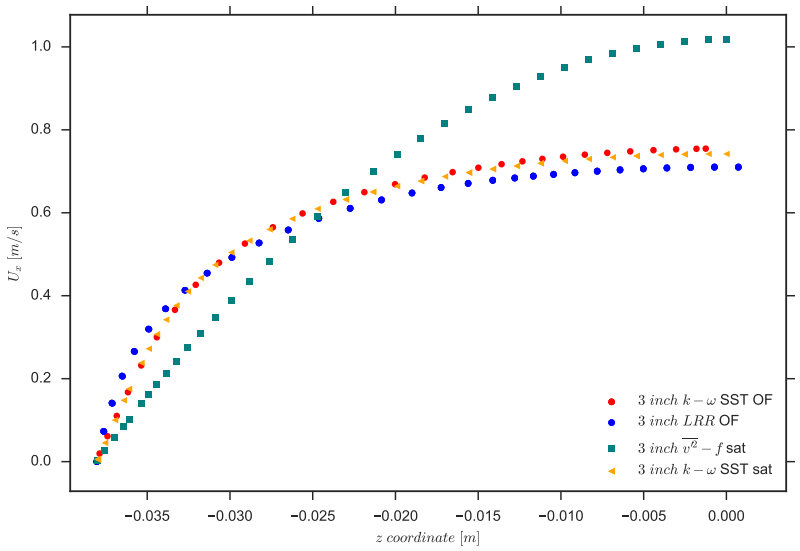

Figure 3.42: *Velocity profile in the 3 in. pipe*

The mean velocities predicted from the $k-\omega$ SST models in both Open source codes match the expected asymptotic values, see Figure 3.43. The under-prediction of u^+ for the LRR model is due to the non-dimensionalisation process, as a reliable near-wall gradient was difficult to obtain.

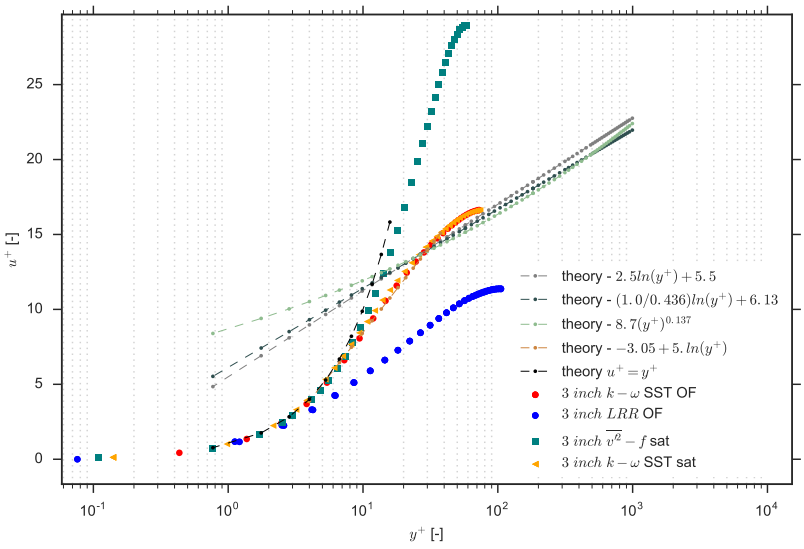

Figure 3.43: *Non-dimensional velocity profiles in the 3 in. pipe*

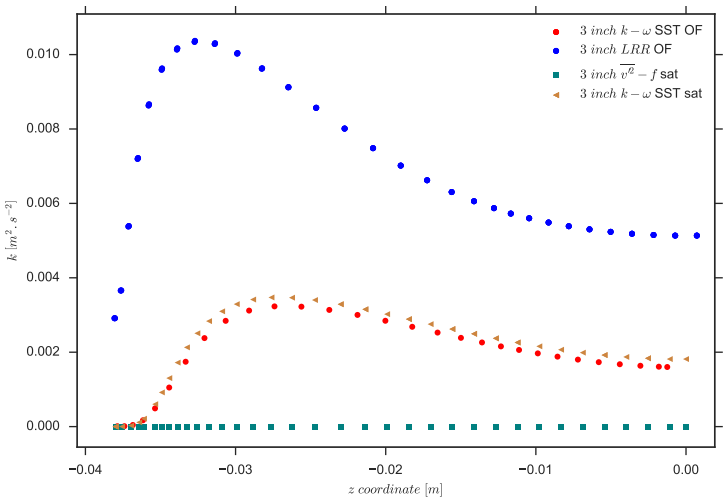

Figure 3.44: *Dimensional turbulent kinetic energy profile in the 3 in. pipe*

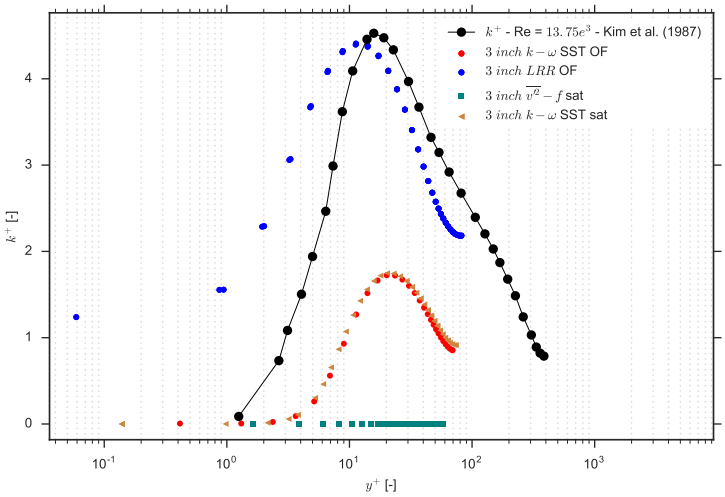

Figure 3.45: *Non-dimensional turbulent kinetic energy profile in the 3 in. pipe*

Although two different meshes have been used, Figure 3.44 shows that the turbulent kinetic results from OpenFOAM and Code_Saturne are very similar. The amplitude of the turbulent kinetic energy predicted by the OpenFOAM LRR model is higher than the one from the $k-\omega SST$ model. On the contrary, the $v2-f$ model fails to predict turbulence, hence a null value corresponding to a laminar flow. Figure 3.45 compares the various models with the turbulent flow data from Kim *et al.* (1987). Although such comparison is somehow meaningless as the Reynolds number is about 1,696, it is still interesting to notice that the peak location is relatively well predicted. In terms of amplitude, the LRR models seems to be of the same order of magnitude than what can be expected for a turbulent flow.

3.3.2 Medium diameter pipes

Medium diameter pipes are pipes rarely studied experimentally or numerically. Results in pipes of diameter 14.5 in. are therefore difficult to find in the literature. Studying the flow in such pipe has been motivated by the fact that a transition between small diameter pipes and large diameter pipes should be established for a better comparison and discussion on a scaling-up strategy from laboratory-type models to large industrial-type models.

14.5 in. ($\simeq 368.3$mm) diameter pipe

The flow conditions used for this case are written in Table 3.7. The Blasius correlation (smooth walls) predicts a wall shear stress around 2.25 Pa, leading to a friction velocity of 0.05 m/s and a pressure drop around 24 Pa/m. The meshes displayed on Figures 3.46 and 3.47 have been used for the low and high Reynolds turbulence models, respectively.

Table 3.7: *Flow conditions for oil in pipe*

U_f (m/s)	ρ_f (kg/m^3)	μ_f $(Pa.s)$	Re $(-)$
0.84	868.8	2.0×10^{-2}	$13,460$

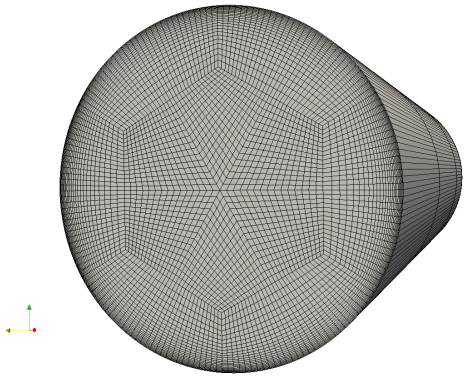

Figure 3.46: *Low Reynolds number mesh for the 14.5 in. pipe*

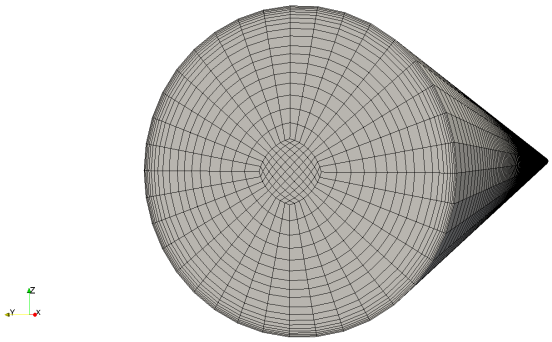

Figure 3.47: *High Reynolds number mesh for the 14.5 in. pipe*

Figure 3.48 shows the velocity profiles obtained with various turbulence models, including the Reynolds Stress model from FLUENT. Predictions from the v2f model in OpenFOAM and from the linear $k-\varepsilon$ model in Code_Saturne are significantly diverging from other predictions, with the linear $k-\varepsilon$ performing very poorly. The estimates from $k-\omega$ SST and v2f from Code_Saturne, and the $k-\omega$ SST from OpenFOAM, are in agreement with the RSM-based profile from FLUENT. When comparing the dimensionless velocity with the theoretical asymptotic values in Figure 3.49, it appears that both $k-\omega$ SST based results from OpenFOAM and Code_Saturne are fairly close to the theoretical values. As mentioned previously, small variations in the estimates of the friction velocity (see Table 3.8) can cause an erroneous representation in the non-dimensionalised space. This is most certainly the reason behind the discrepancies obtained between the RSM based results from Fluent and the theoretical values; this model should perform better than any other RANS model investigated here as it is the only model which takes into account the full anisotropic turbulence of the flow.

Figures 3.50 and 3.51 show the turbulent kinetic energy for this case in their dimensional and non-dimensional form, respectively. The turbulent kinetic energy representation allows a comparison of all turbulence models, including those which are not able to predict the perturbation velocity of components u', v' and w'. The linear $k-\varepsilon$ model of Code_Saturne largely over-predicts this quantity when compared to other models and the results from the v2f model of OpenFOAM are under-predicted, see Figure 3.50. When looking at the position of the peak of dimensionless turbulent intensity in Figure 3.51, the best matches with Kim *et al.* (1987) are obtained with the v2f model in Code_Saturne and with the RSM of

Fluent. In terms of height, $k-\omega$ SST (OpenFOAM) and v2f (Code_Saturne) agree better with the non-dimensionalised DNS results.

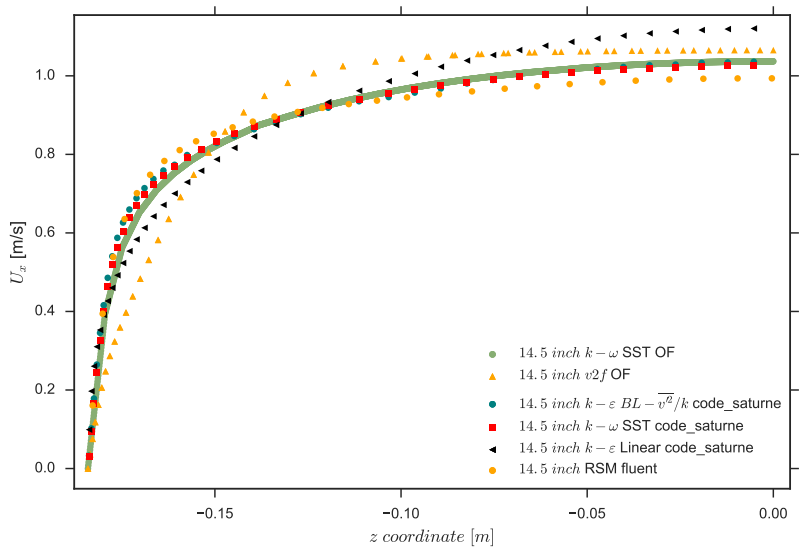

Figure 3.48: *Velocity profile in the 14.5 in. pipe*

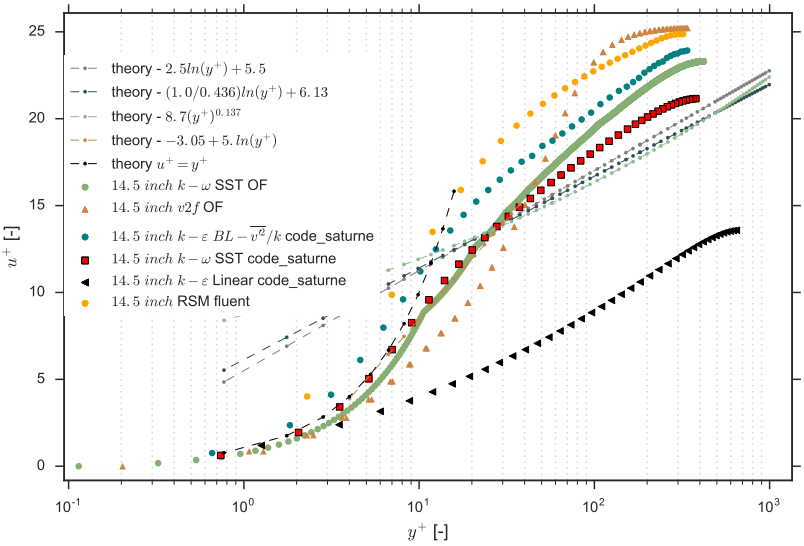

Figure 3.49: *Non-dimensionnalized velocity profile in the 14.5 in. pipe*

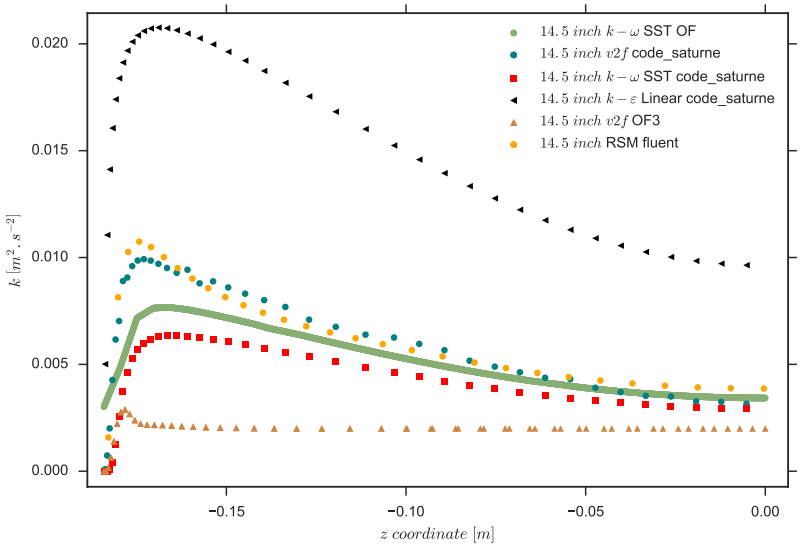

Figure 3.50: *Dimensional turbulent kinetic in the 14.5 in. pipe*

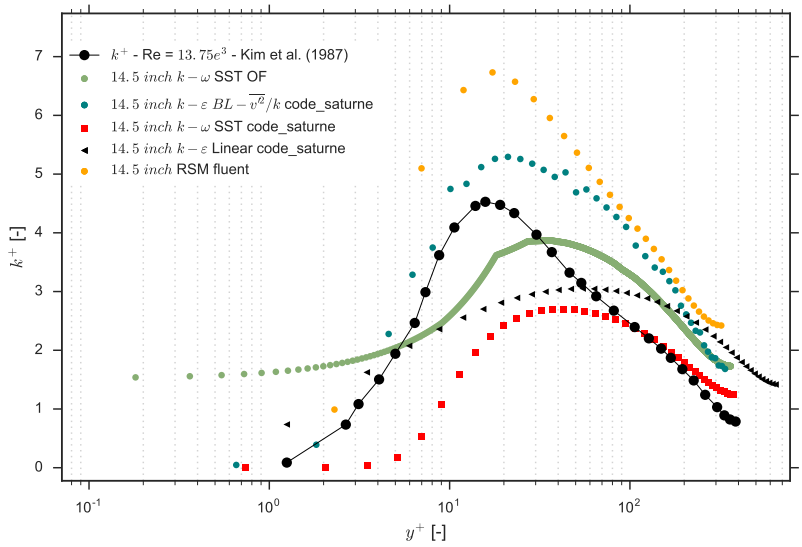

Figure 3.51: *Non-dimensional turbulent kinetic in the 14.5 in. pipe*

The results of the various turbulent models tested are summarized in Table 3.8. All codes estimates of friction velocity are in agreement with the Blasius correlation apart from the linear $k-\varepsilon$ in Code_Saturne. When looking at the pressure drop, all codes apart from the v2f model in OpenFOAM and the linear $k-\varepsilon$ in Code_Saturne agree with values derived from experiments.
It is worth noting that for an unknown reason, the turbulent kinetic energy pattern obtained with the $v-2f$ model in Code_Saturne shows a strange anisotropy behaviour while the Reynolds stress model in Fluent shows a more realistic behaviour, see Figures 3.52 and 3.53. As this phenomenon cannot be explained by the flow physics, it can only be assumed that this is due to a numerical problem. Different meshes have been tested and periodic boundary conditions

Table 3.8: *Simulation results for the 14.5 in. pipe*

Turbulence model	Predicted friction velocity (m/s)	Predicted pressure drop (Pa/m)
BL-v^2/k (Code_Saturne)	0.0433	25.65
$k-\omega$ SST (Code_Saturne)	0.0485	22.43
$k-\omega$ SST (OpenFOAM)	0.0445	22.04
$k-\varepsilon$ Linear (Code_Saturne)	0.0825	74.00
$v2-f$ (OpenFOAM)	0.0377	15.14
$RSM-LRR$ (Fluent)	0.0399	27.58
Blasius correlation	0.0509	24.00

implemented. In all cases, a similar anisotropy was present when applying the $v-2f$ model.

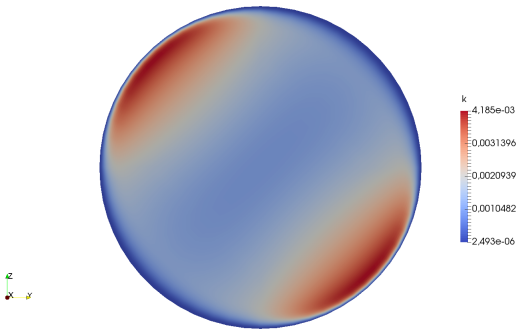

Figure 3.52: *Outlet distribution of k in the 14.5 in. pipe with Code_Saturne (BL-v^2/k model)*

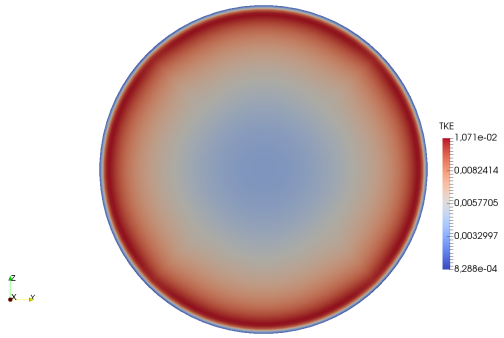

Figure 3.53: *Outlet distribution of k in the 14.5 in. pipe with Fluent (RSM model)*

3.3.3 Large diameter pipe

48 in. ($\simeq$ 1219.2mm) diameter pipe

The flow conditions used for this study are written in Table 3.9. When applying the Blasius correlation, a wall shear stress value around1.7 Pa is obtained, which gives a friction velocity around 0.044 m/s.

Table 3.9: *Flow conditions for oil in pipe*

U_f (m/s)	ρ_f (kg/m^3)	μ_f $(Pa.s)$	Re $(-)$
0.84	873.47	2.0×10^{-2}	$43,460$

Results generated for this pipe were qualitatively better than for other previous pipes; this is probably due to the high Reynolds number obtained in the large pipe, where turbulence models are expected to be more reliable. Based on the previous test cases, it was expected that the $k-\omega$ SST model and the BL-v^2/k mode would offer similar performance. For this reason, only these models have been compared here.

As can be seen in Figure 3.54, all velocity profiles obtained with the two different turbulence models are similar. Near the centreline, the BL-v^2/k model predicts a slightly larger mean velocity though.

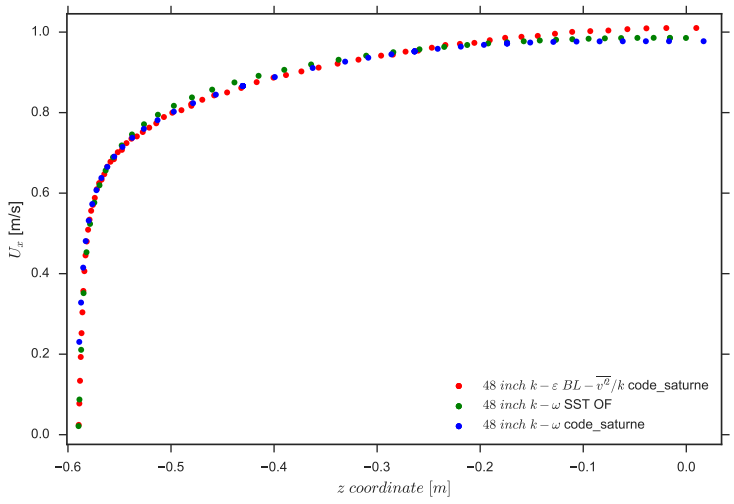

Figure 3.54: *Axial velocity component in a 48 in. diameter pipe; comparison between $k-\omega$ SST and $v2f$*

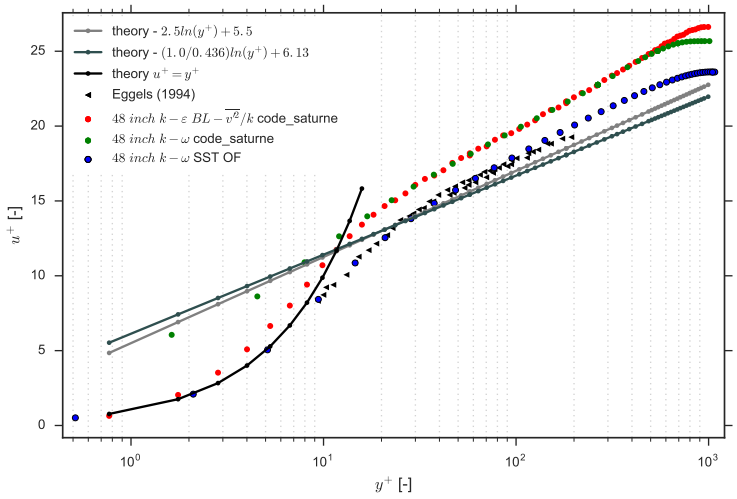

Figure 3.55: *Axial velocity component in a 48 in. diameter pipe; comparison BL-v^2/k from Code_Saturne vs Eggels(1994)*

Non-dimensional mean velocities are compared to the theoretical values and to the experimental estimates from Eggels *et al.* (1994) in Figure 3.55. The OpenFOAM prediction is fairly close to the results from Eggels *et al.* (1994) and to the theoretical asymptotes. The overall non-dimensional velocity predicted by Code_Saturne is higher than the theoretical values, but evolves past $y^+ = 10$ with a slope comparable to the theoretical one. The two predictions from Code_Saturne are also nearly identical past $y^+ = 10$. It is likely that the near-wall spacing of the mesh used for the $k-\omega$ SST turbulence model in Code_Saturne is not refined enough to follow the usual $U^+ = y^+$ below $y^+ = 5$.

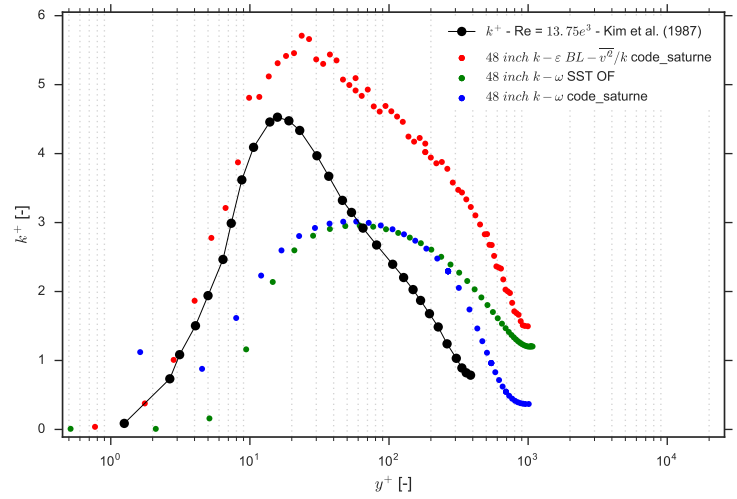

Figure 3.56: *Turbulent kinetic energy in a 48 in. diameter pipe*

Figure 3.56 describes the simulated non-dimensioned turbulent kinetic energy

plotted against the DNS results from Kim *et al.* (1987). The $k-\omega$ SST fails to correctly predict the turbulent kinetic energy, as it under-predicts the amplitude and the peak position is well above the usual value $y^+ \approx 16$. However the BL-v^2/k model from Code_Saturne seems to have a better agreement with Kim *et al.* (1987). This model should be privileged when studying the turbulent fields is important, for instance, when analysing particle dispersion and deposition.

The friction velocity and the pressure drop from all simulations are reported in Table 3.10. All numerical results are in agreement with the Blasius correlation, the farthest estimates being obtained with the $v2f$ model in Code_Saturne.

Table 3.10: *Simulation results for the 48 in. pipe*

Turbulence model	Predicted friction velocity (m/s)	Predicted pressure drop (Pa/m)
BL-v^2/k (Code_Saturne)	0.0379	6.18
$k-\omega$ SST (Code_Saturne)	0.0380	4.50
$k-\omega$ SST (Open_FOAM)	0.0417	5.07
Blasius correlation	0.0440	5.00

3.4 Other industrial cases

The work developed in this thesis was used for industrial applications as part of a commercial project. Only two geometries will be considered here, among various cases undertaken: the 3 in. perforated plate and the 3 in. valve.

3.4.1 Perforated plate

- **Injection**

Water droplets are injected when the oil flow solution has converged. Three particle size distributions were considered here with a water cut of 0.25 % by weight.

The following information, relative to the flow conditions in the 3 in. geometries,are used to determine the number of drops and mass flux to be injected in the domain.

- Pipe diameter $D = 3\ in. = 0.0762\ m$
- Volume flow rate $Q_t = 37\ US\ gal/min = 0.002334\ m^3 \cdot s^{-1}$
- Flow Temperature $T = 20^o F = -6.667^o C$

- Oil carrier density $\rho = 873.47\ kg \cdot m^{-3}$
- Weight percentage of water $wct = 0.25\ \%$

More details about the injection have been provided in Section 2.5.1.

- **Deposition**

The surfaces used to evaluate the droplets deposition mass flux on the perforated plate are shown in green on Figure 3.57. These surfaces are also the faces of the sampling boxes used to evaluate the collisions, using the technique described in Section 2.3.3. The surfaces that have a hole, do not include the hole as being part of the surface of deposition. Each face has been attributed a specific number which is used in this report to identify where the deposition has been evaluated.

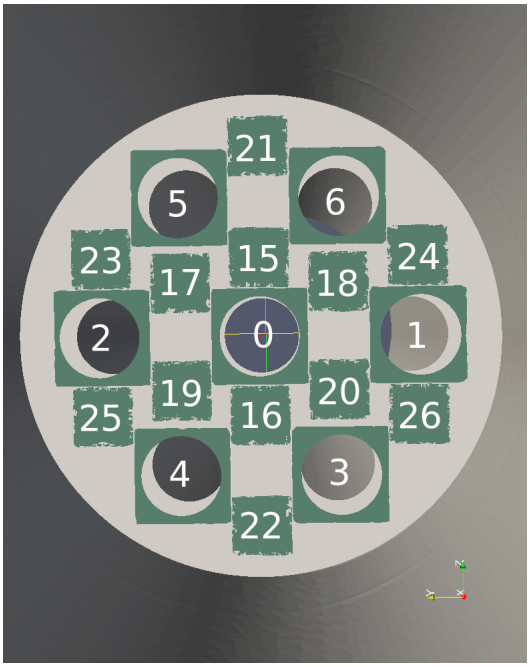

Figure 3.57: *Faces used for the droplets deposition on the perforated plate*

Figure 3.60 shows the sites where the droplets deposition has been determined upstream and downstream regions of the perforated plate.

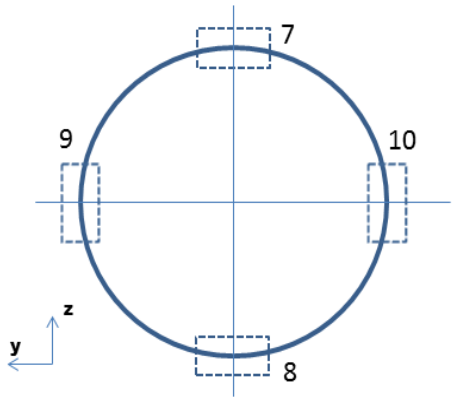

Figure 3.58: *0.5D upstream of the plate*

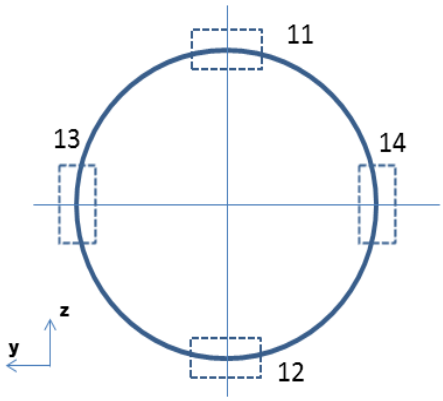

Figure 3.59: *1D downstream of the plate*

Figure 3.60: *Deposition sites for the perforated plate geometry*

The deposition mass flux obtained on the perforated plate case (7 holes, 20F) is summarized in Table 3.11. The deposition surface IDs (Column 1) are those displayed previously on Figure 3.57 for the perforated plate itself (ID 0-6 and 15-26).

IDs 7-14 correspond to locations on the wall upstream (ID 7-10) and downstream (ID 11-14) of the plate. The second column lists the surface areas considered. To avoid any overlapping of surface, surfaces have been taken larger around the holes(ID 0-6) than at other locations on the plate (ID 15-26). The columns labelled M1, M2 and M3 refer to the 9 μm, 25 μm and 41 μm droplets, respectively.

As expected, the deposition mass flux (Column 3 in Table 3.11) is the highest in the vicinity of the holes edges, this is confirmed on Figures 3.61 to 3.63. In addition, a nearly identical ratio of droplets of sizes 9μm and 25μm deposit in these regions ($\simeq 30\%$), however very slightly higher for the 41μm droplets ($\simeq 35\%$). It can be noticed that for all other surfaces considered, the rate of deposition is very low for the medium and the largest size droplets. An increase of the number of droplets would potentially produce a more accurate result with values different from zero. However, the deposition rate in these regions would still remain very low.

Table 3.11: *Summary of droplet deposition for the* $3\ in.$ *perforated plate geometry (7 holes, 37 US gals/min, 20F)*

ID	S_{dep}	M_{dep}	M1	M2	M3	Percentage of M_{dep}		
	m^2	kg/m^2-s	kg/m^2-s	kg/m^2-s	kg/m^2-s	M1	M2	M3
0	1.06E-04	2.07E-01	6.07E-02	7.43E-02	7.18E-02	29.35%	35.93%	34.71%
1	1.06E-04	1.72E-01	6.31E-02	6.31E-02	4.59E-02	36.64%	36.67%	26.70%
2	1.06E-04	2.16E-01	7.29E-02	6.80E-02	7.47E-02	33.82%	31.54%	34.64%
3	1.06E-04	2.35E-01	7.66E-02	8.37E-02	7.47E-02	32.60%	35.61%	31.79%
4	1.06E-04	2.50E-01	7.50E-02	6.87E-02	1.06E-01	30.00%	27.49%	42.51%
5	1.06E-04	2.39E-01	7.95E-02	6.50E-02	9.48E-02	33.23%	27.16%	39.61%
6	1.06E-04	2.55E-01	7.73E-02	8.05E-02	9.76E-02	30.27%	31.50%	38.22%
7	2.97E-04	8.78E-04	4.12E-04	4.65E-04	0.00E+00	46.97%	53.03%	0.00%
8	2.97E-04	6.11E-04	4.11E-04	1.99E-04	0.00E+00	67.35%	32.65%	0.00%
9	2.97E-04	3.91E-04	3.91E-04	0.00E+00	0.00E+00	100.00%	0.00%	0.00%
10	2.97E-04	6.23E-04	3.57E-04	2.66E-04	0.00E+00	57.34%	42.66%	0.00%
11	2.97E-04	4.40E-04	1.74E-04	2.66E-04	0.00E+00	39.49%	60.51%	0.00%
12	2.97E-04	2.17E-04	2.17E-04	0.00E+00	0.00E+00	100.00%	0.00%	0.00%
13	2.97E-04	6.12E-04	4.13E-04	1.99E-04	0.00E+00	67.41%	32.59%	0.00%
14	2.97E-04	1.32E-03	3.90E-04	9.31E-04	0.00E+00	29.53%	70.47%	0.00%
15	8.97E-05	6.79E-03	1.43E-03	1.98E-03	3.38E-03	21.09%	29.13%	49.78%
16	8.97E-05	1.00E-03	1.00E-03	0.00E+00	0.00E+00	100.00%	0.00%	0.00%
17	8.97E-05	7.91E-04	7.91E-04	0.00E+00	0.00E+00	100.00%	0.00%	0.00%
18	8.97E-05	5.75E-04	5.75E-04	0.00E+00	0.00E+00	100.00%	0.00%	0.00%
19	8.97E-05	8.60E-04	8.60E-04	0.00E+00	0.00E+00	100.00%	0.00%	0.00%
20	8.97E-05	5.83E-03	1.79E-03	6.60E-04	3.38E-03	30.72%	11.31%	57.98%
21	8.97E-05	1.18E-03	1.18E-03	0.00E+00	0.00E+00	100.00%	0.00%	0.00%
22	8.97E-05	1.74E-03	8.60E-04	8.80E-04	0.00E+00	49.43%	50.57%	0.00%
23	8.97E-05	1.77E-03	1.11E-03	6.60E-04	0.00E+00	62.76%	37.24%	0.00%
24	8.97E-05	1.56E-03	8.97E-04	6.60E-04	0.00E+00	57.62%	42.38%	0.00%
25	8.97E-05	2.66E-03	8.96E-04	1.76E-03	0.00E+00	33.76%	66.24%	0.00%
26	8.97E-05	9.33E-04	9.33E-04	0.00E+00	0.00E+00	100.00%	0.00%	0.00%

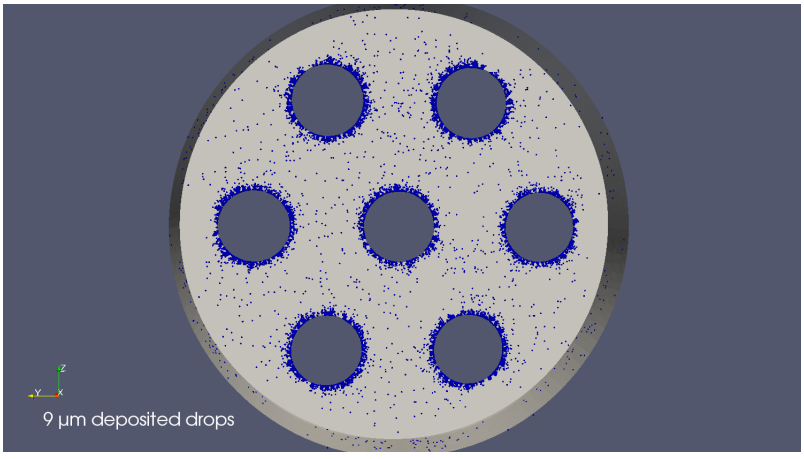

Figure 3.61: $9\ \mu m$ *droplets deposition at 1s on the 7 holes perforated plate,* $3\ in.$*, 20F*

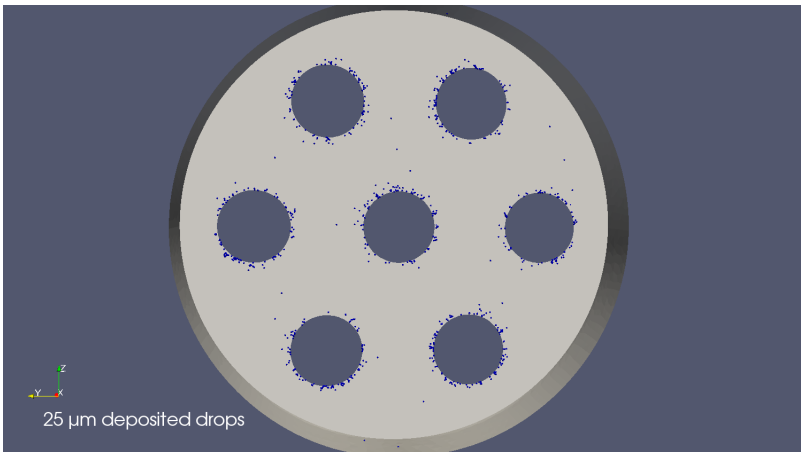

Figure 3.62: *25 μm droplets deposition at 1s on the 7 holes perforated plate, 3 $in.$, 20F*

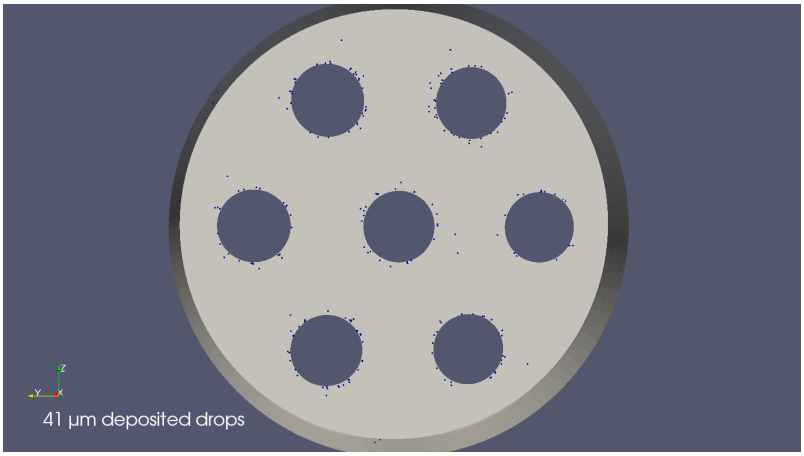

Figure 3.63: *41 μm droplets deposition at 1s on the 7 holes perforated plate, 3 $in.$, 20F*

It can be seen from Figures 3.61 to 3.63 that the smallest droplets are the ones depositing the most on the front side of the perforated plate while only a few of the largest ones deposit in this region. This is entirely due to the over-representation of very small drops over the larger drops, as given by the Particle Size Density. It can also be noticed that, independently of their size, most of the droplets deposit next to the hole edges. The following section will describe the droplet deposition in the 3 in. valve geometry.

3.4.2 Valve

3 in. Clapper Valves

All the flow cases are highly turbulent and a $k-\omega$ SST two-equation turbulence model by Menter (1993) has been used to capture the effects of the fluctuations on the flow. The flow settings are the same as those previously presented for the 3 in. straight pipe.

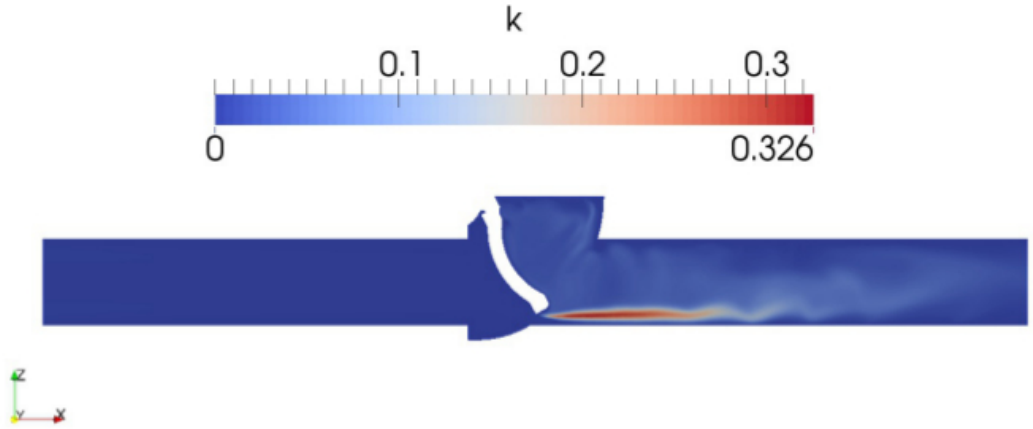

Figure 3.64: *Turbulent kinetic energy k ($\mathrm{m^2 s^{-2}}$) - vertical mid-plane.*

Figures 3.64 and 3.65 show the turbulent kinetic energy k and the turbulent viscosity ν_{turb} for the 37 gpm flow at 20F[1]. The maximum value of ν_t is about 25 times greater than the molecular (laminar) value at this temperature so turbulent transport is significant and has an effect on both the flow (in terms of the pressure drop) and the droplet transport. The highly turbulent region in the body of the pipe behind the valve is a result of the transport of turbulence which is generated in the 'jet'under the clapper.

In addition to the turbulence, another key feature of the flow (in terms of droplet transport) are vortices, which can increase the lift force of large particles. Regions of high vorticity and strain rate can also enhance deposition and droplet crowding.

Figure 3.66 shows streamlines computed around the valve. The flow is largely symmetric across the vertical mid-plane. Two pairs of vortices can be clearly seen:

[1]Recall that $\nu_{turb} = C_\mu k^2/\epsilon$, $C_\mu = 0.09$.

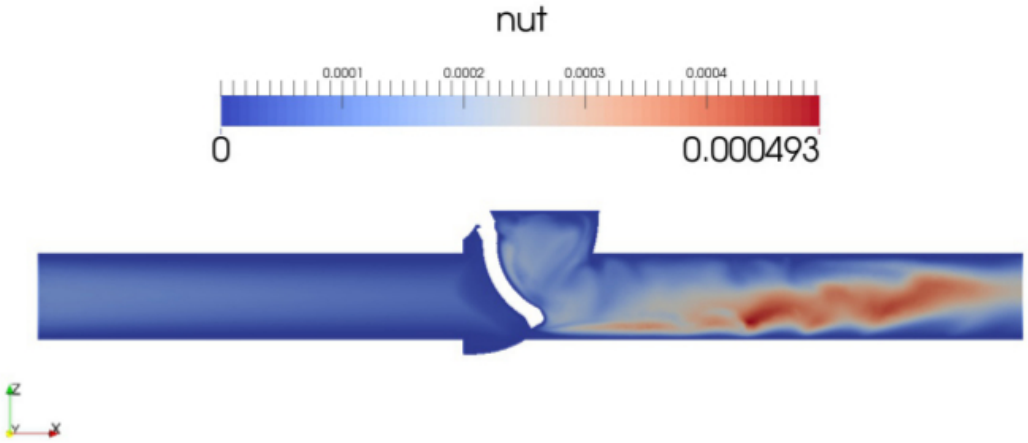

Figure 3.65: *Turbulent viscosity (ν_{turb} $\mathrm{m^2 s^{-1}}$) - vertical mid-plane.*

one pair upstream of the valve plate, the other one downstream. The downstream pair is significantly larger and stronger.

Figure 3.68 shows a close-up of stream lines immediately behind the valve (the flow rate is 37 US gal/min and the oil temperature is 40F). The flow behind the valve is more complex. The pair of large vortices behind the valve can be seen and the vortex is stretched and bent into the streamwise flow direction.

Another visualisation of the flow is given in Figure 3.69. Upstream of the valve, the irrotational core of the fluid can be seen. The vorticity is higher near the boundary walls, as shows the vectorial representation. Indeed, vorticity is produced near the walls and in other locations with high shear.

It is possible to see the more complex vortices behind the valve although it is clear that the highest levels of vorticity are generated below the valve where the flow accelerates strongly. At the end of the domain, the return to the undisturbed pipe flow conditions begin to appear.Note that this section is not the full extent of flow domain, which extends to seven diameters downstream of the sealing face of the valve.

Figures 3.70, 3.71, 3.72 and 3.73 show the interior of the valve and the casing. The coloured spheres show some of the deposition sites which confirm that the vortices and the regions of high vorticity are critical to the water droplet deposition. This includes (at the top of the casing) a line of drops which corresponds to the edges of the two vortices behind the valve and some deposition at the edge of the valve casing.

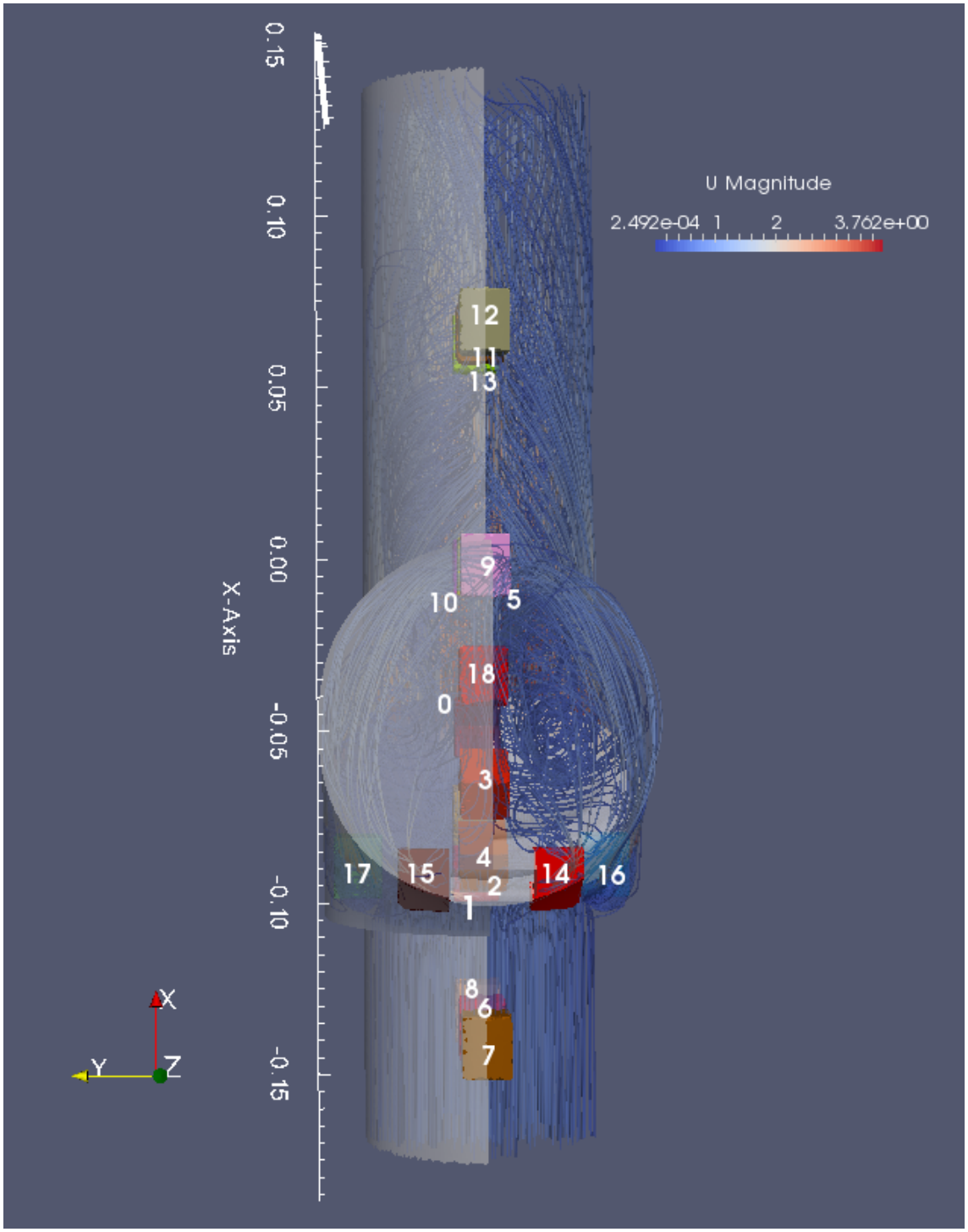

Figure 3.66: *Streamlines around the 3 in. valve; view from above. (37 US gals/min, 20F). (Boxes show regions where droplet transport, crowding and interactions are reported.)*

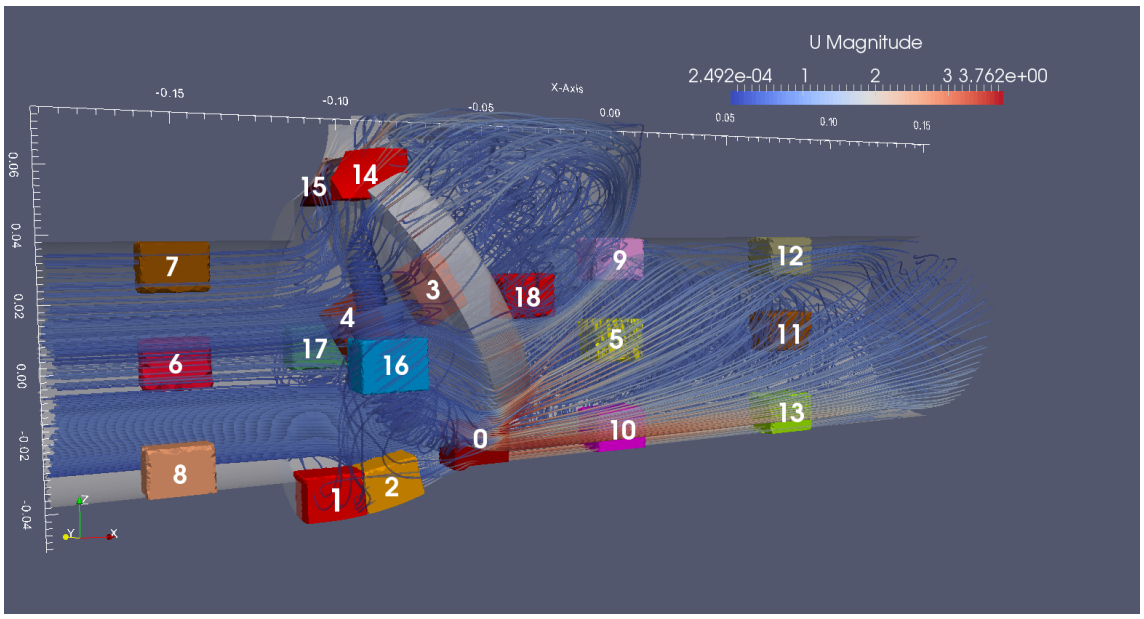

Figure 3.67: *Streamlines around the 3. valve; view from side; lines are coloured by speed in ms^{-1}.(37 US gal/min, 20F). (Boxes show regions where droplet transport, crowding and interactions are reported.)*

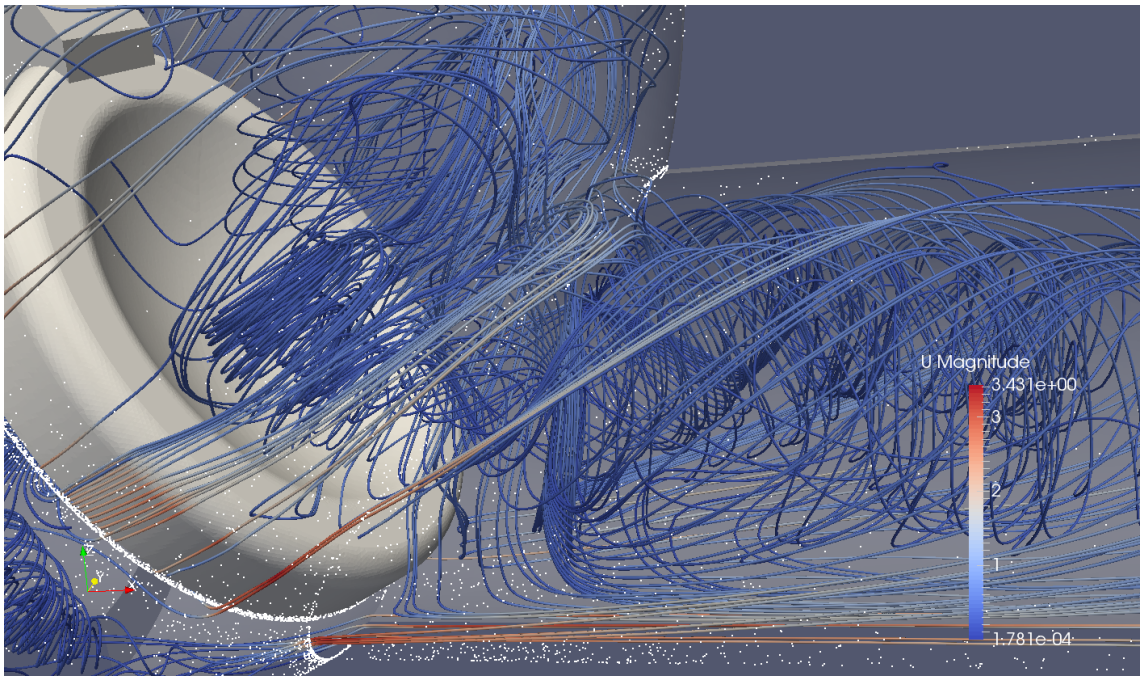

Figure 3.68: *Stream Lines around valve 40F. (37 US gal/min). Note the low velocity regions behind the clapper. Lines are coloured by speed in ms^{-1}. White dots are deposited droplets*

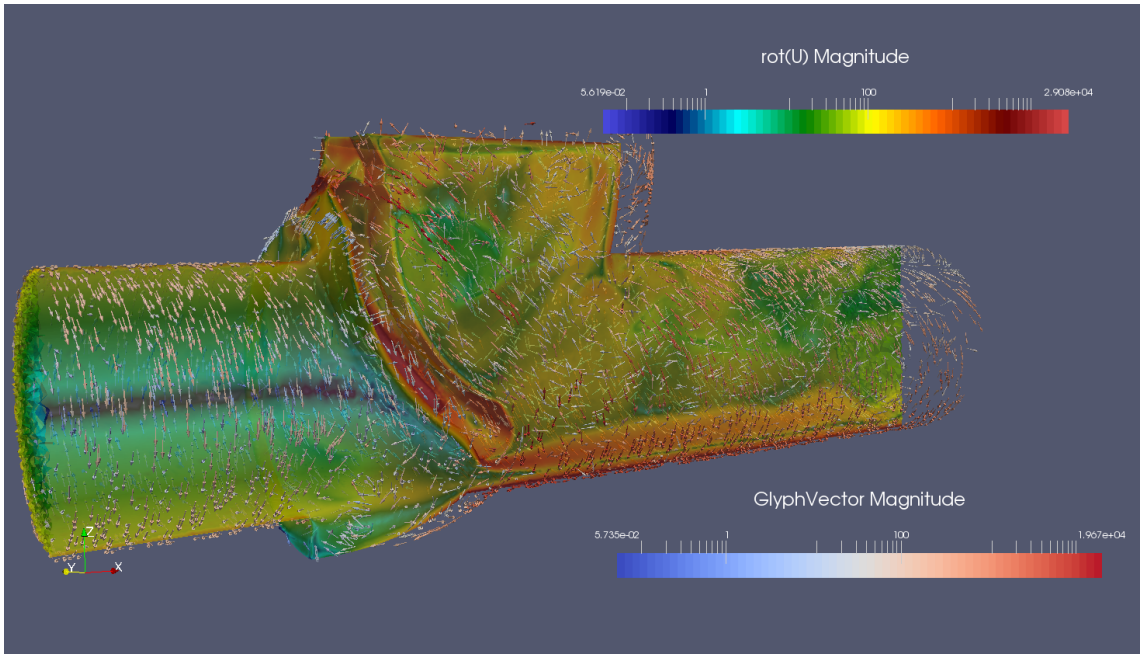

Figure 3.69: *Vorticity field around the valve: vorticity is a* **vector field** *(the units are s^{-1}): the background colour shows the vorticity magnitude on the vertical mid-plane; vectors show the local vorticity. Note the log scale. (Flow: 37 US gal/min, 20F)*

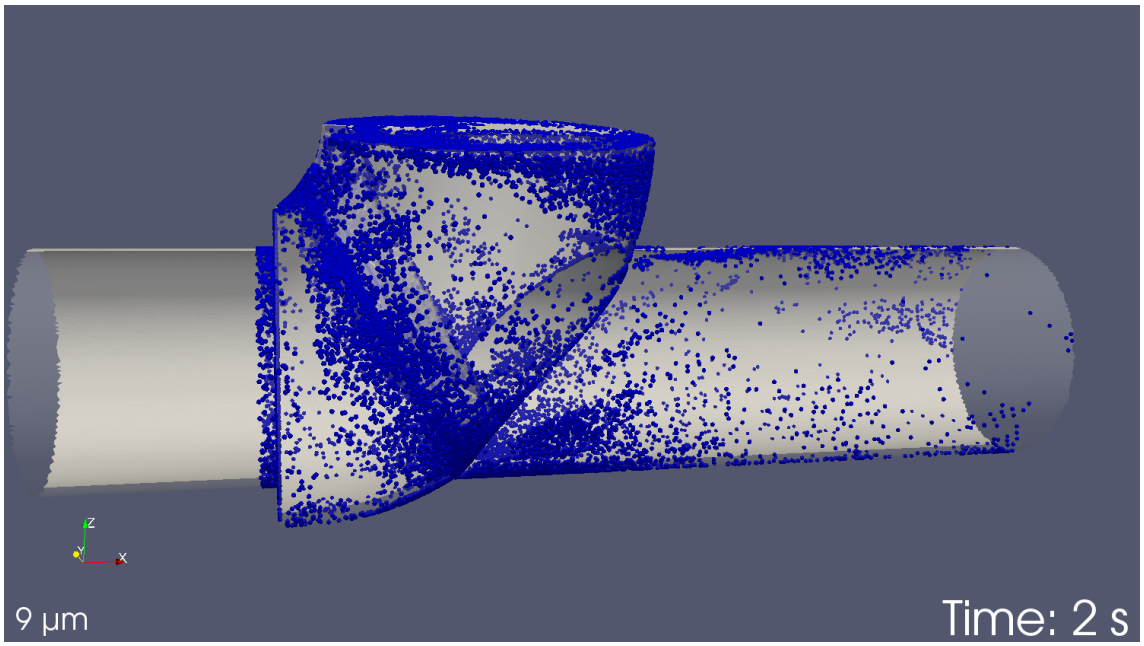

Figure 3.70: *Droplet deposition sites - 9μm drop size. (37 US gal/min, 20F).*

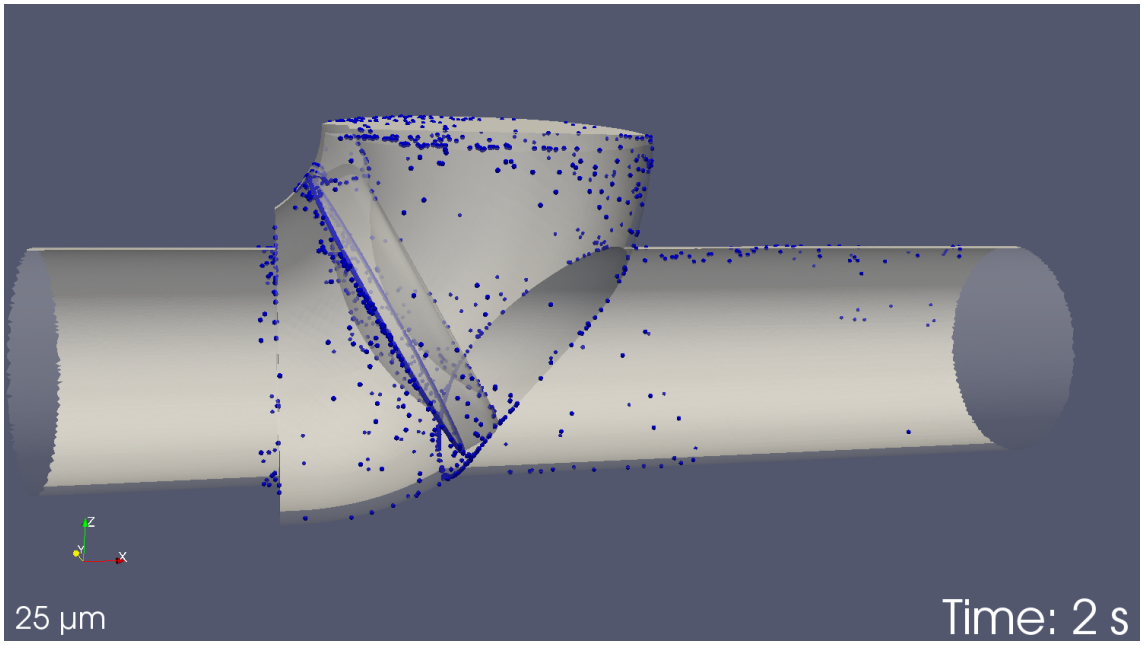

Figure 3.71: *Droplet deposition sites - 25μm drop size. (37 US gal/min, 20F).*

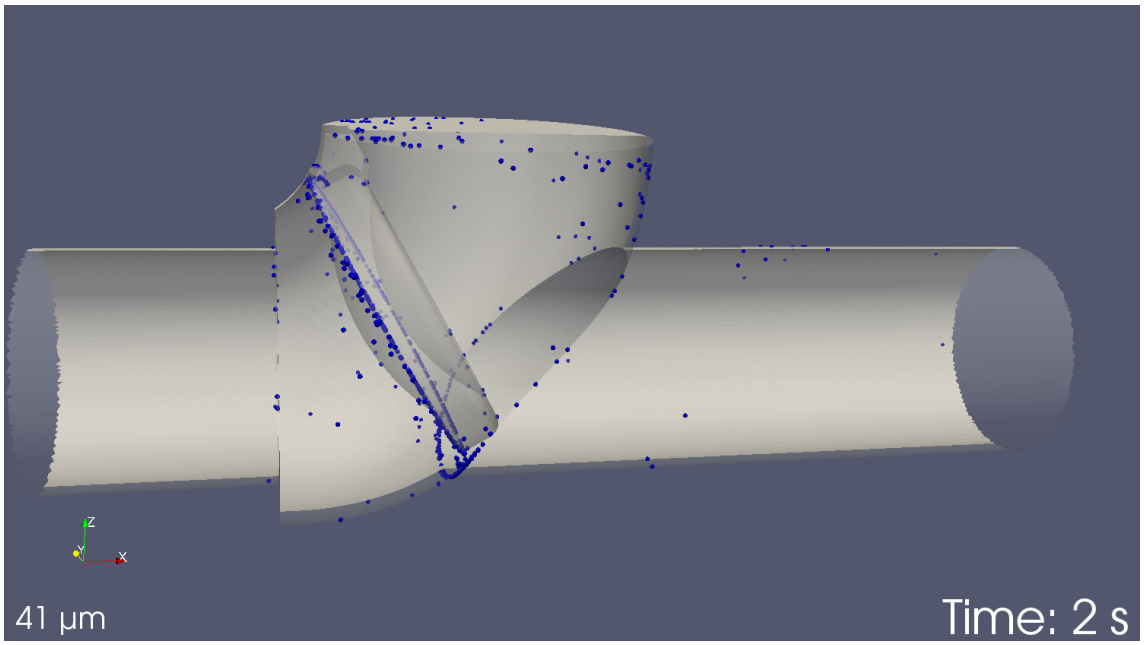

Figure 3.72: *Droplet deposition sites - 41μm drop size. (37 US gal/min, 20F).*

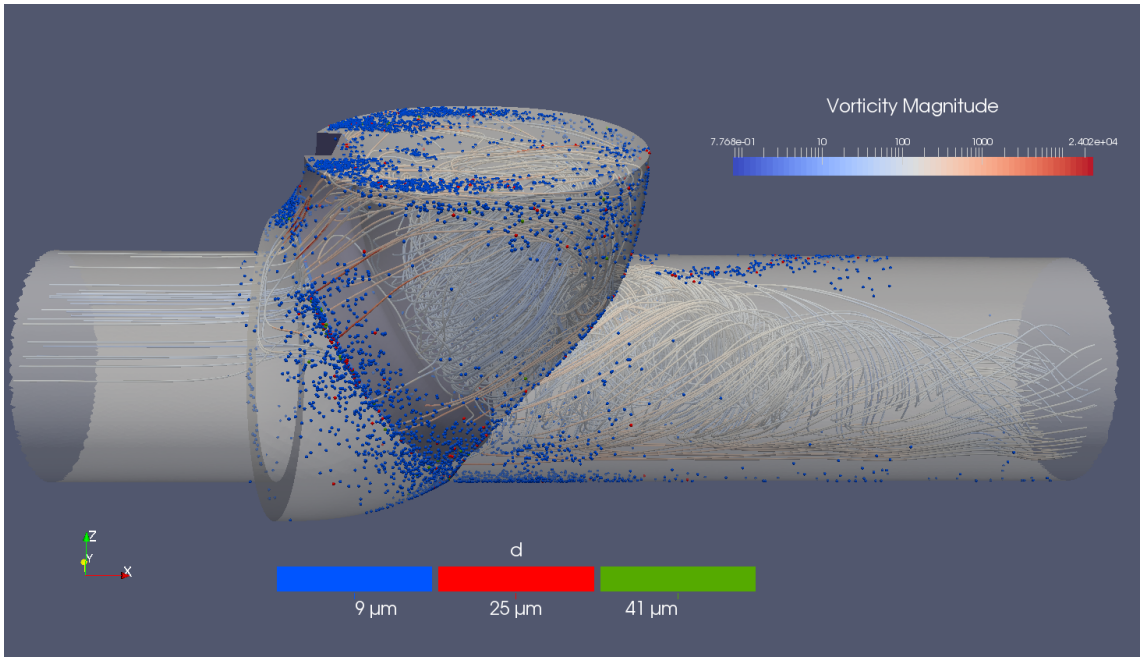

Figure 3.73: *Droplet deposition sites - all drop sizes and streamlines at $t = 1s$. (37 US gal/min, 20F).*

Figure 3.74 shows the droplet deposition sites for the 3 in. valve geometry; below a more detailed description of the locations is given.

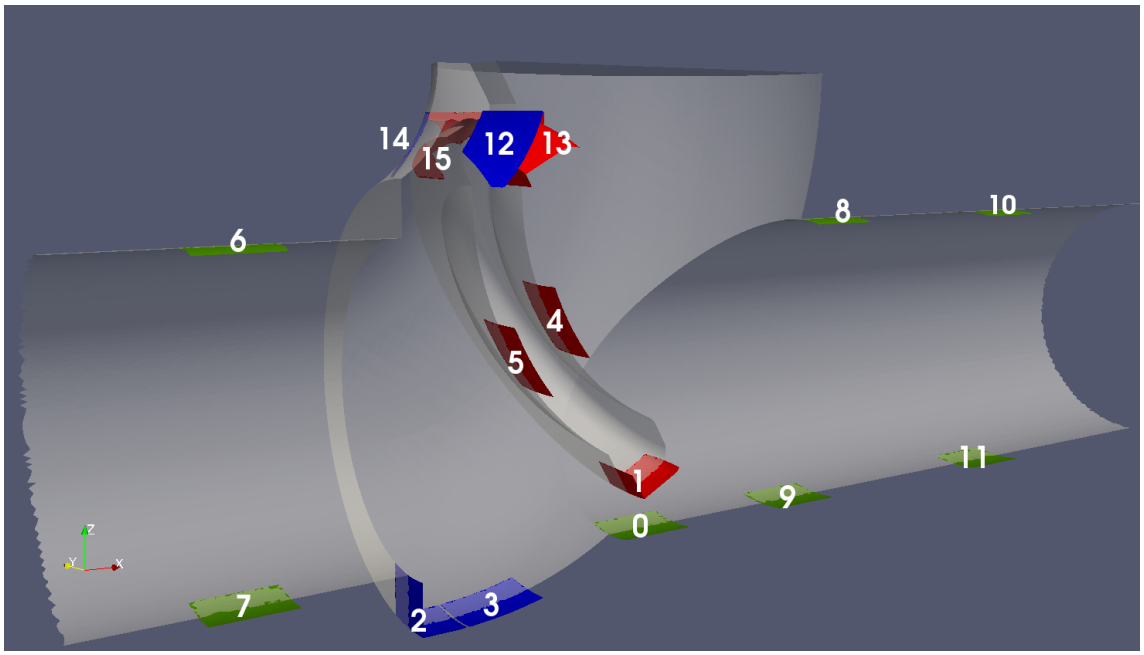

Figure 3.74: *Droplet deposition sites for the 3 in valve geometry.*

Table 3.12: *Description of deposition sites: blue patches - valve casing, green patches - pipe, red - valve (=hinged plate)*

Surface number See Figs. 3.66 & 3.67	Description
0	'Pinch-point' exit below the clapper
1	Base of valve
2, 3	Bottom of valve body bowl
4, 5	Upstream (4) and downstream (5) faces of valve
6, 7	Upstream of valve region (0.5 diameter upstream of sealing face): top (respectively bottom)
8, 9	Downstream of valve region (in pipe, ∼0.5 diameters from sealing face), vertical mid-plane
10, 11	Downstream of valve region (in pipe, ∼1.5 diameters from sealing face), top/bottom (respectively) of pipe
12, 13, 14, 15	Top and side of valve, valve support arm

Table 3.13: *Summary of droplet deposition for the 3 in. valve geometry (20F 37 US gals/min, Small distribution)*

ID	S_{dep}	M_{dep}	M1	M2	M3	Percentage of M_{dep}		
	m^2	$kg\ m^{-2}s^{-1}$	$kg\ m^{-2}s^{-1}$	$kg\ m^{-2}s^{-1}$	$kg\ m^{-2}s^{-1}$	M1	M2	M3
0	3.00E-04	2.10E-02	6.50E-03	8.70E-03	6.30E-03	30%	41%	29%
6	3.00E-04	5.10E-03	2.00E-03	2.40E-03	7.10E-04	39%	47%	14%
7	3.00E-04	3.70E-03	1.90E-03	1.10E-03	7.00E-04	50%	31%	19%
8	2.90E-04	1.20E-03	6.50E-04	5.20E-04	0.00E+00	56%	44%	0%
9	3.00E-04	2.90E-04	2.90E-04	0.00E+00	0.00E+00	100%	0%	0%
10	3.00E-04	2.10E-03	7.60E-04	6.50E-04	7.10E-04	36%	31%	34%
11	3.00E-04	7.40E-06	7.40E-06	0.00E+00	0.00E+00	100%	0%	0%
2	3.60E-04	1.70E-04	1.70E-04	0.00E+00	0.00E+00	100%	0%	0%
3	3.00E-04	8.70E-04	1.80E-04	0.00E+00	6.90E-04	20%	0%	80%
12	2.30E-04	4.80E-03	1.30E-03	1.70E-03	1.80E-03	28%	34%	38%
14	2.30E-04	3.90E-03	1.10E-03	1.00E-03	1.80E-03	27%	26%	47%
1	3.10E-04	1.40E-03	1.20E-03	1.70E-04	0.00E+00	87%	13%	0%
4	3.00E-04	1.50E-03	5.90E-04	9.50E-04	0.00E+00	38%	62%	0%
5	3.00E-04	9.20E-04	2.20E-04	0.00E+00	7.00E-04	24%	0%	76%
13	4.10E-04	5.50E-06	5.50E-06	0.00E+00	0.00E+00	100%	0%	0%
15	4.12E-04	0.00E+00	0.00E+00	0.00E+00	0.00E+00	-	-	-

Table 3.13 shows the deposition rates at sixteen different sites in the neighbourhood of the clapper valve. In regions of low deposition, the accuracy of the mass flux estimation can be inaccurate because of the lack of statistical enough data.

The table shows clearly that the largest deposition rate is at location 0, immediately below the valve where the flow accelerates and there is both high vorticity and strain rate.

Most of the other regions have a deposition rate of around 1 $\mathrm{g.m^{-2}.s^{-1}}$ because of the vortices before and after the valve plate.

After the valve, the flow raises slightly from the bottom of the pipe (see, for example Figure 3.68), which causes a decrease in the deposition at locations 9 and 11.

Zones 13 and 15 have extremely low (almost zero) deposition rates because most of the flows pass under the valve, and because large drops impact surface 14 preferentially.

Chapter 4

Beyond the droplet work

This chapter introduces advanced features developed to simulate droplet-induced pool flows. As the main focus of the thesis is the droplet motion and deposition and not specifically the pool flow, only a brief overview of the code capabilities are presented here. This chapter however relates to the previous work described in this thesis on the simulation of complex droplet-based flow pattern.

A moving mesh strategy has been developed to resolve the main region deformations caused by the liquid-gas interface.

4.1 From the deposition to the pool formation

The code implemented in OpenFOAM contains wetting models to transform deposited Lagrangian particles into a liquid phase. The film thus formed is solved using its own set of equations. In practice, there are numerous depositing droplets contributing to the formation of this new phase, eventually leading to a pool formation. In the contrary, a flow simulation initialized with a film can have its film removed due to the shear stress of the primary phase.

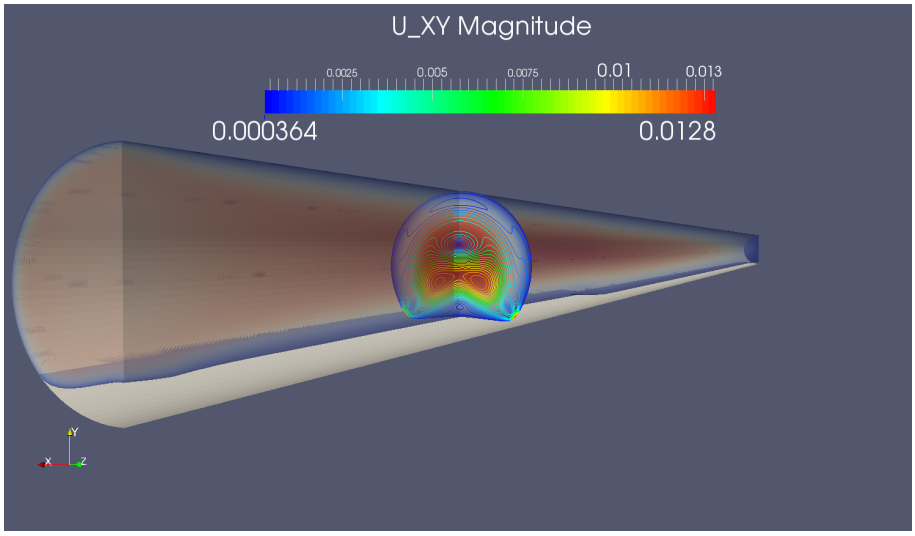

Figure 4.1: *Transient simulation of the development of a separated flow; secondary flows can appear in the primary phase; a wave front can be seen travelling towards the outlet*

Figure 4.1 illustrates the solver capabilities in simulating multi-phase flows. This picture shows how the pool flow deforms the gas region, and how it affects the flow. The pool itself is not shown, only the interface shared by the primary region and the pipe walls are represented here.

4.1.1 The Boussinesq approximation for wavy flows

When droplets deposit onto a surface, they can spread and form a thin liquid film. To reduce the numerical cost of solving the full Navier-Stokes equations into a small liquid region, an approximation can be applied. The model should nevertheless be accurate enough to simulate waves, as their impact on the flow behaviour is important. Being able to predict which waves can become unstable is also useful to simulate the droplet entrainment. The Boussinesq approximation for wavy flows is valid for long dispersive waves and takes into account the gravity and the interfacial stress. This model is generally used to evaluate waves in the sea, were wavelength are larger than the depth. Waves given by these equations are non-linear.

$$\frac{\partial^2 \delta}{\partial t^2} - gh\frac{\partial^2 \delta}{\partial x^2} - gh\frac{\partial^2}{\partial x^2}\left(\frac{3}{2}\frac{\delta^2}{h} + \frac{1}{3}h^2\frac{\partial^2 \delta}{\partial x^2}\right) = 0 \tag{4.1}$$

where h is the mean depth and δ the pool height.

4.1.2 The lubrication theory

The lubrication theory also called thin film approximations, implies the following simplifications over the previous set of equations:

- no pressure variation within the film height
- inertia terms are negligible
- no surface normal velocity

Inertia terms $\left(\text{terms in } \frac{U^2}{L}\right)$ are negligible when the film velocity is small compared to the film length, or with a perfect parallel flow (heavily confined flows). Navier-Stokes equations simplified with these assumptions are reduced to:

$$\overline{grad}\,(p) = \rho\overline{g} + \mu.\overline{div}\left(\overline{\overline{grad}\,(\overline{u})}\right) \tag{4.2}$$

By considering only the wall-normal direction as significant for the velocity gradient, the following system can be written:

$$\begin{cases} \dfrac{\partial p}{\partial x} = \mu\dfrac{\partial^2 u_x}{\partial z^2} & \text{(4.3a)} \\ \dfrac{\partial p}{\partial y} = \mu\dfrac{\partial^2 u_y}{\partial z^2} & \text{(4.3b)} \\ \dfrac{\partial p}{\partial z} = \rho g & \text{(4.3c)} \end{cases}$$

Linear waves analysis

Small waves are balanced with surface tension and weight, plus forces as effects of upper gas (Bernoulli) and Laplace pressure caused by surface tension on a curved surface. Long wavelength are likely to be a major contribution to entrainment of droplets from the pool to the core flow. Multiple instabilities are generally needed to get a full entrainment. Primary instabilities mainly caused by Kelvin-Helmholtz instabilities (relative velocity at the interface not null). Instabilities of Rayleigh-Plateau are the second instabilities: they are caused by a vertical motion induced by the previous instability. One should not confuse Rayleigh-Plateau instabilities with Rayleigh-Taylor instabilities, caused by a difference of density between the two fluids. They may also be considered in this work as gas and liquid will be considered. It seems that their relative importance is small compared to the two previously cited instabilities. However, they act as the first dominant phenomenon in droplets breakup. This will be detailed later in Section 4.4.
The linear wave stability analysis consists in considering a perturbation and put them into the non-linear equations that describe the whole motion. To solve this problem numerically, it is necessary to first linearise the equations and to write them into the weak form. This will lead to a matrix system which can be solved as an eigenvalues problem. If the returned eigenvalues are unconditionally negative, this means the associated wavelength is stable.

Integrating Equation (4.3a) twice with surface shear and no wall slip boundary conditions leads to:

$$u_x(z) = \frac{1}{\mu}\frac{\partial p}{\partial x}\left(\frac{z^2}{2} - \delta z\right) + \frac{\tau_{int}}{\mu} z \tag{4.4}$$

And by using the mass conservation over a linear portion of film:

$$\frac{\partial}{\partial x}\int_0^{h(x)} \left(\frac{1}{\mu}\frac{\partial p}{\partial x}\left(\frac{z^2}{2} - \delta z\right) + \frac{\tau_{int}}{\mu} z\right) dz = -\frac{\partial \delta}{\partial t} \tag{4.5}$$

leads to

$$\delta\frac{\partial \delta}{\partial x}\tau_{int} + \frac{\delta^2}{2}\frac{\partial \tau_{int}}{\partial x} - \frac{1}{3}\frac{\partial}{\partial x}\left(\delta^3\frac{\partial p}{\partial x}\right) = -\mu\frac{\partial \delta}{\partial t} \tag{4.6}$$

The wall shear stress can be written as:

$$\tau_0 = f\left[\frac{1}{2}\rho\left(v^0\right)^2\right] = -\mu\left.\frac{\partial u_x}{\partial y}\right|_{y=0} \tag{4.7}$$

4.2 Mesh morphing, interface tracking

One new approach in this PhD work, is the way the flow is decomposed to deal with two main zones: the primary region and the film region. As both regions are dependent, there is a need to be able to pass informations from one domain to another. The first example treated here, shows how the local liquid height is passed to the primary region to adapt the mesh of this sector to the actual pool height.

4.2.1 Programming with OpenFOAM

Complex phenomena such as droplet entrainment from film, coalescence, break up, compressibility, non-homogeneously distributed film size around a pipe, pool behaviour, need to be reproduced in one code for the purpose of this PhD. OpenFOAM has been selected, as it offers a set of open source libraries to perform computational fluid dynamics studies. This free software will be used since it offers capabilities to modify the source code and adapt it to complex simulations. Other commercial codes such as FLUENT, CFX or StarCCM+ are often restricted and do not offer the possibility to modify the behaviour of the solver, even if additional functions can be implemented via User Defined Functions.
Separate ways to simulate the liquid phase already exist. This includes a pool (VOF is a common one) and thin liquid films using the lubrication formulation. However, there is no common way to deal with them both in a single numerical code. An algorithm is proposed here for OpenFOAM to solve at once both film and pools systems. The main flow is solved based on the standard Eulerian approach, solving Navier-Stokes equations in a collocated mesh[1]. The liquid phase consists in Lagrangian droplets and in an Eulerian film or pool. The coupling with the liquid film or pool is handled in such a way that Eulerian phases are solved separately. Each sector takes boundary values from the other sector and subsequently corrects itself.
This approach might not be the most efficient. An implicit monolithic matrix system resolution would be better in terms of convergence and stability. However, it is easier to manage interfacial fields using the chosen method and in particular the interfacial shear stress. This is also more convenient to implement in a modular programming approach.

4.2.2 Existing code

The base solver used for this project is available in OpenFOAM[2], and has been created to handle thin film and reacting droplets including chemical and thermodynamic reactions. For this purpose, OpenFOAM has a number of given chemical species with their thermodynamic tables, useful to evaluate the surface tension for the liquid phase. However, this system was originally developed to solve drop flows in a gas-liquid system and not for liquid-liquid systems. Despite of this limitation, it would be possible to use a modified version for liquid-liquid applications. This may requires to enter manually new species to account for all thermodynamic effects. This solver has been developed for compressible flows, which add an unnecessary complexity for common applications where the incompressibility hypothesis is generally valid. However, real flows are slightly compressible and having the solver already configured for real applications becomes an advantage.compressible flows which might be useless in most of common applications, and complexify flow computations.

Due to its object oriented decomposition, OpenFOAM is able to handle a list of

[1] OpenFOAM uses the Rhie-Chow interpolation for pressure-velocity correction
[2] it is called *reactingParcelFilmFoam*

selectable models, for each phase: gas, liquid, droplets, and interactions between each of them. OpenFOAM 2.2.0 provides a number models that have been used during this PhD:

- dripping model for film
- splash interaction
- condensation
- RANS models (k-ϵ, k-ω, etc).
- breakup models (see Section 2.3.4)

4.2.3 Code limitations

The original code did not easily handle periodic boundary conditions. This was even more complex with compressible flows. The usual periodic boundary condition in OpenFOAM copy values from the outlet to the inlet. However, a more complex boundary condition is now available which allows to specify a pressure drop between the inlet and the outlet. This procedure will still have to be improved for droplets transport. Furthermore, the robustness of this procedure will still have to be checked for a parallel case, which have moving boundaries.
There is no available model to handle both reacting particles and colliding particles at once in the current version of OpenFOAM (2.2.1).
Only RANS models are easy to enable for the original solver. It could be interesting to use LES or advanced RANS models to catch the secondary flows and to improve the pipe walls wetting, in addition to entrainment and deposition. One of the most important limitation of the original code is that it has not been designed to simulate pool or droplets entrainment. It does not solve any wave equations as the surface equation solved is closer to the lubrication approximation.

4.3 Strategy

To reproduce flow patterns described in Section 2.1.1, the choice of a lagrangian representation for the dispersed phase was motivated by the straightforward interaction of the droplets with the interface or with walls along with the size distribution implementation in OpenFOAM. This allows a very good representation of droplets, and their interaction with the other phases. The main drawback of that approach is the time required to compute a large number of droplets. However, thanks to nowadays computing capabilities (multi cores, GPU) this problem will be solved. Brünggel (2011) for instance, expose how to use GPU in OpenFOAM to compute a particle cloud evolution.
The choice of separating the pool from the primary region comes from the common representation of a shell mesh to simulate films. The idea in this project, is to preserve the shell part and extend the primary region topology. With the increase of the pool, the primary region will adapt its size. This process can be called

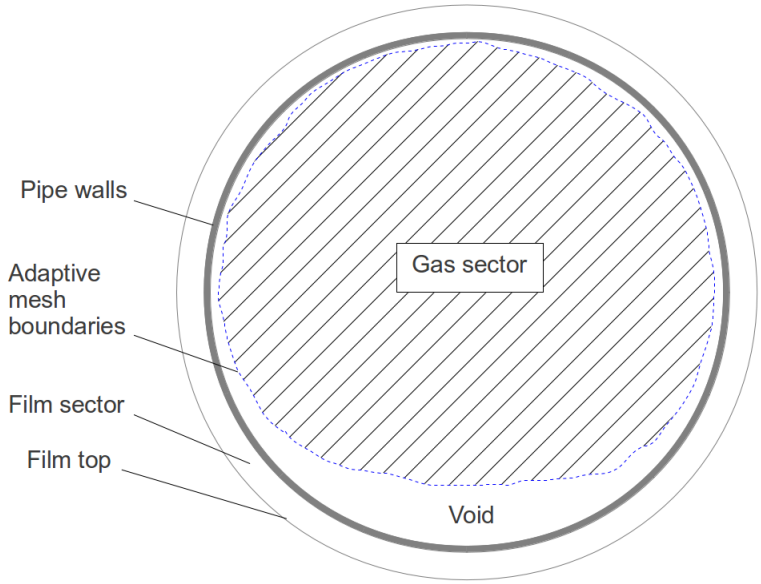

Figure 4.2: *Topology used*

adaptive morphing. This separated representation is appears as a more suitable approach compared to mixing models because of the possibility to have a well defined interface. Having a shell mesh to solve films is well documented, but extending the model to manage a pool is quite difficult. However, since the most important requirement is to obtain good estimates of interfacial velocity, there is no need to generate a precise description of the internal pool flow. Interpolated values will be sufficient for the model developed in this PhD.
Other advantages include the fact that the code will be able to handle a wide range of geometries, such as bended pipes and risers.
Figure 4.2 represents a cross section of a pipe, and shows the primary region and the film/pool sector.The *interface*, corresponds to the deformation of the gas sector (Adaptive mesh boundaries in Figure 4.2). Droplets crossing its boundaries can get a special treatment due to the presence of patches. This will be detailed further later in Section 2.3.6.
For simulation involving a gas phase, the primary region will be solved with a compressible Navier-Stokes solver pressure-based. A short description of compressible solver behaviour is given in the literature review.

4.3.1 Mesh modifications

Values of film height (called thereafter *deltaf*) in the pool are accessible only in film related classes. Access to those values needs to be granted to the primary region to correct the mesh by taking into account the volume of the pool/film. This is performed by writing in an external file the values of *deltaf* in the same order they are sorted in the film zone at every output time steps. Thus it becomes possible to read this file from the primary region and use *deltaf* values in the right order. Another field that expresses the film height is called *deltafVect* which is a

vector field as it contains the direction and orientation of liquid height from the walls.

Origin configuration-based or differential approach?

The two points of view are worth to be considered. One is based on deforming the mesh by adding *deltafVect* values over the original pipeline wall. The other one is based on accumulating deformations seen over a time step. They should be similar when there is no temporal variations in the direction of pool height increase. However in practice, it is not only deformations that are accumulated in the differential approach, but also errors and cell normal deviations. The difference of surfaces produced by one method and the other becomes therefore significant with long run simulations. This explains why the origin-based deformation is implemented in this code, even if the differential approach remains available.

Restart management

To prevent any failure in computation of compressible flow in the primary region, it is recommended not to compute the gas motion in the first step, as one should expect significant deformations of the mesh in case of pool/film starting initialization. Thus, the simulation should be stopped when the first mesh has been generated, and restart the solver with the gas resolution turned on using the new mesh. To be able to do so, a restart procedure has been developed. This procedure will attempt to automatically reconstruct all missing data to proceed all steps. The restart of a simulation should remain an exceptional procedure which may not be suitable for steps with major mesh deformations, as the automatic data re-constructor may have problems to reconstruct irregular geometries (such as interfacial waves). Moreover, the re-meshing procedure is always slower for the first restart step (about five time longer than the other steps). of the mesh, only if one

However, recent code development has greatly improved the reliability of the restart.

4.3.2 Algorithms

Patch value research

Figure 4.3 shows an example of the cross section mesh of a pipe. Three sectors appear: the central patch (Zone 1), created with by rounding a square at the centre of the pipe, the first crown (annular zone – Zone 2) close to the “rounded-square”, where cells sizes are regular, and the outer crown (Zone 3), which includes a refinement near the walls. Thereafter, the central zone will be called inner zone, and the two other zones will be called outer zones. Arrows in Figure 4.3 show the nearest boundary cell for two cells: one from Zone 1, and one from the outer zone. The red arrow explains why it has been decided not to move cells in Zone 1. As it can be seen, this arrow points to the interface between to cells, and this could be problematic. Although this problem could be solved, it would require extra

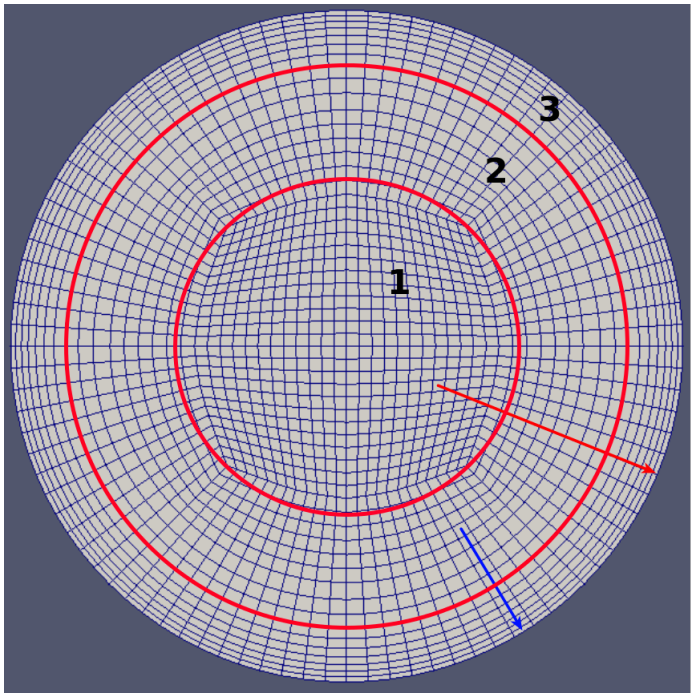

Figure 4.3: *Mesh representation - nearest boundary patch algorithm*

unnecessary development since the central part can be down sized and should not be affected by the pool deformation.

The re-meshing procedure is based on the update of the mesh vertices positions. It has been decided to move only vertex positions from the outer zone, as the geometry is a pipe and there should be a pool only in near walls regions. Moreover, the way the algorithm is created renders slightly difficult to displace vertices of the central patch. To re-mesh the interface, the algorithm loops over all primary region mesh cells and search for the nearest cell on boundary. The boundary cell label retrieved is used to find the corresponding pool height in *deltaf*. Then, points of the cell linked to that boundary cell are moved, following the smoothing procedure described later.
To find the nearest cell label, an algorithm based on the gradient of wall distance[3] was created. In a tube (which is always the case here at the first time step) every cell centre can be linked to one nearest boundary position only, except for the central cell, which is the centre of the circle. It is assumed that there is only one closest boundary cell and that the mesh is sufficiently regular so that the gradient points towards a cell and not an edge.

[3]Thus, it may happen that the closest boundary cell is not what it should be expected in case of large deformations ; a way to assign an unique boundary cell to all cells can be done with further development.

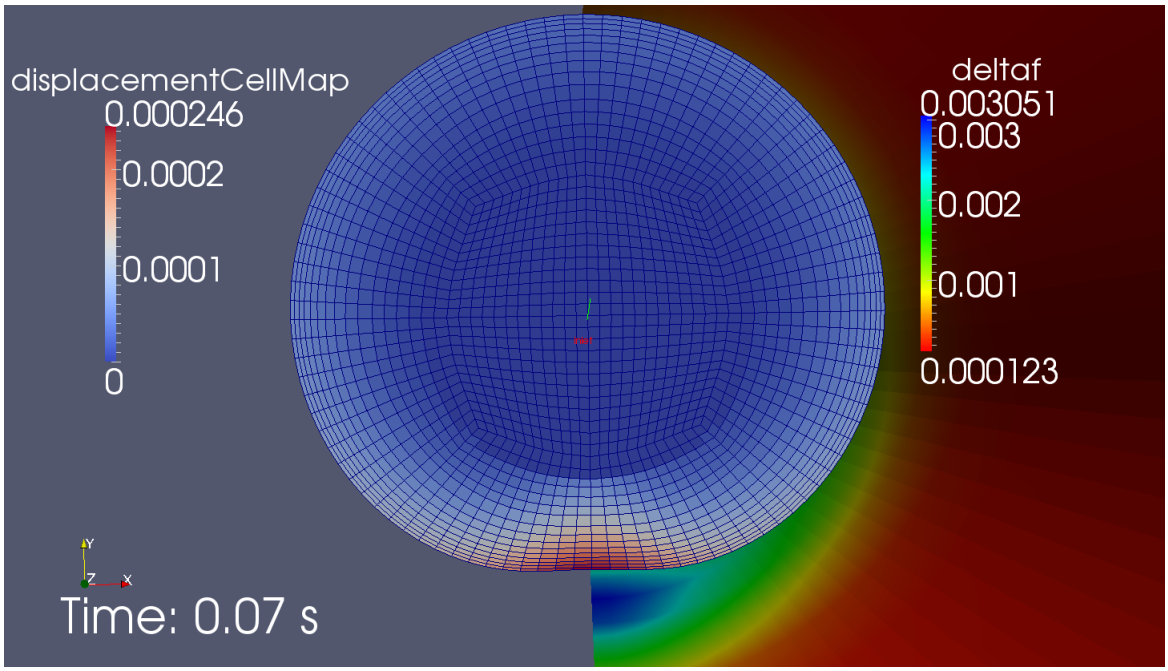

Figure 4.4: *Mesh deformation following pool size - proof of concept picture*

Figure 4.4 shows an example of mesh deformation: blue to red colours in mesh cells indicate the amplitude of the mesh deformation (*displacementCellMap* values). As it may be seen, a pool starts to form. The cell deformation should prevent large cell deformation gradient, as explained later. Notice that the deformation follows *deltaf* values, which are displayed on the right side of Figure 4.4. The algorithm that moves the boundary vertices is a separate algorithm, as the interpolation needed to move them is a surface interpolation and not a volume interpolation.

Inlet-outlet deformations

The inlet and outlet sections of the pipe are managed the same way. To ensure a continuity in mesh deformation near those patches, a “zero gradient” algorithm has been programmed. The vertices displacement map is taken from the nearest vertex already calculated in the core mesh. The algorithm proceeds as follows (given here for the inlet):

- Selection of a cell that belongs to the inlet
- Selection of a vertex from the selected cell that belongs to the inlet patch
- Search for the opposite cell face, which does not belong to the inlet patch
- Search in that face, the nearest vertex to the previously selected one, and get its identification
- Retrieve, using the identification, the deformation associated in the table already calculated by the in-core mesh algorithm

- Give the same deformation to the first selected vertex

The algorithm avoids looping on vertices already attributed: indeed, a vertex can belong to several faces.

Smoothing the internal deformation

The applied displacement on vertices should preserve the refinement near the wall. The smoothing applied here is based on a quadratic interpolation.

$$deformation(d) = Ad^2 + Bd + C \tag{4.8}$$

where d is the distance to the walls which depends on the position of the cell centre. For $d = 0$ the deformation is maximum and has for value $deltaf$. This implies $C = deltaf$. For $d = d_c$ the deformation is set to 0. d_c is the critical radius, which delimits the zone 1 (see Figure 4.2). To ensure a smooth connection at $d = d_c$ one imposes: $\frac{\partial deformation}{\partial d}\Big|_{d_c} = 0$. Finally the equation of cell deformation is given by:

$$deformation(d) = \frac{deltaf}{d_c^2}d^2 - \frac{2 \cdot deltaf}{d_c}d + deltaf \tag{4.9}$$

Optimization

Figure 4.5 shows an estimation of CPU Time Ratio taken by each main part of the algorithm.

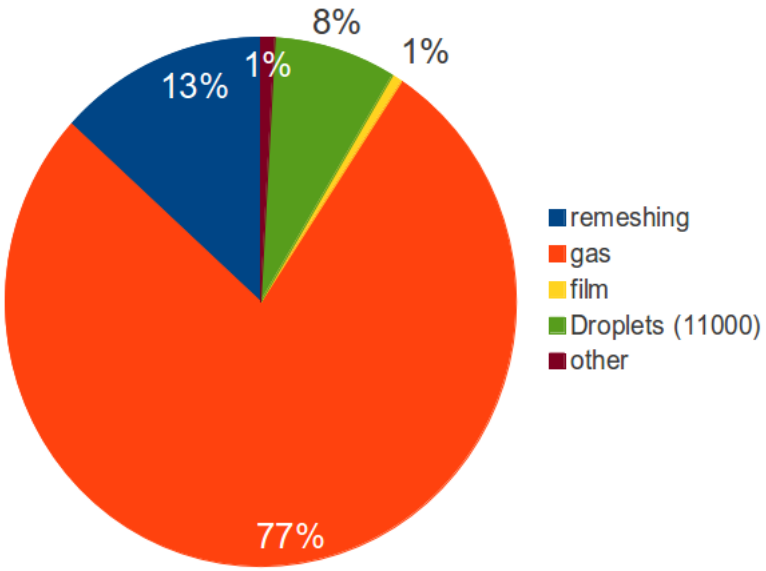

Figure 4.5: *CPU Time Ratio evaluated for 11000 droplets tracked*

It can be seen that solving the gas occupies the largest part of the time, around 77 % of the total simulation time. The re-meshing part takes 13 %, as it implies the reading/writing procedure, which is very time consuming. For 11,000 droplets,

the time ratio used to move them remains acceptable. This time is expected to increase rapidly with a greater number of droplets. This diagram was established for a single CPU, so those times could be reduced for parallel computations or if droplets motion is managed by a graphic card. Solving on the film is negligible in this case, however further modifications in phase coupling as well as wave simulation will increase the CPU time ratio allocated to the film solver. These values are dependent on the mesh size; this benchmark is based on a one meter pipe, with about 211,200 cells.

4.4 Particle entrainment

Droplets entrainment from a film or a pool is different from solid particle re-entrainment, even if the basic idea is similar, i.e.: a mass transfer from a wall (deposition state) to the upper flow. Elements given in this thesis are only valid for water droplets in pipes.
From a flat interface, sheared by an upper flow, interfacial instabilities may arise. The Kelvin-Helmholtz instability is believed to be responsible for creating waves from different wavelengths. Some of those waves are unstable, which means that their amplitude increases with time, under the actions of the upper shear stress. These actions are illustrated by Figure 4.6 and the ripping mechanism by Figure 4.7. According to Kim & Peterson (1994), three entrainment types can be

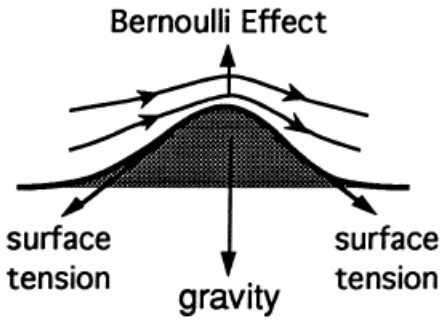

Figure 4.6: *Forces acting on waves*
Source: Vij et al. (1996)

distinguished:

- The wave-induced entrainment, where the pressure gradient over the interface is significant and the gas velocity may be small

- A shear-driven entrainment, where the gas flow is fast and the interfacial shear stress dominant, requires two consecutive instabilities

- An intermediary entrainment, sort of blending of the two previous entrainments

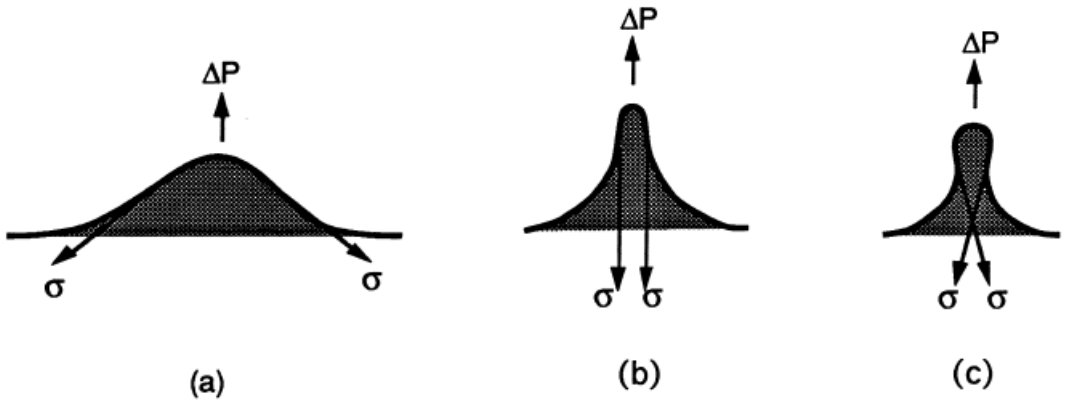

Figure 4.7: *Ripping mechanism leading to droplet entrainment*
Source: Vij et al. (1996) based on Tatterson's descriptions (1977)

As described in Section 4.1.2, the Kelvin-Helmholtz instability is responsible for the appearance of oscillations in the film height.
Finally, the surface tension σ is the force that ultimately separates droplets from the main liquid mass. The drop sees a shear of gas velocity, and is convected as usual. Later, the droplet could break up, again in several ways, as described in Kolev (1993a).
It has been shown in various experimentations[4] that it exists a critical liquid flow rate below which no entrainment can occur, as well as a critical gas surface velocity. For a low surface tension medium (for instance by addition of a surfactant), the entrainment rate is higher (see Hand *et al.* (1992) for instance). For Re_L below 270 for the pool/film, there is no entrainment possible.[5] Note that the wall surface wettability is of great importance to determine the flow pattern and thus the entrainment, as it was shown by Takamasa *et al.* (2008). Several models to predict the entrainment are available in the literature. Most of them are based on correlations dependant on the superficial velocities and/or mass fluxes of the continuous and dispersed phase. The most common model is based on a critical film/pool flow rate, above which, depending on a momentum equation on waves, parts of the wave crest is atomized. The Kelvin-Helmholtz instabilities are often designated to be the main cause for the apparition of unstable waves. It is also often assumed there is an equilibrium state with the deposition rates. Several papers also provide useful informations about the Particle Size Distribution of entrained particles. Details of the implementations of the entrainment models are out of the scope of this thesis, although some attempt to implement a tracking interface model have been performed in the goal of determining the entrainment rates. (Andritsos & Hanratty, 1987) details the interfacial wave stability. Here is a list of valuable publications about the entrainment: Pan & Hanratty (2002); Patruno *et al.* (2010a,b); Patruno & Dorao (2009); Williams *et al.* (1996)

[4]Hewitt and Hall-Taylor, 1970; Dallman et al., 1979; Asali et al., 1985b; Andreussi et al., 1985; Owen, 1986; Willetts, 1987; Schadel et al., 1990

[5]Reported from *The onset of droplet entrainment in annular downward flows* Paolo Andreussi Article first published online: 26 MAR 2009 DOI: 10.1002/cjce.5450580220

Chapter 5

Conclusion

This thesis describes all necessary minimal knowledge to achieve the objective of this PhD, i.e.: to produce a modular solver able to predict quickly and accurately droplets motion in pipes. The chosen numerical method is an Eulerian-Lagrangian solver using OpenFOAM as a starting toolbox. The following points summarize the main features of the models that has been used and implemented in the code:

- Main flow
  A compressible Eulerian solver has been considered, mainly based on current OpenFOAM capabilities. The main flow domain is delimited by a morphing mesh. This allows the solver to solve for one single region only, however taking into account boundary effects such as those due to the liquid pool.

- Pool/Film
  The current code is able to reproduce any size of film or pool up to 20% of liquid hold-up, depending on the flow physical conditions. Several models could be used simultaneously if a pool and a film coexist in the same configuration.

- Droplets
  A basic framework for droplet entrainment has been implemented, allowing droplets to be produced by direct entrainment from the pool and/or film surface depending on the physical conditions. It is also be possible to create a liquid zone from a dry-wall initialization by injecting droplets as a dispersed phase. This is a direct consequence of several particle-wall interaction models present in the code, such as splash, bouncing, deposition, etc. The particle turbulent dispersion has been implemented and validated, using up-to-date models from the literature. The transient dispersion in pipes has been described and a new statistical model to predict it has been produced.

- Phase change
  The solver is also able to generate either a film or a pool or both, reproducing the effects of condensation-evaporation on cooled/heated walls. A condensation model is available in OpenFOAM, although not used during the PhD.

- Scale-up
  A study on the behaviour of droplets dispersion and deposition in small, medium and large pipe diameters has been conducted. It has been shown that the dispersion behave similarly in small and in large pipe: the dispersion is driven by the flow characteristics (especially the turbulent kinetic energy) and the dispersion pattern affects the deposition. Non-dimensional flow descriptions from the literature provide the necessary information to evaluate the long-term dispersion and deposition velocity.

All those features implemented in a unique novel numerical code would help oil and gas companies in their extraction and transport processes of fuel, and would contribute to increase the safety and lower design costs in pumps, filters and other equipments. Finally, the code developed during this PhD will not be limited to oil and gas applications. It could also be potentially used as a design tool in aeronautics and automotive sectors.

State of the work and complementary work

The objective of this PhD was to study the particles motion in turbulent flows, however with a novel insight compared to existing methods. The code developed here has been tested for various applications, from academical to industry-based problems. The code has also been applied on various systems such as a personal computer and a multi-processor High Performance Computer. Numerous aspects of these complex flows have been studied and integrated in a single code, that can handle future improvements. This PhD has lead to various scientific papers (published or to be published soon). Thus, thanks to this PhD, the rules for a proper particle injection in a Lagrangian framework have been established. The effects of derogating from this injection rule have also been investigated. The subsequent dispersion and motion of various particles sizes have been studied in several geometries and turbulent flow conditions. A parcel approach has been used to simulate several millions of particles. Evaluating the Eulerian concentration of particle-particle collisions have become possible on a large scale, with the accuracy of the Lagrangian framework. Simulations involving the scaling-up of these dispersed flows have been performed during this PhD. Such information does not commonly appear in the literature. Particle deposition has been effectively evaluated.

Several features and improvements could be added to the code developed during this PhD and described in this thesis:

- Improvement of the region coupling and interface tracking
- GPU integration
- LES and DNS studies
- Icing and other thermal related phenomena
- Chemical reactions and surfactants studies
- Improvement of the adaptive mesh strategy

Appendix

Appendix A

Data Tables

Straight pipes

The simulation in the 3 in. straight pipe at 20F (37 US gal/min) for the small droplet size distribution has been run for 5s, with data reported every 0.1s. As a reminder, droplets have been injected in the fully developed flow, corresponding to the position $D = 0$. Collision results are summarised in Table A.1. The flow rate of the fluid considered is 37 US gal/min. Five boxes were created in the central part of the pipe (along the centreline) at the distance from the drop injection plane given in Column 2, the first column being the position inside the pipe geometry. It appears clearly that the collision rate varies in the pipe, along the centreline, as shown in Column 3. However, results obtained in all the 25D boxes were disregarded as droplets had not reached a steady state yet (droplets need a longer simulation time for the distribution to reach a steady state at 25D).

The number of collisions in boxes located at the top of the pipe (top, 12 o'clock in Column 1) seems slightly higher than in the middle of the pipe, although this is not clear enough to conclude.

The number of collisions in the bottom region of the pipe (bot, 6 o'clock in Column 1) is however lower than in the central and top regions of the pipe.

Right and left regions (right, 3 o'clock & left, 9 o'clock, in Column 1, respectively) show the largest number of collisions in the pipe.

Table A.1: *Collisions in the 3 in. straight pipe, 20F, 37 US gal/min. x coordinate in Column 1 is given in Column 2.*

Box pos.	Inlet dist.	Coll./s	Percentage of collisions 9-9	9-25	9-41	25-25	25-41	41-41	Drops/ box
cent	0.5D	187.63	25.00%	0.00%	75.00%	0.00%	0.00%	0.00%	5,780,868
(x,0,0)	1D	233.74	100.00%	0.00%	0.00%	0.00%	0.00%	0.00%	5,899,954
	2D	231.95	40.00%	0.00%	60.00%	0.00%	0.00%	0.00%	6,216,691
	5D	186.41	25.00%	0.00%	50.00%	25.00%	0.00%	0.00%	6,059,619
	10D	463.41	50.00%	30.00%	20.00%	0.00%	0.00%	0.00%	6,350,978
	25D	325.68	28.57%	42.86%	28.57%	0.00%	0.00%	0.00%	6,518,204
top	0.5D	193.98	33.33%	16.67%	33.33%	16.67%	0.00%	0.00%	8,904,944
(x,0,0.03)	1D	225.60	42.86%	28.57%	28.57%	0.00%	0.00%	0.00%	8,915,667
(12 o'clock)	2D	516.51	37.50%	18.75%	37.50%	0.00%	6.25%	0.00%	8,556,636
	5D	258.07	37.50%	25.00%	25.00%	12.50%	0.00%	0.00%	8,682,452
	10D	359.87	45.45%	45.45%	9.09%	0.00%	0.00%	0.00%	8,843,762
	25D	69.68	50.00%	0.00%	50.00%	0.00%	0.00%	0.00%	6,647,337
bot	0.5D	64.38	0.00%	100.00%	0.00%	0.00%	0.00%	0.00%	8,019,632
(x,0,-0.03)	1D	163.28	20.00%	60.00%	20.00%	0.00%	0.00%	0.00%	9,002,620
(6 o'clock)	2D	351.76	27.27%	36.36%	27.27%	9.09%	0.00%	0.00%	8,871,999
	5D	231.93	57.14%	0.00%	28.57%	0.00%	0.00%	14.29%	8,744,935
	10D	196.00	16.67%	66.67%	16.67%	0.00%	0.00%	0.00%	8,420,600
	25D	69.74	50.00%	50.00%	0.00%	0.00%	0.00%	0.00%	6,723,052
left	0.5D	697.64	32.35%	14.71%	50.00%	0.00%	2.94%	0.00%	12,932,149
(x,0.03,0)	1D	571.96	38.46%	34.62%	26.92%	0.00%	0.00%	0.00%	12,756,009
(9 o'clock)	2D	416.31	47.37%	15.79%	26.32%	5.26%	5.26%	0.00%	11,935,216
	5D	318.54	21.43%	21.43%	42.86%	7.14%	7.14%	0.00%	11,325,552
	10D	280.89	54.55%	27.27%	18.18%	0.00%	0.00%	0.00%	9,527,700
	25D	32.97	0.00%	0.00%	0.00%	0.00%	100.00%	0.00%	5,545,815
right	0.5D	581.42	35.71%	17.86%	42.86%	0.00%	3.57%	0.00%	13,348,240
(x,-0.03,0)	1D	717.61	41.18%	26.47%	29.41%	2.94%	0.00%	0.00%	13,369,706
(3 o'clock)	2D	381.69	41.18%	29.41%	23.53%	0.00%	5.88%	0.00%	11,974,746
	5D	427.76	22.22%	33.33%	44.44%	0.00%	0.00%	0.00%	11,719,714
	10D	387.86	46.67%	40.00%	13.33%	0.00%	0.00%	0.00%	8,915,894
	25D	99.13	0.00%	33.33%	33.33%	33.33%	0.00%	0.00%	5,111,403

As can be seen, the collision rate is higher for the smallest droplets (9μm). This collision rate decreases with the increase of the droplets size. Table A.1 therefore shows that the lowest collisions rate is obtained between the droplets of size $41\mu m$.

The number of collisions obtained in the 3 in. straight pipe reported in Table A.1. Note that each box considered in the 3 in. straight pipe[1] has the same volume, $V \simeq 3.7 \times 10^{-6}\ m^3$.

The analysis of droplets deposition in the 3 in. straight pipe has not been carried out with the box approach due to a very small number of droplets depositing on the pipe wall. However, to analyse the entry effects on droplet deposition, the deposition rate at different position down the pipe wall was investigated.

[1]Boxes in the straight pipes have the following dimensions: length=0.016042m, width=0.01522m & height=0.01522m

Bibliography

Abbott, C. E. 1977. A survey of Waterdrop Interaction Experiments. *Rev. Geophys.*, **15**(3), 363–374.

Abrahamson, J. 1975. Collision rates of small particles in a vigorously turbulent fluid. *Chemical Engineering Science*, **30**(Ii), 1371–1379.

Ahmadi, G., & McLaughlin, J. B. 2008. Transport, Deposition and Removal of Fine Particles - Biomedical Applications. *Pages 92–173 of:* Matijević, Egon (ed), *Medical Applications of Colloids*. Springer US.

Andritsos, N, & Hanratty, T J. 1987. Interfacial instabilities for horizontal gas-liquid flows in pipelines. *International Journal of Multiphase Flow*, **13**(5), 583–603.

ANSYS, Inc. 2013a. *Fluent 15.0 User's Guide*.

ANSYS, Inc. 2013b. *IcemCFD 15.0 User's Guide*.

Atiya, A. F., & M., Steve a. K. 2005. Efficient Estimation of First Passage Time Density Function for Jump-Diffusion Processes. *SIAM Journal on Scientific Computing*, **26**(5), 1760–1775.

Baehr H. D., Stephan K. 2011. *Heat and mass transfer - Third Edition*. Springer.

Berlemont, a., Desjonqueres, P., & Gouesbet, G. 1990. Particle lagrangian simulation in turbulent flows. *International Journal of Multiphase Flow*, **16**(1), 19–34.

Bocksell, T L, & Loth, E. 2006. Stochastic modeling of particle diffusion in a turbulent boundary layer. *International Journal of Multiphase Flow*, **32**(oct-nov), 1234–1253.

Bonn, Daniel, Eggers, Jens, Indekeu, Joseph, Meunier, Jacques, & Rolley, Etienne. 2009. Wetting and spreading. *Reviews of modern physics*, **81**(June), 739–805.

Brown, L., Hewitt, G.F., Hu, B., Thompson, C.P., & Verdin, P. 2009. Predictions of Droplet Distribution in Low Liquid Loading Stratified Flow in a Large Diameter Pipeline. *Pages 1–15 of: 14th International Multiphase Production Technology Conference*.

Brünggel, Nils. 2011. *Lagrangian Particle Tracking on a GPU*. M.Phil. thesis, Hochschule Luzern.

Code_Saturne. 2015. *Code_Saturne Theory Guide*.

Coninck, Joël De, de Ruijter, Michel J., & Voué, Michel. 2001. Dynamics of wetting. *Current Opinion in Colloid Interface Science*, **6**(1), 49 – 53.

Crowe, C., Sommerfeld, M., & Tsuji, Y. 1998. *Multiphase flows with droplets and particles*. CRC Press.

Dosio, A., Guerau de Arellano, J. V., Holtslag, A. a. M., & Builtjes, P. J. H. 2005. Relating Eulerian and Lagrangian Statistics for the Turbulent Dispersion in the Atmospheric Convective Boundary Layer. *Journal of the Atmospheric Sciences*, **62**(4), 1175–1191.

Eggels, J. G. M., Unger, F., Weiss, M. H., Westerweel, J., Adrian, R. J., Friedrich, R., & Nieuwstadt, F. T. M. 1994. Fully developed turbulent pipe flow: a comparison between direct numerical simulation and experiment. *Journal of Fluid Mechanics*, **268**(-1), 175.

Einstein, A. 1905. *On the movement of small particles suspended in stationary liquids required by the molecular-kinetic theory of heat*.

Flores, A G, Crowe, K E, & Griffith, P. 1995. Gas-phase secondary flow in horizontal, stratified and annular two-phase flow. *International Journal of Multiphase Flow*, **21**(2), 207–221.

FLUENT. 2014. User's Guide Fluent 14.0. *Fluent Incorporation, USA*.

Gosman, A. D., & Ioannides, E. 1983. Aspects of Computer Simulation of Liquid-Fueled Combustors. *Journal of Energy*, **7**(6), 482–490.

Gouesbet, G., & Berlemont, A. 1998. Eulerian and Lagrangian approaches for predicting the behaviour of discrete particles in turbulent flows. *Progress in Energy and Combustion Science*, **25**(2), 133–159.

Govan, a H, Hewitt, G F, & Ngan, C F. 1989. Particle motion in a turbulent pipe flow. *International Journal of Multiphase Flow*, **15**(3), 471–481.

Graham, D. I., & James, P. W. 1996. Turbulent dispersion of particles using eddy interaction models. *International Journal of Multiphase Flow*, **22**(1992), 157–175.

Gupta, Pankaj K, & Pagalthivarthi, Krishnan V. 2006. A comparative study of the effect of model lift coefficients on particle trajectory. *Indian Journal of Engineering & Materials Sciences*, **13**(August), 293–306.

Haerth, M., & Schubert, D. W. 2012. Simple approach for spreading dynamics of polymeric fluids. *Macromolecular Chemistry and Physics*, **213**, 654–665.

Hand, N P, Spedding, P L, & Ralph, S J. 1992. The effect of surface tension on flow pattern, holdup and pressure drop during horizontal air-water pipe flow at atmospheric conditions. *The Chemical Engineering Journal*, **48**(3), 197–210.

He, C., & Ahmadi, G. 1999. Particle deposition in a nearly developed turbulent duct with electrophoresis. *Journal of Aerosol Science*, **30(6)**.

Hetsroni, G., & Sokolov, M. 1971. Distribution of Mass, Velocity, and Intensity of Turbulence in a Two-Phase Turbulent Jet. *ASME*, **38**(2).

Hinze, J.O. 1975. *Turbulence:*. McGraw-Hill classic textbook reissue series. McGraw-Hill.

Jin, C., Potts, I., & Reeks, M. W. 2015. A simple stochastic quadrant model for the transport and deposition of particles in turbulent boundary layers. *Physics of Fluids*, **27**(5), 1–41.

Kallio, GA, & Reeks, MW. 1989. A numerical simulation of particle deposition in turbulent boundary layers. *International Journal of Multiphase Flow*, **15**(3), 433–446.

Kim, B.H., & Peterson, G.P. 1994. Theoretical and physical interpretation of entrainment phenomenon in capillary-driven heat pipes using hydrodynamic instability theories. *International Journal of Heat and Mass Transfer*, **37**(17), 2647–2660.

Kim, John, Moin, Parviz, & Moser, Robert. 1987. Turbulence statistics in fully developed channel flow at low Reynolds number. *Journal of Fluid Mechanics*, **177**(-1), 133.

Koeltzsch, K. 1998. On the relationship between the Lagrangian and Eulerian time scale. *Atmospheric Environment*, **33**(1), 117–128.

Kolev, N I. 1993a. Fragmentation and coalescence dynamics in multiphase flows. *Experimental Thermal and Fluid Science*, **6**(3), 211–251.

Kolev, N.I. 1993b. Fragmentation and coalescence dynamics in multiphase flows. *Experimental Thermal and Fluid Science*, **6**(1), 211–251.

Kolev, Nikolay Ivanov. 2007. *Multiphase flows dynamics 1: fundamentals*. Berlin: Springer.

Kou, S. G., & Wang, H. 2003. First passage times of a jump diffusion process. *Advances in Applied Probability*, **35**(2), 504–531.

Kruis, F. E., & Kusters, K. a. 1997. the Collision Rate of Particles in Turbulent Flow. *Chemical Engineering Communications*, **158**(1), 201–230.

Lai, A. C. K., & Cheng, Y. C. 2007. Study of expiratory droplet dispersion and transport using a new Eulerian modeling approach. *Atmospheric Environment*, **41**(35), 7473–7484.

Lain, S., & Sommerfeld, M. 2003. Turbulence modulation in dispersed two-phase flow laden with solids from a Lagrangian perspective. *International Journal of Heat and Fluid Flow*, **24**(4), 616–625.

Launder, B. E., Reece, G. J., & Rodi, W. 1975. Progress in the development of a Reynolds-stress turbulence closure. *Journal of Fluid Mechanics*, **68**(03), 537.

Launder, B.E., & Sharma, B.I. 1974. Application of the Energy-Dissipation Model of Turbulence to the Calculation of Flow Near a Spinning Disc. *Letters in Heat and Mass Transfer*, **1**(2), 131 – 138.

Lecrivain, G., & Hampel, U. 2012. Influence of the Lagrangian Integral Time Scale Estimation in the Near Wall Region on Particle Deposition. *Journal of Fluids Engineering*, **134**, 074502.

Li, A., & Ahmadi, G. 1993. Deposition of aerosols on surfaces in a turbulent channel flow. *International Journal of Engineering Science*, **21(3)**.

Liu, Benjamin Y H, & Agarwal, Jugal K. 1974. Experimental observation of aerosol deposition in turbulent flow. *Journal of Aerosol Science*, **5**(2), 145–155.

Loth, E. 2000. Numerical approaches for motion of dispersed particles, droplets and bubbles. *Progress in Energy and Combustion Science*, **26**(3), 161–223.

Marchioli, Cristian, & Giusti, Andrea. 2003. Direct numerical simulation of particle wall transfer and deposition in upward turbulent pipe flow. *International journal of Multiphase flow*, **29**, 1017–1038.

Matida, Edgar Akio, Nishino, Koichi, & Torii, Kahoru. 2000. Statistical simulation of particle deposition on the wall from turbulent dispersed pipe flow. *International Journal of Heat and Fluid Flow*, **21**(4), 389–402.

Menter, F R. 1994. Two-equation eddy-viscosity turbulence models for engineering applications. *AIAA Journal*, **32**(8), 1598–1605.

Menter, F.R. 1993. Zonal Two Equation k-omega Turbulence Models for Aerodynamic Flows. *AIAA paper*.

Nasr, Hojjat, & Ahmadi, Goodarz. 2007. The effect of two-way coupling and inter-particle collisions on turbulence modulation in a vertical channel flow. *International Journal of Heat and Fluid Flow*, **28**(6), 1507–1517.

Orme, Melissa. 1997. Experiments on droplet collisions, bounce, coalescence and disruption. *Progress in Energy and Combustion Science*, **23**(1), 65–79.

Pan, KL, & Law, CK. 2007. Dynamics of droplet–film collision. *Journal of fluid mechanics*, **587**, 1–22.

Pan, Lei, & Hanratty, Thomas J. 2002. Correlation of entrainment for annular flow in vertical pipes. *International Journal of Multiphase Flow*, **28**(3), 363–384.

Pang, MJ, & Wei, JJ. 2011. Analysis of drag and lift coefficient expressions of bubbly flow system for low to medium Reynolds number. *Nuclear Engineering and Design*.

Papavergos, P. G., & Hedley, A. B. 1984. Particle Deposition Behavior from Turbulent Flows. *Chemical Engineering Research and Design*, **62**.

Paras, S.V., & a.J. Karabelas. 1991. Droplet entrainment and deposition in horizontal annular flow. *International Journal of Multiphase Flow*, **17**(4), 455–468.

Patruno, L E, Marchetti, J M, Dorao, C A, Svendsen, H F, & Jakobsen, H A. 2010a. Droplet size distribution after liquid entrainment in horizontal stratified two-phase three-field dispersed flow. *Chemical Engineering Science*, **65**(4), 1407–1414.

Patruno, L E, Marchioro Ystad, P A, Jenssen, C B, Marchetti, J M, Dorao, C A, Svendsen, H F, & Jakobsen, H A. 2010b. Liquid entrainmentâ"Droplet size distribution for a low surface tension mixture. *Chemical Engineering Science*, **65**(18), 5272–5284.

Patruno, LE, & Dorao, CA. 2009. On the modelling of droplet–film interaction considering entrainment, deposition and breakage processes. *Chemical Engineering Science*, **64**, 1362–1371.

Picano, F., Sardina, G., & Casciola, C. M. 2009. Spatial development of particle-laden turbulent pipe flow. *Physics of Fluids*, **21**(2009), 093305.

Pilch, M, & Erdman, C A. 1987. Use of breakup time data and velocity history data to predict the maximum size of stable fragments for acceleration-induced breakup of a liquid drop. *International Journal of Multiphase Flow*, **13**(6), 741–757.

Qian, J, & Law, CK. 1997. Regimes of coalescence and separation in droplet collision. *Journal of Fluid Mechanics*.

Rein, Martin. 1993. Phenomena of liquid drop impact on solid and liquid surfaces. *Fluid Dynamics Research*, **12**(2), 61–93.

Saffman, PG, & Turner, JS. 1956. On the collision of drops in turbulent clouds. *Journal of Fluid Mechanics*, 16–30.

Salome. 2015. *User's Guide*.

Sommerfeld, Martin. 2001. Validation of a stochastic Lagrangian modelling approach for inter-particle collisions in homogeneous isotropic turbulence. *International Journal of Multiphase Flow*, **27**, 1829–1858.

Szabados, Tamas. 2010. An elementary introduction to the Wiener process and stochastic integrals. 45.

Takamasa, T, Hazuku, T, & Hibiki, T. 2008. Experimental Study of gas-liquid two-phase flow affected by wall surface wettability. *International Journal of Heat and Fluid Flow*, **29**(6), 1593–1602.

Taylor, G. I. 1922. Diffusion by Continuous Movements. *Proceedings of the London Mathematical Society*, **s2-20**(1), 196–212.

Tian, L., & Ahmadi, G. 2007. Particle deposition in turbulent duct flows-comparisons of different model predictions. *Journal of Aerosol Science*, **38(4)**.

Tsuji, Yutaka, Morikawa, Yoshinobu, & Shiomi, Hiroshi. 1984. LDV measurements of an air-solid two-phase flow in a vertical pipe. *Journal of Fluid Mechanics*, **139**(2), 417–434.

Verdin, P.G., Thompson, C.P., & Brown, L.D. 2014. CFD modelling of stratified/atomization gas–liquid flow in large diameter pipes. *International Journal of Multiphase Flow*, **67**(July), 135–143.

Vij, A K, Dunn, W E, & Conditioning, Air. 1996. Modeling of Two-Phase Flows in Horizontal Tubes. **61801**(May).

Vreman, A. W. 2007. Turbulence characteristics of particle-laden pipe flow. *Journal of Fluid Mechanics*, **584**, 235–279.

Vreman, A. W. 2015. Turbulence attenuation in particle-laden flow in smooth and rough channels. *Journal of Fluid Mechanics*, **773**, 103–136.

Weller, H G, & Tabor, G. 1998. A tensorial approach to computational continuum mechanics using object-oriented techniques. *Computers in Physics*, **12**(6), 620–631.

Wells, M. R., & Stock, D. E. 1983. The effects of crossing trajectories on the dispersion of particles in a turbulent flow. *Journal of Fluid Mechanics*, **136**, 31.

Williams, L.R., Dykhno, L.a., & Hanratty, T.J. 1996. Droplet flux distributions and entrainment in horizontal gas-liquid flows. *International Journal of Multiphase Flow*, **22**(I), 1–18.

Yarin, Alexander L. 2006. Drop Impact Dynamics: Splashing, Spreading, Receding, Bouncing... *Annual Review of Fluid Mechanics*, **38**, 159–192.

Young, J, & Leeming, A. 1997. A theory of particle deposition in turbulent pipe flow. *Journal of Fluid Mechanics*, **340**(September 2000), 129–159.

Zhang, M. Y., Zhang, H., & Zheng, L. L. 2008. Simulation of droplet spreading, splashing and solidification using smoothed particle hydrodynamics method. *International Journal of Heat and Mass Transfer*, **51**, 3410–3419.